Study on the discovery of new heavy, neutral gauge bosons with the ATLAS experiment

ΑΡΙΑΔΝΗ ΑΝΤΩΝΑΚΗ

PhD Thesis

ΕΘΝΙΚΟΝ & ΚΑΠΟΔΙΣΤΡΙΑΚΟΝ
ΠΑΝΕΠΙΣΤΗΜΙΟΝ ΑΘΗΝΩΝ

Εθνικό και Καποδιστριακό Πανεπιστήμιο Αθηνών
Τμήμα Φυσικής
Τομέας Πυρηνικής Φυσικής και Στοιχειωδών Σωματιδίων

Μάρτιος 2012

Εισαγωγή

Η παρούσα διατριβή παρουσιάζει τα πρώτα αποτελέσματα της αναζήτησης νέων βαρέων, ουδετέρων διανυσματικών μποζονίων στο πείραμα ATLAS, με χρήση της διάσπασής τους σε μιόνια ($Z' \to \mu^+\mu^-$). Τα αποτελέσματα αφορούν αφενός τα πρώτα $42\,\mathrm{pb}^{-1}$ των δεδομένων από συγκρούσεις πρωτονίων - πρωτονίων που συνελέγησαν κατά τη διάρκεια του 2010 στον νέο επιταχυντή LHC (Large Hadron Collider) του CERN και αφετέρου δεδομένα που συνελέγησαν μέσα στο 2011, συνολικής φωτεινότητας $1,21\,\mathrm{fb}^{-1}$.

Η σπουδαιότητα της έρευνας για την αναζήτηση του νέου βαρέος μποζονίου Z' έγκειται στο γεγονός ότι η ανακάλυψή του θα αποτελούσε μία σίγουρη ένδειξη για νέα φυσική. Υπάρχει μία σειρά θεωρητικών μοντέλων τα οποία προβλέπουν την ύπαρξη νέων ουδέτερα φορτισμένων μποζονίων βαθμίδας (GUTs [7], E6 models [8], Left-Right Symmetric models [11], Little Higgs models [13], Kaluza-Klein models [12] κ.α.). Η μάζα του μποζονίου δεν προβλέπεται από τη θεωρία και μπορεί να βρίσκεται οπουδήποτε ανάμεσα στην E_{weak} και την E_{GUT} (δηλαδή, ανάμεσα στην ενέργεια σπασίματος της ηλεκτρασθενούς συμμετρίας και την ενέργεια στην οποία η ηλεκτρομαγνητική, η ασθενής και η ισχυρη δύναμη ενοποιούνται σε μία κοινή δύναμη).

Το μποζόνιο Z' αναμένεται να εμφανιστεί στο πείραμα ATLAS σαν ένας συντονισμός με μεγάλη μάζα, στη διαδικασία Drell-Yan ($pp \to \ell^+\ell^-$ όπου $\ell = e, \mu$ και τ). Ο μηχανισμός παραγωγής υποδεικνύει ότι το Z', σε αναλογία με το μποζόνιο Z του Καθιερωμένου Προτύπου, είναι ηλεκτρικά ουδέτερο, colorless και self-adjoint (σωμάτιο χωρίς χρώμα, που αποτελεί το αντισωμάτιο του εαυτού του).

Η παρούσα διατριβή αποτελείται από πέντε κεφάλαια. Στο πρώτο κεφάλαιο δίνεται μία θεωρητική εισαγωγή, ξεκινώντας από μία σύντομη επισκόπηση του Καθιερωμένου Προτύπου και προχωρώντας στη συνέχεια στη θεωρητική περιγραφή της ύπαρξης νέων ουδετέρων διανυσματικών μποζονίων, με αναλυτική παρουσίαση των ιδιοτήτων και των χαρακτηριστικών τους. Στο δεύτερο κεφάλαιο περιγράφεται ο ανιχνευτής του πειράματος ATLAS, συμπεριλαμβανομένων όλων των σχετικών συστημάτων ανίχνευσης (Εσωτερικός Ανιχνευτής, Καλορίμετρα, Φασματόμετρο Μιονίων), ποιότητας δεδομένων και προσομοίωσης

. Στο τρίτο κεφάλαιο περιγράφονται οι μέθοδοι ανακατασκευής μιονίων με το λογισμικό του πειράματος και η απόδοση του συστήματος και παρουσιάζονται αναλυτικά όλες οι μέθοδοι μελέτης που χρησιμοποιούνται στην εργασία (αλγόριθμοι ανακατα-σκευής, εργαλεία ελέγχου ποιότητας δεδομένων κ.λπ.).

Τα δύο τελευταία κεφάλαια αναφέρονται στην κυρίως ανάλυση πάνω στις δύο περιόδους λήψης δεδομένων του πειράματος (2010 και 2011). Αρχικα, περιγράφεται η διαδικασία λήψης δεδομένων από το πείραμα. Στην συνέχεια παρουσιάζεται όλη η διαδικασία επιλογής των ζευγών μιονίων και τα κριτήρια ποιότητας που εφαρμόζονται, τόσο στα πραγματικά δεδομένα, όσο και στα προσομοιωμένα δείγματα του σήματος και των διαδικασιών υποβάθρου. Εν γένει, τα κριτήρια επιλογής στοχεύουν στην επιλογή μιονίων με αρκετά μεγάλη εγκάρσια ορμή, ανακατασκευασμένων και από το Μιονικό Φασματόμετρο και από τον Εσωτερικό Ανιχνευτή. Για να εξασφαλιστεί η ποιότητα ανακατασκευής, τα μιόνια πρέπει να χαρακτηρίζονται από ικανό αριθμό ιχνών (“hits”) και στα δύο υποσυστήματα. Τέλος, απαιτείται να παράγονται κοντά στην πρωτεύουσα κορυφη και να μην συνοδεύονται από επιπλέον δραστηριότητα στο χώρο γύρω τους (ώστε να εξασφαλιστεί ότι δεν αποτελούν μέρος ενός πίδακα).

Μελετήθηκαν διάφορες διαδικασίες υποβάθρου, που χαρακτηρίζονται από την παραγωγή δύο αντίθετα φορτισμένων μιονίων στην τελική κατάσταση. Το βασικότερο ρόλο παίζει η διαδικασία Drell-Yan σε μιόνια ($Z \to \mu^+\mu^-$), ενώ συνυπολογίστηκαν οι διαδικασίες $t\bar{t}$, W + jets (όπου ένα jet ενδέχεται να αναγνωριστεί εσφαλμένα ως μιόνιο), η παραγωγή διμποζονίων και τέλος οι QCD διαδικασίες $b\bar{b}$ και $c\bar{c}$ σε μιόνια. Η συνεισφορά των κοσμικών σωματιδίων, ως μία άλλη πιθανή πηγή υποβάθρου, επίσης εξετάστηκε. Τα επιλεχθέντα γεγονότα χρησιμοποιήθηκαν για να κατασκευαστούν οι κατανομές της αναλλοίωτης μάζας από τα ζεύγη μιονίων στα πραγματικά γεγονότα και στις διαδικασίες υποβάθρου. Με αυτόν τον τρόπο μπορεί να εκτιμηθεί αν τα πραγματικά δεδομένα παρουσιάζουν παραγωγή γεγονότων πάνω από τα αναμενόμενα από το Καθιερωμένο Πρότυπο.

Τα δεδομένα και των δύο ετών δεν έδειξαν παραγωγή γεγονότων επιπλέον των αναμενομένων και, κατά συνέπεια, υπολογίστηκαν τα όρια στο γινόμενο σ*B (ενεργού διατομής * λόγο διάσπασης) για το Z', για μάζες στην περιοχή 0,3 με 2 TeV. Τα όρια αξιολογήθηκαν χρησιμοποιώντας στατιστική ανάλυση η οποία συμπεριέλαβε και το σχήμα της κατανομής της αναλλοίωτης μάζας (δεν ήταν, δηλαδή, ένα “counting experiment”), σε κάθε πιθανή μάζα παραγωγής του σήματος.

Πριν την έναρξη λειτουργίας του LHC, το όριο στη μάζα του Z' είχε εκτιμηθεί από το Tevatron, για το μιονικό κανάλι, ίσο με $1,071\,\mathrm{TeV}/c^2$. Στην παρούσα εργασία, με χρήση των δεδομένων του 2010, το όριο υπολογίστηκε στα $874\,\mathrm{GeV}/c^2$. Τα δεδομένα του 2011 επέκτειναν αυτό το όριο στα $1,678\,\mathrm{TeV}/c^2$.

Contents

Chapter 1

Theoretical Introduction

1.1 Standard Model

The Standard Model ([1],[2]) is a theory developed to explain what the world is and what holds it together. It is a simple and comprehensive theory that describes all the hundreds of particles that are observed in nature and all the complex interactions that take place between them.

The model structure is based on two groups of particles: the six quarks (u, d, c, s, t and b) and the six leptons (e, μ, τ along with their corresponding neutrinos ν_e, ν_μ, ν_τ). Those alone form the total amount of matter in nature and are characterized by a half-integer spin ("fermions"). There are also four force-carrier particles (otherwise "mediators"): the $W^{\pm}$ and Z bosons, the photon (γ) and the gluon (g), that have integer spins ("bosons") and are responsible for all the interactions between the fermions.

In other words, the basic picture of the Standard Model is that of fermions (quarks and leptons) with spin equal to $\frac{1}{2}$, which interact through forces that are carried by gauge bosons (the carriers), the spin of which is equal to unity: all the known matter particles are leptons and composites of quarks, and they interact in several ways by exchanging the force carrier particles.

The Standard Model is a renormalizable field theory, based on a local symmetry (i.e. separately valid at each space-time point x). It describes strong, electromagnetic and weak interactions. There are eight strong charges, called "color" charges (that they are carried by the gluons) and four electro-weak charges (that correspond to the rest of the carriers, γ, $W^{+,-}$ and Z). The commutators of these charges form a $G_{SM} = SU(3)\times SU(2)\times U(1)$ algebra. The theory is invariant under local gauge transformation of the symmetry group.

Gravity (to which the -purely hypothetical until now- graviton is associated as the carrier) is not included in the theory; moreover, it is negligible in the energy region accessed through our experimental capability.

The matter fermions are categorized in three generations ("families") with identical quantum numbers but different masses. Each family contains a weakly charged doublet of quarks, in three color replicas (Red, Green, Blue), and a colorless weakly charged doublet with a neutrino and a charged lepton.

Some details about the elementary particles and the force carriers can be seen in Tables 1.1, 1.2 and 1.3.

Symbol	Name	Generation	Charge ($\cdot e$)	Mass (MeV)	B	C	S	T	B
u	up	1^{st}	$+\frac{2}{3}$	2	$\frac{1}{3}$	0	0	0	0
d	down	1^{st}	$-\frac{1}{3}$	5	$\frac{1}{3}$	0	0	0	0
c	charm	2^{nd}	$+\frac{2}{3}$	1,300	$\frac{1}{3}$	1	0	0	0
s	strange	2^{nd}	$-\frac{1}{3}$	104	$\frac{1}{3}$	0	-1	0	0
t	top	3^{rd}	$+\frac{2}{3}$	171,000	$\frac{1}{3}$	0	0	1	0
b	bottom b	3^{rd}	$-\frac{1}{3}$	4,200	$\frac{1}{3}$	0	0	0	-1

Table 1.1: The six quarks of Standard Model and their quantum numbers

Symbol	Name	Generation	Charge ($\times e$)	Mass (MeV)	L_e	L_μ	L_τ
e^-	electron	1^{st}	1	0.5	1	0	0
ν_e	electron neutrino	1^{st}	0	$< 2 \cdot 10^{-6}$	1	0	0
μ^-	muon	2^{nd}	1	105	0	1	0
ν_μ	muon neutrino	2^{nd}	0	$< 1.9 \cdot 10^{-4}$	0	1	0
τ^-	tau	3^{rd}	1	1780	0	0	1
ν_τ	tau neutrino	3^{rd}	0	$< 1.8 \cdot 10^{-2}$	0	0	1

Table 1.2: The six leptons of Standard Model and their quantum numbers

Force	Carrier		Charge($\times e$)	Spin	Mass (GeV)
Electromagnetic	photon	γ	0	1	0
Strong	gluon	g	0	1	0
Weak	$W^{\pm}$		±1	1	80.4
	Z^0		0	1	91.2
Gravity	graviton	G	0	2	0

Table 1.3: The four forces of nature and their bosonic carriers

When a physical system has some sort of symmetry, according to Noether's theorem, there exists a current j^μ that should be conserved:

$$\partial_\mu j^\mu = 0 \tag{1.1}$$

The existence of a current, consequently, implies that there must be some "charge", which is the generator of the (local) symmetry group (and, thus, called "Noether charge"). As a trivial example, we could mention the electric charge "e", the generator of the electromagnetic symmetry -a U(1) symmetry. The conserved current here is, of course, the electric current.

According to this, the electric charge and the eight color charges are the generators of the corresponding symmetries. Regarding the (bosonic) carriers, the photon and the gluons have zero masses as a consequence of the exact conservation of those generators. The fact that the weak bosons W^+, W^- and Z have large masses ($m_{W^\pm} \sim 80\,\mathrm{GeV}$, $m_Z \sim 91\,\mathrm{GeV}$), instead of a zero one, is a clear indication that the corresponding symmetries are broken at some point. So, a crucial question is why and how the electroweak gauge symmetry is broken.

In Standard Model, this spontaneous breaking of the electroweak gauge symmetry is incorporated in the Higgs mechanism (also called "Englert-Brout-Higgs-Guralnik-Hagen-Kibble mechanism"). This is a theory [3] which predicts the presence of one (or more) new, spin 0 boson, named after the English theoretical physicist Peter Higgs: the Higgs boson. The discovery of the -not yet experimentally observed- Higgs particle is the main interest of modern Physics, since it is the last missing link of the Standard Model and its awaited appearance will complete the theory.

1.1.1 Interaction Formalism

Particles in nature interact either because they decay or because they respond to a force (due to the presence of another particle).

The decay of a fermion into a different one takes place due to the action of the mediator boson. Similarly, the interaction of two particles is again explained by the exchange of a mediator.

Consider a fermion and a boson that interact. The system of the two particles can be described by the following Lagrangian [4]:

$$L = \frac{p_1^2}{2m_1} + \frac{p_2^2}{2m_2} - \frac{1}{2}kV(x_1, x_2) \tag{1.2}$$

The above Lagrangian consists of three parts. Firstly, the two kinetic terms correspond to the free fermion and the free boson (the mediator). The third term, which is a potential one, describes the interaction between the two: for example, the interaction of a photon with an electromagnetic field.

In electromagnetic theory, the Lagrangian for a free particle of mass m and an free electromagnetic field, represented from a potential **A** in vacuum, is written as:

$$L_{free} = \frac{p^2}{2m} + \frac{1}{8\pi}\int \mathrm{d}^3x \left(\frac{1}{c^2}\left|\frac{\partial \mathbf{A}}{\partial t}\right|^2 + |\nabla \times \mathbf{A}|^2 \right) \tag{1.3}$$

We can get the Lagrangian with the interaction incorporated by simply replacing the ordinary momentum by the canonical one:

$$\mathbf{P} \rightarrow \mathbf{p} + \frac{q}{c}\mathbf{A} \tag{1.4}$$

Therefore, Equation 1.3 transforms to:

$$L_{inter} = L_{free} + \frac{q}{2mc}\mathbf{A} \cdot \left(2\mathbf{p} + \frac{q}{c}\mathbf{A}\right) \tag{1.5}$$

1.1.1.1 Quantum-mechanical model

In Quantum Mechanics, fermions or bosons can be represented by specific fields with some intrinsic properties. The interaction process is an exchange of energy and momentum between fields, which is governed by laws of conservation of intrinsic quantities.

In order to pass from the classical description of the previous paragraph, to the quantum-mechanical one, we have to do some replacements. First, a free particle state is described by a spinor: $\Psi = \Psi(x^\mu)$. Then, in the continuum, the Lagrangian $L = L(q, \dot{q})$ is replaced by a Lagrangian density $\mathcal{L}$, the generalized coordinates q by the fields Ψ and the generalized velocities $\dot{q} = \mathrm{d}q/\mathrm{d}t$ by the Ψ field gradient $\partial_\mu\Psi = \partial\Psi/\partial x^\mu$.

Therefore, we have a relation of the form:

$$\mathcal{L} = \mathcal{L}(\Psi, \partial_\mu\Psi) \tag{1.6}$$

The Lagrangian density for a free particle and an electromagnetic field can be written as follows (using natural units, i.e: $\hbar = c = 1$):

$$\mathcal{L}_{free} = \bar{\Psi}(i\gamma^\mu\partial_\mu - m)\Psi - \frac{1}{4}F_{\mu\nu}F^{\mu\nu} \tag{1.7}$$

In the above equation, $\bar{\Psi} = \Psi^\dagger\gamma^0$ and $F_{\mu\nu} = \partial_\mu A_\nu - \partial_\nu A_\mu$. The term $\bar{\Psi}(i\gamma^\mu\partial_\mu - m)\Psi$ is called the Dirac Lagrangian.

To incorporate the interaction and extract the quantum-mechanical version of Equation 1.5, we replace:

$$P_\mu \to p_\mu + qA_\mu \tag{1.8}$$

$$p_\mu \to -i\partial_\mu \tag{1.9}$$

$$P_\mu \to -iD_\mu \tag{1.10}$$

$$D_\mu \rightarrow \partial_\mu - iqA_\mu \tag{1.11}$$

and we finally get:

$$\mathcal{L}_{inter} = \mathcal{L}_{free} + q\bar{\Psi}\gamma^\mu\Psi A_\mu \tag{1.12}$$

We have, therefore, constructed the current $J^\mu = q\bar{\Psi}\gamma^\mu\Psi$, which is a conserved quantity:

$$\partial_\mu J^\mu = 0 \tag{1.13}$$

1.1.1.2 Local phase invariance

We can change the phase of all the fields that represent the particles (local phase change) by applying the rotation operator:

$$\Psi \rightarrow \Psi' = e^{-iq\alpha(x)}\Psi \tag{1.14}$$

Here $\alpha(x)$ depends on the coordinates and q is the generator of the rotation. The Dirac Lagrangian ceases to be invariant, because of the second term of Equation 1.15:

$$\mathcal{L}_D = \bar{\Psi}(i\gamma^\mu\partial_\mu - m)\Psi + q\bar{\Psi}\gamma^\mu\Psi\partial_\mu\alpha(x) \tag{1.15}$$

By making the particle to interact with potential A_μ and based on Equation 1.12, we can write:

$$\mathcal{L}_D = \bar{\Psi}(i\gamma^\mu\partial_\mu - m)\Psi + q\bar{\Psi}\gamma^\mu\Psi\partial_\mu\alpha(x) + q\bar{\Psi}\gamma^\mu\Psi A_\mu \tag{1.16}$$

We can calibrate the potential in such a way that the term of change of phase is canceled:

$$A_\mu \rightarrow A_\mu - q \cdot \partial\alpha(x) \tag{1.17}$$

Considering now Equation 1.11, we finally have:

$$\mathcal{L}_D = \bar{\Psi}(i\gamma^\mu D_\mu - m)\Psi \tag{1.18}$$

This Lagrangian (describing an interacting particle with a potential) is invariant under a local phase change, if the potential is calibrated according to 1.17. The fields represented by such calibrated potentials are called gauge fields.

1.1.2 Interactions

1.1.2.1 Strong Interaction

The strong interaction is based on a Lagrangian, invariant under local gauge transformations of the $SU(3)_C$ group. The subscript C indicates that the transformations only act on particles with color charge.

The strong interaction is represented by eight gauge fields for the gluons G^{α}_{μ} ($\alpha = 1, 2, \ldots, 8$) and each of these fields is associated with a generator: $T_\alpha = \lambda_\alpha/2$, with λ_α being the Gell-Mann matrices [5]:

$$\lambda_1 = \begin{bmatrix} 0 & 1 & 0 \\ 1 & 0 & 0 \\ 0 & 0 & 0 \end{bmatrix} \lambda_2 = \begin{bmatrix} 0 & -i & 0 \\ i & 0 & 0 \\ 0 & 0 & 0 \end{bmatrix} \lambda_3 = \begin{bmatrix} 1 & 0 & 0 \\ 0 & -1 & 0 \\ 0 & 0 & 0 \end{bmatrix}$$

$$\lambda_4 = \begin{bmatrix} 0 & 0 & 1 \\ 0 & 0 & 0 \\ 1 & 0 & 0 \end{bmatrix} \lambda_5 = \begin{bmatrix} 0 & 0 & -i \\ 0 & 0 & 0 \\ i & 0 & 0 \end{bmatrix} \lambda_6 = \begin{bmatrix} 0 & 0 & 0 \\ 0 & 0 & 1 \\ 0 & 1 & 0 \end{bmatrix}$$

$$\lambda_7 = \begin{bmatrix} 0 & 0 & 0 \\ 0 & 0 & -i \\ 0 & i & 0 \end{bmatrix} \lambda_8 = \frac{1}{\sqrt{3}} \begin{bmatrix} 1 & 0 & 0 \\ 0 & 1 & 0 \\ 0 & 0 & -2 \end{bmatrix}$$

Therefore, we have a spinor of the form $\Psi \rightarrow \Psi' = e^{-ig_S T_\alpha \alpha(x)}\Psi$. The $g_S T_\alpha = q_\alpha$ factors correspond to the coupling constants of the fields with gluons.

The T_α generators commute, according to:

$$[T_\alpha, T_b] = i f^{c}_{\alpha b} T_c \tag{1.19}$$

Here, $f^{c}_{\alpha b}$ is the structure constant of the $SU(3)_C$ group.

1.1.2.2 Electroweak Interaction

In 1961, S.L. Glashow, S. Weinberg and A. Salam proposed the unified description of electromagnetic and weak phenomena based on a Lagrangian, invariant under local gauge transformations of the $SU(2)_L \times U(1)_Y$ group [6]. The subscript L means that these transformations only act on components of the left chiral fermions and Y corresponds to the hypercharge quantum number.

Electroweak interactions are represented by four gauge fields: an isotriplet of vector fields W_μ^i (i=1,2,3) and a single field B_μ. Each of these fields are associated with the generators $\tau_i = \sigma_i/2$ of the weak isospin group $SU(2)_L$, where σ_i are the Pauli matrices:

$$\sigma_1 = \begin{bmatrix} 0 & 1 \\ 1 & 0 \end{bmatrix} \sigma_2 = \begin{bmatrix} 0 & -i \\ i & 0 \end{bmatrix} \sigma_3 = \begin{bmatrix} 1 & 0 \\ 0 & -1 \end{bmatrix}$$

and

y= I Y / 2

which correspond to the $U(1)_Y$ group (Y is the quantum number of hypercharge).

At low energies, we can only observe the $U(1)_{EM}$ symmetry (the gauge symmetry of electrodynamics, transmitted by the photon). This fact indicates that the $SU(2)_L \times U(1)_Y$ gauge symmetry is broken at a particular energy scale E_W. Therefore, the weak interaction must be mediated by particles (gauge bosons) with masses of the order of E_W.

The weak β decay is performed via the virtual exchange of a relatively heavy, charged ($q = \pm 1$) gauge boson, the $W^\pm$. This charged boson is associated to the $SU(2)_L$ gauge group. The $SU(2)_L$ gauge symmetry should also have one neutral (diagonal) generator, thus a neutral gauge boson with mass of the same order: the well-known Z boson.

Because the electromagnetic symmetry $U(1)_{EM}$ is different from the $U(1)_Y$ symmetry, the mass eigenstates γ and Z of the neutral gauge bosons are a linear combination of the two neutral gauge bosons associated to the $SU(2)_L$ and $U(1)_Y$ gauge groups.

The Lagrangian of the electroweak interaction in the Standard Model can be written in the form [9]:

$$-\mathcal{L}_{EW} = g J_i^\mu W_{i\mu} + g' J_Y^\mu B_\mu \tag{1.20}$$

where g and g' are the $SU(2)_L$ and $U(1)_Y$ couplings, correspondingly.

From the above relation, we can extract the neutral current interaction:

$$-\mathcal{L}_{EW}^{NC} = gJ_3^{\mu}W_{3\mu} + g'J_Y^{\mu}B_{\mu} \tag{1.21}$$

The currents of Equation 1.21 are:

$$J_3^{\mu} = \sum_i \bar{f}_i\gamma^{\mu}[t_{3iL}P_L + t_{3iR}P_R]f_i \tag{1.22}$$

$$J_Y^{\mu} = \sum_i \bar{f}_i\gamma^{\mu}[y_{iL}P_L + y_{iR}P_R]f_i \tag{1.23}$$

In the above equations, f_i is the field of the i^{th} fermion.

The factors:

$$P_L = \frac{1-\gamma^5}{2} \tag{1.24}$$

and

$$P_R = \frac{1+\gamma^5}{2} \tag{1.25}$$

are the left and right chiral projections. $t_{3iL,R}$ is the third component of the weak isospin for the left and right chiral component of f_i, for which the following relations are valid:

$$t_{3uL} = t_{3\nu L} = +\frac{1}{2} \tag{1.26}$$

$$t_{3dL} = t_{3e^-L} = -\frac{1}{2} \tag{1.27}$$

$$t_{3iR} = 0 \tag{1.28}$$

The weak hypercharges y_{iL} and y_{iR} are chosen in such a way that they give the correct electric charges q_i of the fermions (with respect to the positron charge):

$$t_{3iL} + y_{iL} = t_{3iR} + y_{iR} = q_i \tag{1.29}$$

Anticipating the spontaneous breaking of $SU(2)_L \times U(1)_Y$ to the electromagnetic subgroup $U(1)_{EM}$, we can write Equation 1.21 in the following form:

$$-\mathcal{L}^{NC}_{EW} = eJ^{\mu}_{EM}A_{\mu} + g_1 J^{\mu}_1 Z^0_{1\mu} \tag{1.30}$$

The new states appearing in the above equation are the mass eigenstate neutral gauge bosons: A_μ is the (massless) photon field and $Z^0_{1\mu} = Z_\mu$ the (massive) Z boson. Those are connected with the W^i_μ (i=1,2,3) and B_μ vector fields through the weak angle:

$$A_\mu = sin\theta_W W_{3\mu} + cos\theta_W B_\mu \tag{1.31}$$

$$Z_\mu = cos\theta_W W_{3\mu} - sin\theta_W B_\mu \tag{1.32}$$

The weak angle θ is given by:

$$\theta_W = tan^{-1}\frac{g'}{g} \tag{1.33}$$

Therefore, we have the new couplings:

$$e = sin\theta_W \tag{1.34}$$

and

$$g_1^2 = \frac{g^2}{cos^2\theta_W} \tag{1.35}$$

By inserting the chiral couplings:

$$\epsilon^1_L(i) = t_{3iL} - sin^2\theta_W q_i \tag{1.36}$$

and

$$\epsilon^1_R(i) = t_{3iR} - sin^2\theta_W q_i \tag{1.37}$$

the currents can be written in the form:

$$J^{\mu}_{EM} = \sum_i q_i \bar{f}_i \gamma_\mu f_i \tag{1.38}$$

and

$$J_1^\mu = \sum_i \bar{f}_i \gamma_\mu [\epsilon_L^1(i) P_L + \epsilon_R^1(i) P_R] f_i \tag{1.39}$$

1.2 Models with new gauge bosons

The Standard Model is a very successful theory. It has been able to describe nature and all physics phenomena -at elementary particles level- below 100 GeV and its predictions have been experimentally verified, with great success. However, there are several fundamental questions that remain unresolved. For example, the existence of exactly three generations of fermions (see above) and their mass hierarchy is not explained, the mechanism for electroweak symmetry breaking has not been experimentally confirmed yet or, in addition, severall parameters still lack a theoretical explanation.

There are indications, therefore, that the Standard Model is not a fundamental theory, but only a very good approximation of nature at the energy ranges that have been so far accessible to experimental capabilities. The search for theories beyond the Standard Model is an important part of modern Physics.

A large variety of such theories predict additional gauge bosons, that arise from extensions of the electroweak symmetry of the Standard Model. There are two types of such bosons, both electrically charged and neutral, which are named in analogy with the Standard Model W and Z bosons, and share some of their properties.

1.2.1 Charged bosons: W'

Any charged ($q = \pm 1$), spin 1, gauge boson, which is not included in the Standard Model, is called W' boson (regardless of the theoretical model introducing it) and, according to several predictions, such a boson can be discovered in LHC.

Theories and models which predict new charged gauge bosons range from Grand Unified Theories [10], the various Left-Right Symmetric Models [11], Kaluza-Klein theories [12] and Little Higgs models [13]. The new charged vector bosons may or may not have similar properties to the Standard Model bosons, depending on the theory that predicts them.

As an example, a theoretical model, based on the gauge group $SU(3)_C \times SU(2)_L \times SU(2)_R \times U(1)_{B-L}$ which is called a Left-Right Symmetric Model (LRSM), after spontaneous symmetry breaking, predicts a right-handed W_R gauge boson which mixes with the left-handed W_L boson of the Standard Model. The W_R gauge boson is a possible W' boson candidate.

The D0 experiment, at Fermilab, has set the present lower limit for the W' boson mass [14] to 1 TeV at 95% C.L. The LHC, with a final center-of-mass energy at 14 TeV, will increase the search reach.

1.2.2 Neutral bosons: Z'

The second case of new gauge bosons is the neutral one: a new, heavy gauge boson which, in analogy with the Z, is neutral with respect to its electric charge and its name is derived from the latter: Z' (again, regardless of the theoretical model predicting such a particle).

The Z' boson is the subject of this study and will be further analyzed in the following paragraphs.

1.3 The Z' boson

The Z' boson will appear in the ATLAS experiment as a massive (much above the 91.2 GeV mass of the Z boson) resonance, observed in the Drell-Yan process $pp \to \ell^+\ell^-$, where $\ell = e, \mu$ and τ. The production mechanism indicates that the Z', in analogy with the Z boson, is electrically neutral, colorless and self-adjoint.

However, the above procedure is not constraint to be a Z' boson. It is the spin of the new resonance that will give a hint for what kind of new physics we are dealing with [15]: a spin 0 $\bar{\nu}$ in R-parity violating SUSY, a spin 1 Kaluza-Klein excitation of a Standard Model gauge boson from some extra dimensional model or a spin-2 Kaluza-Klein excitation of the graviton, as in the Randall-Sundrum model.

The particle we are interested in, the Z' boson, is characterized by a spin equal to unity. Therefore, we are dealing with a new, electrically neutral, colorless and self-adjoint gauge boson with spin 1, arising from an extension of the Standard Model gauge group (see next paragraph).

It is a very short-lived particle, which can only be observed through its decay products (or through indirect interference effects). The decay products of the Z' will be detected above the Standard Model background (with the Drell-Yan process consisting the main background procedure). Such a background is always present because both the Z and γ particles are produced by the same processes which create a Z'.

1.3.1 Extensions of Standard Model

There are theories, beyond the Standard Model, which have been proposed and predict that strong and electroweak interactions can be described by one simple gauge group G at very high energies: $E > E_{GUT}$ (with GUT standing for "Grand Unified Theories").

The Grand Unified Theories indicate that all fundamental interactions should have one common origin and E_{GUT} is the energy scale where the three running gauge coupling constants of the Standard Model gauge group become equal. Obviously, for energies below that scale, the gauge group G must be broken, in order to give the Standard Model symmetry $SU(3)_C \times SU(2)_L \times U(1)_Y$.

In Figure 1.1, we present the merging of the forces at the high energy limit.

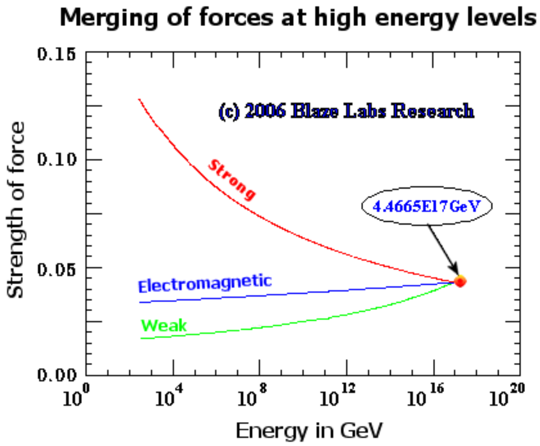

Figure 1.1: Unification of the forces

The smallest simple gauge group G, which can contain the Standard Model, is G = SU(5). The number n of neutral gauge bosons of a GUT is given by n = rank[G]. We know that the rank of SU(5) is equal to 4, which means that we can't have additional neutral gauge bosons. Therefore, the Z' boson can not be present in a SU(5) group.

Since the SU(5) group leaves no room for additional gauge bosons, we have to consider groups larger than that. The next gauge group that can allow for such a new particle is the SO(10) one. Its rank is equal to 5, therefore it allows for an additional neutral gauge boson. Obviously, GUTs with groups larger than SO(10), will predict more particles of that kind.

The minimal extension of the Standard Model gauge group is to add an abelian factor $U(1)'$ [16]. If some of the Standard Model particles have non-zero $U(1)'$ charges, the $U(1)'$ gauge symmetry must be broken at some scale (greater than the weak scale) and, thus, lead to a massive Z' (vector) boson which should then decay into some Standard Model particles and mixes with the known Z boson.

The extended group G' will be of the form:

$$G' = G_{SM} \times U(1)' = SU(3)_C \times SU(2)_L \times U(1)_Y \times U(1)' \tag{1.40}$$

The mass of the Z' is not constrained by theory. It can be anywhere between E_W and E_{GUT}. The LHC experiments have the potential to search the entire mass region up to $\sim$ 4 TeV.

1.3.2 Z' couplings

We start from the neutral current Lagrangian of equation 1.30 and we expand it by adding (in the general case) n additional U(1) groups. Therefore, for $n \geq 1$, we have:

$$-\mathcal{L}^{NC} = eJ^{\mu}_{EM}A_{\mu} + \sum_{\alpha=1}^{n+1} g_{\alpha} J^{\mu}_{\alpha} Z^{0}_{\alpha\mu} \tag{1.41}$$

(for the rest of this section, Reference [17] has been widely used).

In the summation term of 1.41, the factors with indexes equal to unity are the Standard Model parameters: g_1 the gauge coupling, $Z^0_{1\mu}$ the boson and J^0_1 the current. Similarly, g_α and $Z_{\alpha\mu}$ (for α = 2,3,...,n+1), are the gauge couplings and bosons for the additional $U(1)'$s.

The currents of the new models are given by:

$$J_\alpha^\mu = \sum_i \bar{f}_i \gamma^\mu \left[\epsilon_L^\alpha(i) P_L + \epsilon_R^\alpha(i) P_R\right] f_i \tag{1.42}$$

The above equation can also be written in the form:

$$J_\alpha^\mu = \sum_i \bar{f}_i \gamma^\mu [g_V^\alpha(i) - g_A^\alpha(i)\gamma^5] f_i \tag{1.43}$$

The chiral couplings $\epsilon_L^\alpha(i)$ and $\epsilon_R^\alpha(i)$, which may be unequal for a chiral gauge symmetry, are the $U(1)_\alpha$ charges for the left and right components of the fermion f_i. The factors

$$g_V^\alpha(i) = \epsilon_L^\alpha(i) + \epsilon_R^\alpha(i) \tag{1.44}$$

and

$$g_A^\alpha(i) = \epsilon_L^\alpha(i) - \epsilon_R^\alpha(i) \tag{1.45}$$

are the corresponding vector and axial couplings.

We specify the $U(1)_\alpha$ charges of the left chiral components of both the fermion f and the antifermion (conjugate) f^C, symbolized by $Q_{\alpha f}$ and $Q_{\alpha f^C}$, respectively. The relations with the chiral couplings are:

$$\epsilon_L^\alpha(f) = Q_{\alpha f} \tag{1.46}$$

$$\epsilon_R^\alpha(f) = -Q_{\alpha f^C} \tag{1.47}$$

For instance, in the Standard Model, equations 1.36 and 1.37 for the u and $\bar{u}$ quarks give $Q_{1u} = \frac{1}{2} - \frac{2}{3}sin^2\theta_W$ and $Q_{1u^c} = +\frac{2}{3}sin^2\theta_W$.

The additional gauge couplings and charges, as well as the gauge boson masses and mixing, are extremely model dependent. Still, the gauge couplings and charges can be modified simultaneously. For example, replacing g_α by $\lambda_\alpha g_\alpha$ is allowed but under the condition that the charges Q_α are reduced by a factor $1/\lambda_\alpha$.

For a complex SU(2) scalar multiplet ϕ:

$$\phi = \begin{pmatrix} \phi^+ \\ \phi^0 \end{pmatrix} \tag{1.48}$$

we can extract the three and four point gauge interactions from the kinetic term $\mathcal{L}_\phi^{kin} = (D^\mu\phi)^\dagger D_\mu\phi$, where $D_\mu\phi$ is the gauge covariant derivative.

The neutral current part of the gauge covariant derivative of an individual field ϕ_i is given by:

$$D_\mu\phi_i = \left[\partial_\mu + ieq_iA_\mu + i\sum_\alpha^{n+1} g_\alpha Q_{\alpha i} Z^0_{\alpha\mu}\right]\phi_i \tag{1.49}$$

Here q_i is the electric charge of the ϕ_i field and $Q_{\alpha i}$ its $U(1)_\alpha$ charge.

1.3.3 Masses and Mixing

Consider the general case of a gauge group G=SU(N), with N-1 diagonal generators. G can be broken by the vacuum expectation value (VEV) of a real adjoint Higgs representation Φ, which can be represented by a Hermitian traceless $N \times N$ matrix:

$$\Phi = \sum_{i=1}^{N^2-1} \phi^i L_i \tag{1.50}$$

where the ϕ^i are the real components of Φ and the L_i are the fundamental $N \times N$ representation matrices. When Φ acquires a vacuum expectation value $\langle\Phi\rangle$, SU(N) is broken to a subgroup associated with those generators which commute with $\langle\Phi\rangle$. Without loss of generality, $\langle\Phi\rangle$ can be diagonalized by an SU(N) transformation, so that the N-1 diagonal generators remain unbroken.

We assume that electrically neutral scalar fields ϕ_i acquire VEVs, so A_μ remains massless, while the $Z^0_{\alpha\mu}$ fields develop a mass term $\mathcal{L}_Z^m = \frac{1}{2}M^2_{\alpha\beta}Z^0_{\alpha\mu}Z^{0\mu}_\beta$, where:

$$M^2_{\alpha\beta} = 2g_\alpha g_\beta \sum_i Q_{\alpha i}Q_{\beta i}\left|\langle\phi_i\rangle\right|^2 \tag{1.51}$$

$M^2_{11} \equiv M^2_{Z^0}$ would be the (tree-level) Z mass in the Standard Model limit, in which the other Z^0's and their mixing can be ignored.

If the only Higgs fields are SU(2) doublets (or singlets), as in the Standard Model or the Minimal Supersymmetric Standard Model, then we can write:

$$M_{Z^0}^2 = \frac{1}{2} g_1^2 \sum_i |\langle\phi_i\rangle|^2 = \frac{1}{4} g_1^2 \nu^2 \tag{1.52}$$

with $\nu^2 = 2\sum_i |\langle\phi_i\rangle|^2 \sim (\sqrt{2}G_F)^{-1} \sim (246\,\mathrm{GeV})^2$ being the square of the weak scale (G_F is the Fermi constant).

Diagonalizing the mass matrix of Equation 1.51, we obtain n+1 eigenstates $Z_{\alpha\mu}$, with mass M_α:

$$Z_{\alpha\mu} = \sum_{\beta=1}^{n+1} U_{\alpha\beta} Z_{\beta\mu}^0 \tag{1.53}$$

where U is an orthogonal mixing matrix. It is straightforward to show that the mass-squared eigenvalues are always non-negative.

Using Equations 1.41 and 1.53, we see that $Z_{\alpha\mu}$ couples to $\sum_\beta g_\beta U_{\alpha\beta} J_\beta^\mu$.

For n=1 and writing $Q_{2i} \equiv Q_i$, we get the mass matrix:

$$M_{Z-Z'}^2 = \begin{bmatrix} 2g_1^2 \sum_i t_{3i}^2 |\langle\phi_i\rangle|^2 & 2g_1 g_2 \sum_i t_{3i} Q_i |\langle\phi_i\rangle|^2 \\ 2g_1 g_2 \sum_i t_{3i} Q_i |\langle\phi_i\rangle|^2 & 2g_2^2 \sum_i t_{3i}^2 |\langle\phi_i\rangle|^2 \end{bmatrix} = \begin{bmatrix} M_{Z^0}^2 & \Delta^2 \\ \Delta^2 & M_{Z'}^2 \end{bmatrix} \tag{1.54}$$

Many $U(1)'$ models involve an SU(2) singlet, S, and two Higgs doublets:

$$\phi_u = \begin{pmatrix} \phi_u^0 \\ \phi_u^- \end{pmatrix} \tag{1.55}$$

and

$$\phi_u = \begin{pmatrix} \phi_d^+ \\ \phi_d^0 \end{pmatrix} \tag{1.56}$$

with $U(1)'$ charges $Q_{S,u,d}$.

Then, the elements of the matrix in Equation 1.54 can be written as:

$$M_{Z^0}^2 = \frac{1}{4} g_1^2 \left(|\nu_u|^2 + |\nu_d|^2\right) \tag{1.57}$$

$$\Delta^2 = \frac{1}{2} g_1 g_2 \left(Q_u |\nu_u|^2 - Q_d |\nu_d|^2\right) \tag{1.58}$$

and

$$M^2_{Z'} = g_2^2 \left(Q_u |\nu_u|^2 + Q_d |\nu_d|^2 + Q_S |s|^2 \right) \tag{1.59}$$

Here, $\nu_{u,d} \equiv \sqrt{2}\langle \phi^0_{u,d} \rangle$, $s = \sqrt{2}\langle S \rangle$ and $\nu^2 = |\nu_u|^2 + |\nu_d|^2 \sim (246GeV)^2$.

The eigenvalues of a general $M^2_{Z-Z'}$ are given by the following equations:

$$M_1^2 = \frac{1}{2}\left[M^2_{Z^0} + M^2_{Z'} + \sqrt{(M^2_{Z^0} - M^2_{Z'})^2 + 4\Delta^4} \right] \tag{1.60}$$

and

$$M_2^2 = \frac{1}{2}\left[M^2_{Z^0} + M^2_{Z'} - \sqrt{(M^2_{Z^0} - M^2_{Z'})^2 + 4\Delta^4} \right] \tag{1.61}$$

The rotation U is given by:

$$U = \begin{bmatrix} cos\theta & sin\theta \\ -sin\theta & cos\theta \end{bmatrix} \tag{1.62}$$

where

$$\theta = \frac{1}{2} arctan(\frac{2\Delta^2}{M^2_{Z^0} - M^2_{Z'}}) \tag{1.63}$$

The θ angle is related to the masses through the following relation:

$$tan^2\theta = \frac{M^2_{Z^0} - M_1^2}{M_2^2 - M^2_{Z^0}} \tag{1.64}$$

An important limit is $M_{Z'} \gg (M_{Z^0}, |\Delta|)$. This typically occurs because an SU(2) singlet field (such as the S above) has a large VEV and contributes only to $M_{Z'}$. In this case, we have:

$$M_1^2 \sim M^2_{Z^0} - \frac{\Delta^4}{M^2_{Z'}} \ll M_2^2 \tag{1.65}$$

and

$$M_2^2 \sim M^2_{Z'} \tag{1.66}$$

We also can write:

$$\theta \sim -\frac{\Delta^2}{M^2_{Z'}} \sim C \frac{g_2}{g_1} \frac{M_1^2}{M_2^2} \tag{1.67}$$

where

$$C = -\frac{\sum_i t_{3i} Q_i \left|\langle\phi_i\rangle\right|^2}{\sum_i t_{3i} \left|\langle\phi_i\rangle\right|^2} \tag{1.68}$$

with C being model dependent.

1.3.4 The Sequential Standard Model Z'

The Sequential Standard Model (SSM) Z' [17] is defined to have the same couplings to fermions as the Standard Model Z boson.

It is not expected in the context of gauge theories unless it has different couplings to exotic fermions or if it occurs as some excited state of the ordinary Z in models with extra dimensions at the weak scale. However, it serves as a useful reference case when comparing constraints from various sources.

In the present study, the SSM Z' is the “model” which our analysis is performed on.

1.4 Z' Searches

Z' searches are of two kinds: indirect and direct. We can look for indirect Z' effects in precise electroweak data and for direct Z' production at large colliders [18].

Important constraints arise from both sources.

1.4.1 Indirect searches

An indirect search can be performed when we look for deviations from the Standard Model that might be associated with the existence of a Z'. This usually involves precision electroweak measurements at the Z-pole region, as well as below and above it.

In a model-independent approach, the Z' can be directly described in terms of its axial and vector couplings to fermions. Therefore, we can test the cross-sections and asymmetries measured at energies around the Z peak. If this particle is not the Standard Model Z but, instead, a mixture with a Z', the couplings to fermions will change [19].

At energies above 130 GeV, the interference between Z and Z' becomes increasingly important and the data are very sensitive to the mass of the Z'. Since changes to cross-sections and asymmetries arise from interference terms, the precise form of these changes depends strongly on the model.

To obtain limits on the Z' properties, cross-sections for the processes $e^+e^- \rightarrow \mu^+\mu^-, \tau^+\tau^-, q\bar{q}$ and the forward-backward asymmetries for the leptonic processes $e^+e^- \rightarrow \mu^+\mu^-, \tau^+\tau^-$ at energies around the Z resonance are compared to the predictions of the several Z' models (the forward-backward asymmetries are obtained by counting the numbers of events in the forward and backward hemispheres).

LEP indirect searches constrain Z' bosons to be heavier than a few hundred GeV. Similarly, in LHC, an indirect study would be focused on the dilepton invariant mass distribution dN/dM and the forward-backward asymmetry, A_{FB}, which is determined by the dilepton angular distribution (for more details, see Reference [20]).

1.4.2 Direct searches

If heavy gauge bosons turn out to have a mass of the order of a few TeV, a large collider is an ideal place to discover and study them. High-energy experiments can search for on-shell Z' production and decay.

The direct search for a Z' focuses on the existence of high-mass dilepton resonances: the production of the new boson takes place via quark-antiquark annihilation and it is then followed by the decay to a lepton pair: electron-positron or a pair of opposite-charged muons. The latter will give an invariant mass value much above the Standard Model Z boson pole.

Prior to the LHC era, the strictest limits from direct searches came from the D0 and CDF experiments at the Tevatron. The SSM Z' was excluded, for a mass lower than 1.071 TeV ([21],[22]).

Recently, CMS has also excluded a SSM Z' with a mass lower than 1.140 TeV [23]. A similar study of the ATLAS collaboration, using data taken during 2010, has set the lower limit on the Z' mass at 1.048 TeV (that particular analysis is presented in detail in Chapter 4).

Chapter 2

LHC accelerator and experiments

2.1 LHC - Structure and operation

LHC is a circular collider, which is designed to accelerate beams of protons up to a center of mass energy equal to $\sqrt{s} = 14\,\text{TeV}$ (7 TeV per beam). The protons included in each beam come in a form of bunches, with a minimum time distance of 25 ns from one another. The two beams are moving in opposite directions within two separate tubes and collide at four specific points inside the accelerator (the so-called Interaction Points: 1, 2, 5 and 8). These points are where the four major experiments that take place at the LHC are located (see Figure 2.1): ATLAS (A Toroidal LHC ApparatuS), CMS (Central Muon Solenoid), ALICE (A Large Ion Collider Experiment) and LHCb (Large Hadron Collider beauty).

The LHC, apart from protons, will occasionally accelerate heavy ions as well. More specifically, Lead (Pb) ions will be accelerated to energy up to 6TeV per nucleon, in the center of mass system.

In recent years, in the design of the accelerator, two new, smaller experiments have been added, namely TOTEM (TOTal Elastic and diffractive cross section Measurement) and LHCf (Large Hadron Collider forward). All, six in total, LHC experiments will be analyzed in the next paragraphs.

The LHC is installed in the existing tunnel of the older CERN accelerator LEP (Large Electron Positron). The tunnel has a length of 26.7 km and outspreads between

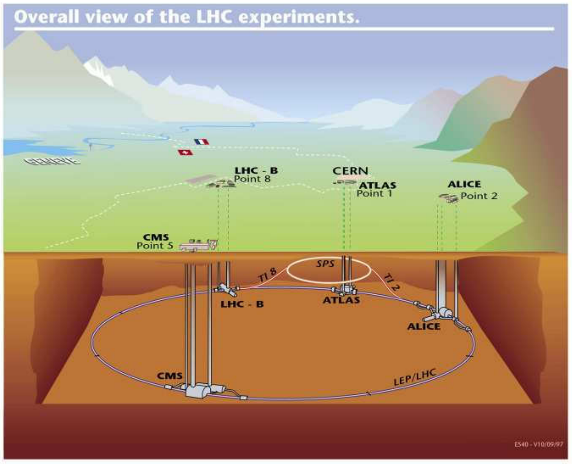

Figure 2.1: Underground representation of the LHC experiments

France and Switzerland.

The proton beams reach their final energy (presently 3.5 TeV each), following a series of successive accelerations in various pro-accelerators prior to being injected into the main LHC tunnel. The first stage is the production of protons from Hydrogen. The produced protons undergo the first accelerating procedure with the use of electromagnetic waves in the RF (radiofrequency) region. At this stage, their energy reaches the level of 750 KeV.

The next step is to lead the beams in a linear accelerator (Linac), where their energy upgrades to 50 MeV, just before entering the synchrotron (Booster), where the energy achieved reaches the value of 1.4 GeV. The next steps consists of the insertion of the beams in two successive accelerator systems, the Proton Synchrotron (PS), from which they come out with energy 26 GeV, and finally the Super Proton Synchrotron (SPS), which increases their energy up to 450 GeV. This is the energy the protons have when entering the main ring, where the final stage of the acceleration, up to 7 TeV, takes place. The above sequence of accelerations is shown in Figure 2.2.

Inside the LHC, in addition to the increase of the energy, a main concern is to maintain the beam of protons in circular orbit and to avoid deviation of particles from it, due to electrical repulsive forces. This is achieved by a strong -given the high energy values- magnetic field. Specifically, there is a series of superconductive bipolar magnets,

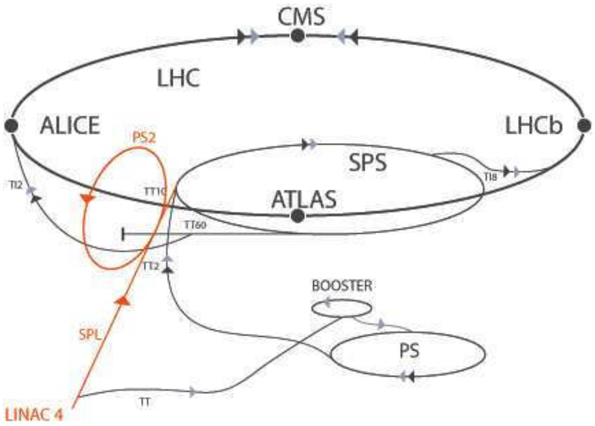

Figure 2.2: The LHC accelerating systems

which create a field larger than 8 T. It is obvious that two such magnetic systems with opposite direction are required, in order to focus the two oppositely charged and conversely moving beams.

In Table 2.1 some details of the LHC design are presented[1].

2.2 LHC experiments

In this section, a brief description of the five LHC experiments is given. The sixth one, ATLAS, since it is the one on which this thesis is based on, is being analyzed in more detail in a following section.

The general operation of a detector in a collision experiment is as follows: First, the particles produced in the interaction point are entering a magnetic field. The purpose of this field is the bending of the particle track, for those particles that are electrically charged, which leads to the calculation of their momentum: the greater the latter, the less the curvature. This measurement takes place in the first part of the detector crossed by the particles in their path, the Tracker Detector. There, the initial part of the track of each particle is reconstructed and, also, their momentum and their charge is determined (oppositely charged particles obviously obtain opposite curvatures). Thereafter, the particles pass through the calorimeters. Moving outwards, the first one to be passed

---

[1] Table taken from http://www.lhc-closer.es/ : Taking a closer look at LHC - GLOSSARY

LHC parameters	
Circumference	26659 m
Dipole operating temperature	1.9 K
Number of arcs (2450 m long)	8
Number of lattice cells per arc	23
Number of straight sections (545 m long)	8
Main RF System	400.8 MHz
Number of magnets (dipoles, quadrupoles ... dodecapoles)	9300
Number of dipoles	1232
Number of quadrupoles	858
Number of RF cavities	8 / beam
Nominal energy (protons)	7 TeV
Momentum at collision	7 TeV/c
Momentum at injection	450 GeV/c
Nominal energy (ions)	2.76 TeV/nucleon
Peak magnetic dipole field	8.33 T
Current in main dipole	11800 A
Energy density of the LHC magnets	500 kJ/m
Main dipole coil inner diameter	56 mm
Distance between aperture axes (1.9 K)	194.00 mm
Distance between aperture axes (293 K)	194.52 mm
Main Dipole Length	14.3 m
Horizontal force at 8.33 T (inner and outer layer)	1.7 MN/m
Maximum current with NO resistence (1.9 K e 8.33 T)	17000 A
Maximum current with NO resistence (1.9 K e 0 T)	50000 A
Number de strands per cable	36
Bending radius	2803.95 m
Minimum distance between bunches	$\sim 7\,\text{m}$
Bunch spacing	25 ns
Design Luminosity	$10^{34}\,\text{cm}^{-2}\cdot\text{s}^{-1}$
No. of bunches / proton beam	2808
No. of protons / bunch (at start)	$1.15\cdot 10^{11}$
Circulating current / beam	0.54 A
Number of turns / second	11245
Stored beam energy	360 MJ
Stored energy in magnets	11 GJ
Beam lifetime	10 h
Average crossing rate	31.6 MHz
Number of collisions / second	600 millions
Radiated Power / beam (syncrotron radiation)	$\sim 6\,\text{KW}$
Total crossing angle (collision point)	$300\,\mu\text{rad}$
Emittance ϵ_n	$3.75\,\mu\text{rad}$
β	0.55 m

Table 2.1: A list of LHC parameters

is the Electromagnetic Calorimeter, where electrons and photons lay almost all their energy. Immediately after, those particles that have penetrated the Electromagnetic Calorimeter without being absorbed, will enter the Hadronic Calorimeter where they will stop. The only particles that pass by both types of calorimeters, without losing a significant part of their energy, are the muons. This is the reason why, in such experiments, there are, at the most outer part, specific devices for the identification of such particles, the Muon Detection System. The Muon System must be inside a magnetic field, as well. This helps to separate the muons from their antiparticles, since, due to their opposite charges, muons and antimuons are curved into opposite directions. Through the radius of the curvature, one can estimate the momentum of the incoming particle.

Figure 2.3 shows the path followed by the different particles in their passage through the detector.

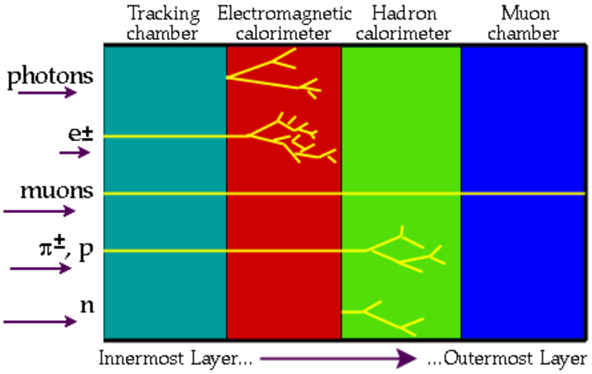

Figure 2.3: Schematic representation of particles passage inside a detector

This is the mode of operation of the two major experiments to be performed at the LHC, ATLAS and CMS. Their differences lie mainly in the choice of the technology used in their manufacture.

2.2.1 CMS

CMS [24], like ATLAS, is a general purpose detector which aims to study all possible physics that can be provided by LHC. The main feature of the CMS detector is a tubular superconducting magnet which gives the whole detector its name (Compact

Muon Solenoid). The magnet has a length of 13 m and a diameter of 5.9 m (Figure 2.4). It is made of a coil of superconducting material, which creates a magnetic field around 100.000 times stronger than that of Earth. It is the biggest magnet of this type ever built and its size allows the installation in the interior part of the Tracker and the two types of Calorimeters.

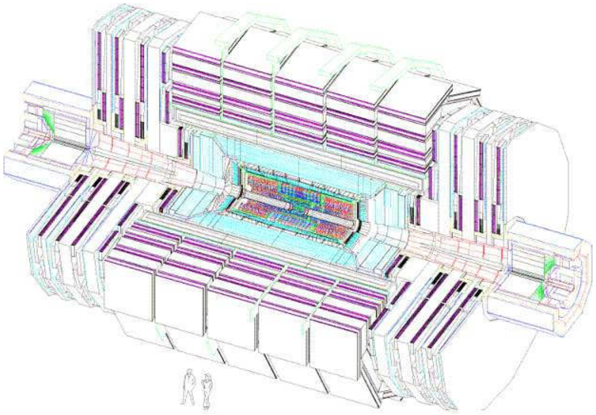

Figure 2.4: The CMS detector

The Tracker identifies the tracks of the particles. To do this, measurements of the position are taken with such precision, that ultimately the track can be well identified with the use of only a few points. Each spatial measurement of particles has a precision of 10 mm. Since, as the innermost part of the detector, the Tracker will receive the largest amount of data -thus radiation- the detector design was such that ensured great resistance to radiation for this subsystem. More specifically, the Tracker of the CMS detector consists entirely of silicon. The individual sections are the pixels (in the inner part) and the silicon microstrip detectors that surround the latter. These subsystems, when being crossed by a particle, produce small electrical signals which are then enhanced and measured.

The Electromagnetic Calorimeter, which is a homogeneous calorimeter of $PbWO\_4$ crystals, produces a light pulse when penetrated by electrons and photons. The light produced is proportional to the energy of the particle that passed. Specially designed light detectors are attached to each crystal to convert light into electrical signals, which are then enhanced in order to be analyzed.

After the Electromagnetic Calorimeter, the particles are entering the Hadronic one. The Hadronic Calorimeter of the CMS detector is a sampling calorimeter, which has the ability to measure the position of a particle as well as its energy and time of arrival, using alternating layers of absorber and scintillator, through light pulse production. This light is collected by optical fibers and then treated appropriately. The Hadronic Calorimeter is divided into sectors, the central (barrel) and two endcaps on the two sides. The barrel consists of 36 sections, weighing 26 tons each, while the same number of sections forms the endcaps.

Finally, the outermost part of the detector is where the Muon Detection System is located. It consists of four layers of gas detectors, situated between iron plates. The role of these layers of iron is to provide the return of the magnetic field (return yoke) and to absorb those hadrons that did not stop in the Hadronic Calorimeter.

2.2.2 ALICE

As already mentioned, the ALICE detector [25] studies mainly the collisions of heavy ions -namely lead ions- with a view to the discovery of quark-gluon plasma. In such a study, a critical measure is the ability to identify particles, which, in this case, is performed by the measurement of time of flight, the measurement of energy loss $\mathrm{d}E/\mathrm{d}X$, the transition radiation and finally the Cherenkov radiation.

A schematic view of the detector is shown in Figure 2.5. It consists of a central part (barrel), with a muon spectrometer on one side. A set of cylindrical detectors (ITS Drift, ITS Strips, TPC, TRD), within a magnetic field, form the Tracker of the experiment. These detectors identify the location of each particle using more than 100 points and provide tracks of great accuracy. The role of the magnetic field detector is crucial, since it provides the necessary curvature of the tracks.

The Electromagnetic Calorimeter of ALICE is a sampling calorimeter. The structure is based on the use of lead and scintillator that alternate. Each basic unit (module) consists of four towers of such layers. A total of 12×24 modules make up a super module. There are in total 11 super modules, which give a number of 12.672 towers, and provides high partition (granularity). Each of these towers can be read independently by special fibers.

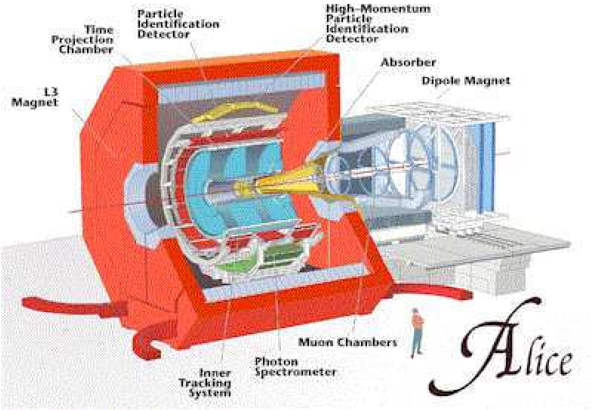

Figure 2.5: The ALICE detector

After the Electromagnetic Calorimeter comes the Muon Spectrometer. This can study the full range of heavy quarkonia $(J/\Psi, \Psi', Y, Y', Y'')$, through their decay to a pair of muons $(\mu^+\mu^-)$.

In terms of pseudorapidity, the ALICE Muons Spectrometer covers the area $2.5 < \eta < 4$. The resolution in the invariant mass is of the order of 70 MeV, for the mass region of J/Ψ, and approximately 100 MeV for Y. These values allow individual measurement for all five possible resonances.

2.2.3 LHCb

The smallest of the four main experiments of the LHC accelerator, LHCb [26] is devoted entirely to the study of the physics of the b-quark. In this case, the correct selection of events containing B-mesons is very important, given the enormous number of events that are being generated inside the accelerator. Therefore, emphasis was given in the creation of an efficient trigger system. The schematic view of the detector is shown in Figure 2.6.

B-mesons have the property not to flee in all directions after their formation, but, in contrast, to be close to the beam axis. This fact played an important role in the design of the LHCb detector. Thus, unlike other detectors in the LHC, the LHCb extends 20 m in length around the beam axis, with the various subsystems following one another in a straight line.

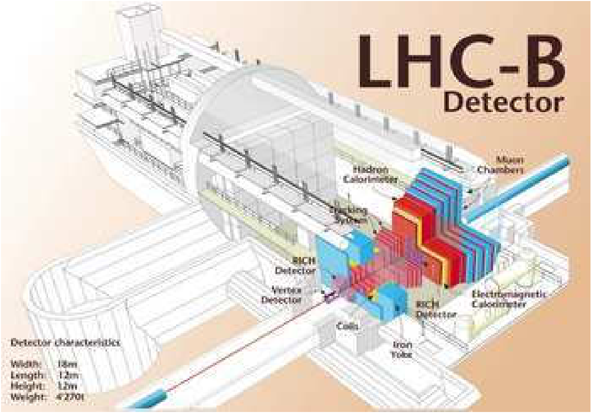

Figure 2.6: The LHCb detector

First comes the VELO (VErtex LOcator). This device selects the B-mesons between the total number of particles that are formed in the accelerator. For this purpose, its 42 silicon detectors are located 5 mm from the interaction point. VELO measures the distance from this point (that is, the point of the formation of the B-meson) to the point where the B-mesons decay. The precision of the system is of the order of 100 mm.

The next subsystems are the two RICH (Ring Imaging CHerenkov) detectors. They measure the Cherenkov radiation of charged particles passing through the interior and calculate their speed. Then, in conjunction with other measurements, they determine the mass, charge and ultimately the kind of particle. The two RICH detectors are responsible, therefore, to detect a range of particles that come from the decay of B-mesons.

The system of track identification consists of a set of four stations and it possesses two detectors with different technologies. The Silicon Tracker uses microstrip silicon detectors for particle detection. The Outer Tracker is positioned away from the beam and consists of hundreds of gas pipes, so the particle is detected by the ionization it causes to the gas molecules.

The Calorimeters, both the Electromagnetic and the Hadronic ones, are constructed using a sandwich structure with layers of metal and plastic plates. The collision of the incoming particles with the metal plates creates new particles, which excite the molecules of plastic plates, resulting in the emission of ultraviolet light.

Finally, the Muon Spectrometer (which is very important, since very often the final states of B-mesons lead to muons), located at the end point of the LHCb detector, consists of five plates of various sizes, each of which is filled with a combination of three different gases: carbon dioxide, argon and tetrafluoromethane. The muons that are penetrating those stations react with the mixture of the gasses and are, thus, being identified.

2.2.4 TOTEM

The TOTEM experiment [27] aims to accurately measure the cross section of proton-proton interactions, as well as to perform an in-depth study of the structure of the proton. It examines the physical processes that take place in the region near the axis of the beam and will be an excellent additional study beyond the general one of two major experiments. In the case of elastic and (most) diffractive events, intact protons in the final state need to be detected at a small angle relative to the beam line. The TOTEM detector (Figure 2.7) is designed in order to provide high acceptance in a region with such large flow of events such as the forward region. TOTEM detects particles coming from the proton-proton interaction, at Point 5, and also provides good triggering for the most important amongst them.

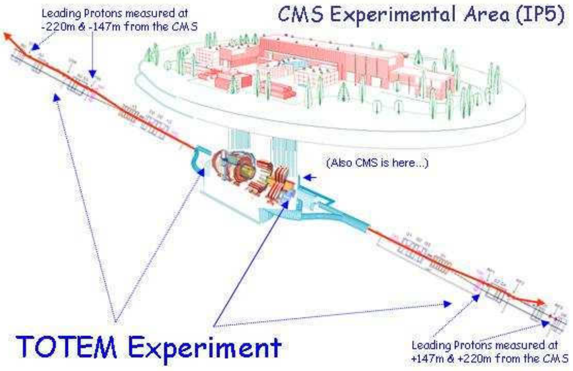

Figure 2.7: The TOTEM detector

The Totem detector consists of three different kinds of subdetectors. First come the Roman Pots (RPS) which have the ability to move along the axis of the beam. Each station consists of two units, located 4m from one another. Each unit consists of two sensitive detectors in a cylindrical housing (known as pots), attaching the beam from above and below and another one that moves horizontally. They are located in both sides of the Interaction Point 5, where the CMS detector is also located, and at some distance from the latter. In the cavity of CMS there are placed the other two subdetectors of the experiment. These two types of particle telescopes (T1 and T2) are located at 10,5 and 13,5 m on either side of CMS. These telescopes fully cover the area around the axis of the beam and they can reconstruct the tracks of charged particles resulting from pp collisions, as well as identifying the primary vertex.

2.2.5 LHCf

The aim of the LHCf experiment [28] is to study the production of neutral particles in proton-proton collisions at very small angles around the beam axis (forward region).

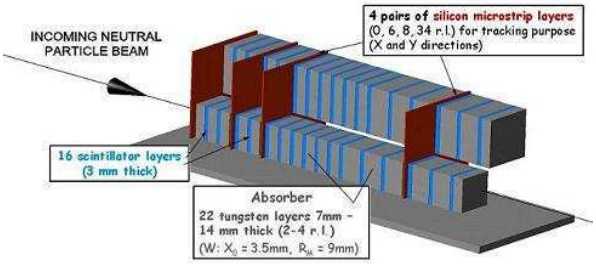

Figure 2.8: The LHCf Calorimeter

The detector consists of two small Calorimeters (Figure 2.8), which are located at 140 m from ATLAS interaction point. The two Calorimeters are more or less similar but differ in the sensors used in their construction. The first one has scintillating fibers (SciFi) and multi-anode photomultipliers (MAPMTs). The second one uses silicon strips instead. Each sub-detector has four pairs of sensors placed at various locations. The first two are used to detect the shower maximum of gamma-ray induced showers, while the other two deal with the hadronic showers, developed deep in the Calorimeter.

2.3 The ATLAS detector

ATLAS ([29],[30]) is one of the six in total experiments that takes place at the LHC. It employs almost 3000 physicists from 37 countries and from more than 179 universities and laboratories around the world. The decision to build it was first taken in March 1992, at a meeting in Evian-les-Bains, France, involving 600 scientists. There, EAGLE (Experiment for Accurate Gamma, Lepton and Energy Measurements) and ASCOT (Apparatus with Super COnducting Toroids) joined forces to proceed with the design and creation of an ambitious experiment that would take place at the LHC: this was the birth of ATLAS[2]. Several year later, in 1994, the design of the Detector was completed and the formal proposal for the new experiment was ready.

The assembly of the individual parts of the detector was performed in the several partner universities and institutes and their final assembly at the detector pit at CERN began in 2003. The construction was completed in 2008, when it began to collect the first data on September 10th, before the accident at LHC, 9 days later (9/19/2008), which resulted in the closure of the accelerator for about a year.

The detector of the experiment has a length of 44m and a width of 25 m, and weighs about 7000 tons (almost the same as the Eiffel Tower). It is composed of a number of individual sub-detectors. More specifically, like in any such detector, the main parts are the Tracker (named Inner Detector because of its position in the innermost part of the system), the Electromagnetic Calorimeter (Liquid Argon), the Hadronic Calorimeter (Tile Calorimeter) and finally the muon detection system (Muon Spectrometer), all placed within a strong magnetic field.

The University of Athens participates in ATLAS with two groups, one working on the Muon Spectrometer and another one on the Tile Calorimeter. In the preparation and construction stages, the first group was responsible for the assembly of 30000 BIS MDT tubes, while the second one was responsible for the assembly and the quality control test of the totally 10,300 Photomultiplier tubes that are used in the Calorimeter.

The following pages present the various subsystems of the ATLAS experiment. Particular emphasis is given to the description of the Muon Spectrometer, since this is the sub-detector on which mainly relies the study for the detection of the Z' particle.

The ATLAS detector, with all its subdetectors, is presented in Figure 2.9

---

[2] http://cerncourier.com/cws/article/cern/35867

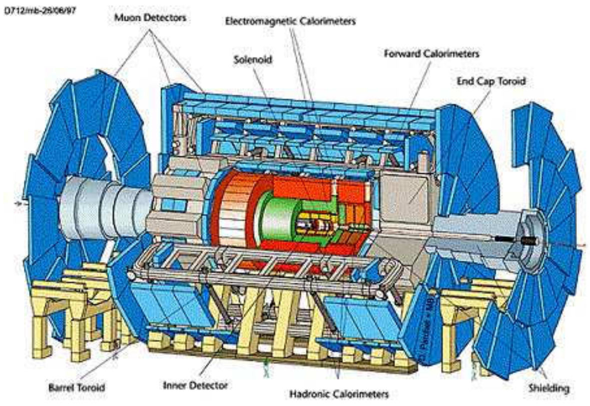

Figure 2.9: The ATLAS detector

2.3.1 Inner Detector

The Inner Detector (or Tracker) [31], [32] of the experiment has the main aim of identifying and measuring the tracks of the particles that are created in the interaction point. It is the first subsystem of the ATLAS detector, located at the innermost point. It consists of three different types of detectors that make it possible to detect and precisely measure the tracks of charged particles, among the huge number of tracks that will be created. More specifically, the three types of the Inner Tracking detector (Tracker) used are:

- Silicon semiconductor detectors (Pixel)
- Thin strips semiconductor detectors (Semiconductor Tracker - SCT)
- Transition radiation detectors (Transition Radiation Tracker - TRT)

In Figure 2.10, there is a schematic representation of the ATLAS Tracker, where the exact location of the various subdetectors can be seen.

2.3.1.1 Pixel

Pixel Detector provides very high granularity and gives very accurate measurements near the interaction point. Three measurements are provided throughout the acceptance region and the detector can also identify the impact parameters very close to

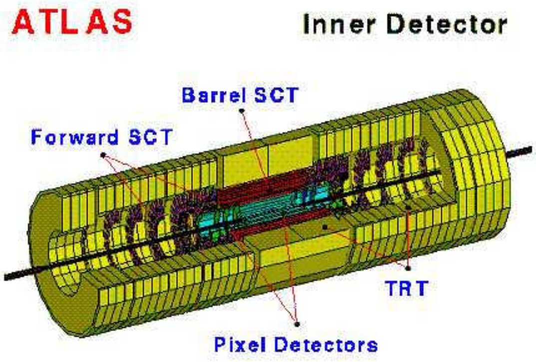

Figure 2.10: Schematic view of ATLAS Inner Detector

the point where the particles were created, allowing discovery of short-lived ones (e.g. B-hadrons).

The basic module of the detector is composed of a series of 16 chips connected to an appropriate sensor. The detector consists of three cylindrical layers (namely, layer 1, layer 2 and B-layer) in the central area with a radius of 50.5 mm, 88.5 mm and 122.5 mm (a total of 1456 modules) and three disks on the two lateral regions, with radii between 90 and 150 mm (288 modules in total).

The resolutions, averaged over a flat pseudorapidity distribution, are [33]:

- $\sigma(\mathrm{R}\phi) = 11\,\mu$m for barrel layers 1 and 2
- $\sigma(\mathrm{R}\phi) = 12\,\mu$m for the B-layer
- $\sigma(\mathrm{R}\phi) = 12\,\mu$m for the disks
- $\sigma(\mathrm{z}) = 69\,\mu$m for barrel layers 1 and 2
- $\sigma(\mathrm{z}) = 71\,\mu$m for the B-layer
- $\sigma(\mathrm{R}) = 77\,\mu$m for the disks

2.3.1.2 SCT

SCT forms the central part of the Inner Detector. It has an active area of silicon of totally about $61\,\mathrm{m}^2$ -more than 50 times larger than any other silicon detector- with a total of 6.2 million read channels. The spatial resolution is 16mm at the ρ-ϕ plane and 580 mm at z direction.

The modules consist of silicon sensors, connected together in pairs, in a solid angle of 40 mrad, and provide information on the hits in two dimensions. The SCT consists of four concentric layers in the central region, with a total of 2112 subdetectors. In the two sides, there are 9 disks in each, with 1976 subdetectors. The total system occupies an area of 5.6 m in length and 56 cm in radius. On average, four spatial measurements are taken for each track in the region of $|\eta| < 2.5$.

2.3.1.3 TRT

The TRT is responsible for determining the path followed by the particles, through reading the various hits they left in their way.

The TRT, in the outermost part of the Inner Detector, gives measurements of the track of charged particles through a total of more than 400,000 read channels. Moreover, it can identify the electrons by measuring the transition radiation. It is composed of a barrel and three end-cups on each side. Overall, it provides a total of 36 average measurements per track in the pseudorapidity region $|\eta| < 2.1$.

The main unit is the straw. It is a cylindrical drift tube, with a diameter of 4 mm and a length varying from 39 cm at end-cups up to 144 cm in the barrel. The gas mixture used consists of $70\%\,\mathrm{Xe} - 27\%\,\mathrm{CO_2} - 3\%\,\mathrm{O_2}$. It achieves a spatial resolution of about 170 mm at the ρ-ϕ plane.

The TRT also provides additional discrimination between electrons and hadrons, with a pion rejection varying with h between a factor of 15 and 200 at 90% electron efficiency [31].

2.3.2 Electromagnetic Calorimeter

Like any collider detector, the ATLAS Detector has two types of calorimeters, the Electromagnetic Calorimeter, responsible for detecting electromagnetic objects (electrons, photons) and calculate their energy, and the Hadronic Calorimeter, responsible for studying and measuring the energy of hadrons. Moreover, in the greater η region, there is also another Calorimeter, the Forward Calorimeter, which is a combination of the two above mentioned types of calorimeters.

The Electromagnetic Calorimeter [34] covers the pseudorapidity area $|\eta| < 3.2$. It makes use of lead as an absorber and Liquid Argon as the active material, while it possess an accordion geometry (see Figure 2.11).

It is divided into three sections, the Barrel, which covers the region $|\eta| < 1.475$, and the two End-Cups, with $1.375 < |\eta| < 3.2$. The barrel is composed of two identical pieces, separated by a gap at z = 0. Similarly, each end-cup is constructed by two "wheels", one internal and one external. The absorber of the calorimeter is made up entirely of lead, while the electrodes used to read the signals are made from kapton.

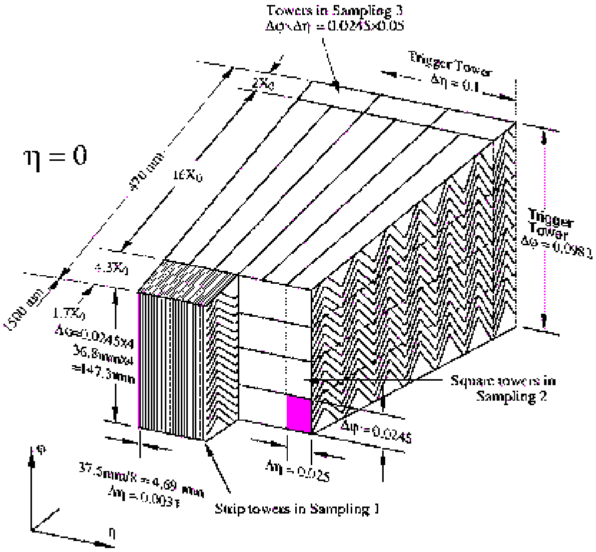

Figure 2.11: The accordion geometry of the ATLAS the Electromagnetic calorimeter

In the pseudorapidity region of $|\eta| < 2.5$, the Electromagnetic Calorimeter is divided into three sectors in the longitudinal direction. The first sector, of approximately

$6X_0$ length, operates as a pre-shower detector, allowing identification of the particles (separation γ/π_0, e/π, etc.) and determination of their position. The accuracy of the latter is based on the granularity achieved: $\Delta\eta \times \Delta\phi = 0.003 \times 0.1$. The middle sector is divided into sections of $\Delta\eta \times \Delta\phi = 0.025 \times 0.025$. Finally, the third sector has $\Delta\eta \times \Delta\phi = 0.05 \times 0.025$ and has a thickness ranging between $2\,X_0$ and $12\,X_0$.

The material penetrated by an interactive particle, before it enters the Electromagnetic Calorimeter, equals $2.3\,X_0$. In order, therefore, for the energy loss that the particle has undergone until its entrance to be taken into account (i.e. to be corrected) a presampler is used.

The accuracy in measuring the energy of the Electromagnetic Calorimeter is described by the following equation [34]:

$$\frac{\sigma_z}{E} = \frac{0.1}{\sqrt{E}} \otimes \frac{0.3}{E} \otimes 0.01 \tag{2.1}$$

2.3.3 Hadronic Calorimeter

The Hadronic Calorimeter of ATLAS consists of several parts: the Tile Calorimeter (Tile Cal), the Forward Calorimeter and the Liquid Argon Hadronic EncCup Calorimeter (LArHEC).

2.3.3.1 Tile Calorimeter

The Tile Calorimeter [35] is a sampling device, which uses steel as the absorption material, while a large number of scintillating tiles play the role of the active medium. These tiles are read by special fibers which are capable of shifting the wavelength of the incoming light (Wavelength Shifting Fibers - WLS). The innovation of this kind of calorimeter lies in the way the tiles are oriented: perpendicular to the direction of the colliding beams.

The structure of the Tile-Cal is cylindrical (see Figure 2.12). It consists of a central barrel (LB), with a length of 5640 mm, which is arranged along the axis of the beams, and two outer barrels (EB), each one 2910 mm in length, which are mounted on the two sides of the central part. The inner radius is equal to 2280 mm and the external one to 4230 mm (these numbers are common for all three barrels).

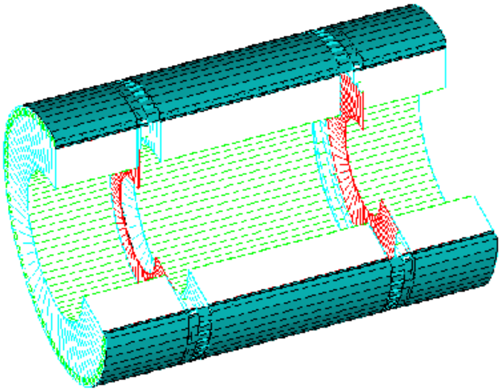

Figure 2.12: The cylindrical structure of the ATLAS Tile calorimeter

In the 60cm of the space between the central and the outer barrels, where the several electronic devices are hosted, there is a place for the Intermediate Tile Calorimeter (ITC). This is actually an extension of the Tile-Cal, which maximizes the amount of active material in this region.

The principle design of the Tile Calorimeter is shown in Figure 2.13. It consists of independent building units, of sphenoid shape, located in the azimuthal direction. These units are composed of steel plates of two different sizes, which alternate. The gaps between the steel plates is where the scintillating tiles are placed, as well as the optic fiber optics used for reading (two fibers per plate).

A multitude of such units (19 for LB, 10 for the EB) are linked together to create a total of 64 basic structures that make up the three sections of the calorimeter. The structure is completely periodic and allows the construction of a massive detector, by simply assembling a large number of smaller models.

The reading process in the Tile Calorimeter is as follows: an ionizing particle crosses the plate, causing the creation of ultraviolet light. Due to the scintillator, this light switches to the visible light region and it then spread to the edges of the tile. There it is being absorbed by the optical fibers, which have the ability to shift it to even larger wavelengths. This way, it falls within the sensitivity range of the total 10 300 photomultiplier of the calorimeter, to which it is lead.

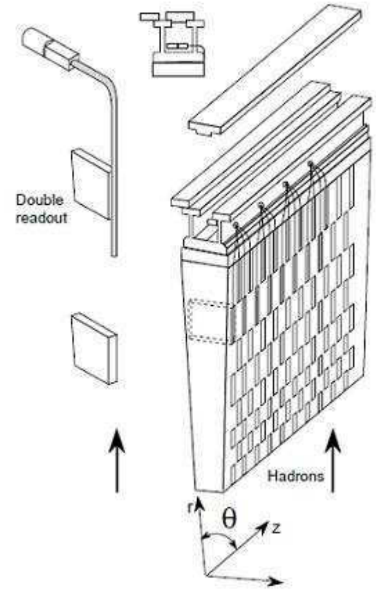

Figure 2.13: The principle design of ATLAS Tile Calorimeter

2.3.3.2 Liquid Argon Hadronic End-Cap Calorimeter

The Liquid Argon Hadronic End-Cap Calorimeter [36] is a sampling device, with copper as the absorbent and liquid argon as active medium, which are arranged in parallel. The pseudorapidity region that is covered is $1.5 < |\eta| < 3.2$.

It shares each of the two liquid argon end-cap cryostats with the electromagnetic end-cap and forward (FCAL) calorimeters.

The LArHEC calorimeter consists of two cylindrical wheels in each ATLAS end-cap cryostat (i.e., four wheels in total): a front wheel (HEC1) and a rear wheel (HEC2). Each one of the wheels is constructed of 32 identical wedge-shaped modules. The HEC1 modules are made of 25 copper plates, while the HEC2 modules are made of 17 copper plates. The thickness of the plates is different for the different type of wheels: 25 mm for HEC1 and 50 mm for HEC2 (the front plates of each wheel has half the thickness of the others). The inner radius is 475 mm for all wheels, apart from the first 9 plates of HEC1 where it is 372 mm. The 475 mm inner radius region provides the place for the Forward Calorimeter (see Section 2.3.4). The outer radius is 2.03 m and the length of the gap between the plates is common everywhere: 8.5 mm.

The resolution for jets for the Liquid Argon Hadronic is expected to be:

$$\frac{\sigma_E}{E} = \frac{0.5}{\sqrt{E}} \otimes 0.03 \tag{2.2}$$

2.3.4 Forward Calorimeter

For the Forward Calorimeter [37] a new technology is used. It consists of cylindrical electrodes (rod structure), which are suitable for the high-radiation environment within which the Calorimeter is located.

More specifically, the Forward Calorimeter is located very close to the beams and, regarding the pseudorapidity, it covers the region between 3.1 and 4.9. The position in which it is located, adjacent to other calorimetric devices and close to the interaction point, has many advantages, such as to cover gaps in the system in terms of calorimetry (seamless calorimetry) and it also provides a natural shield for the muon system.

The Forward Calorimeter is a complex calorimeter, providing both types of calorimetry (electromagnetic and Hadronic). It consists of an electromagnetic sector (FCal1), which is followed by two Hadronic ones (FCal2 and FCal3). The first uses copper as absorber, while the other two use tungsten. The active means, in both cases, is liquid argon.

A representation of the ATLAS Forward Calorimeter can be seen in Figure 2.14.

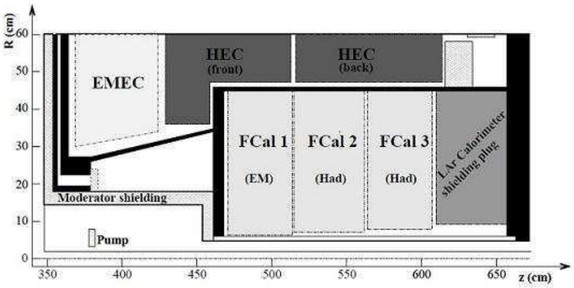

Figure 2.14: Schematic representation of the ATLAS Forward Calorimeter

2.3.5 Muon Spectrometer

The muon spectrometer of ATLAS forms the outer part of the detector, inside of which all the other subsystems (Inner Detector, Electromagnetic and Hadronic Calorimeters) are located.

The Muon Spectrometer will not be described here, since a later section (2.4) is entirely dedicated to it.

2.3.6 Magnet System

The magnetic sytem of ATLAS [38] is composed of two distinct parts. The first one is the Central Solenoid, which is responsible for producing a nearly uniform magnetic field in the Inner Detector. The second part is the Toroid, which plays a crucial role on the Muon Spectrometer function.

A schematic representation of the magnetic field can be seen in Figure 2.15.

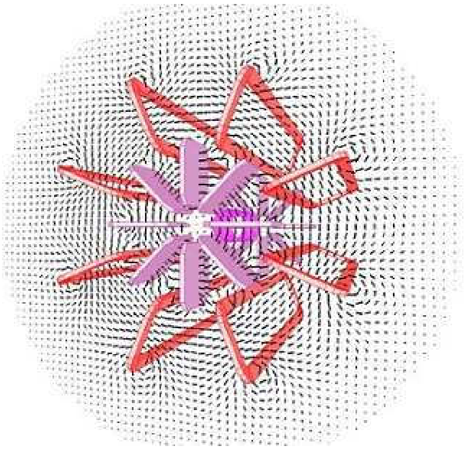

Figure 2.15: ATLAS Magnetic Field

2.3.6.1 Central Solenoid

The central Solenoid of ATLAS [39] (a photo of which is presented in Figure 2.16) is the first component of the magnetic sytem and is located just outside the Inner Detector. It consists of a central coil (weighting almost 5 tonnes) which contains almost 9 kilometers of superconducting wire an it is cooled by liquid helium. An electric current of 8,000 Amperes produces an axial magnetic field of an intension of 2 Tesla.

It has a total length of 5.3 m and a diameter of 2.3 m. Its construction makes use of the minimim material thickness possible, since the Solenoid is surrouned by the Electromagnetic Calorimeter and it should not affect the good performance of the latter.

Figure 2.16: The ATLAS central Solenoid

2.3.6.2 Toroid

The ATLAS Toroid is responsible for generating the appropriate magnetic field for the identification and determination of the muon tracks through the Muon Spectrometer. It covers the pseudorapidity area $0 < |\eta| < 2.7$.

The toroid is divided into three sections, the central toroid (barrel toroid), with a length of 25 m and a diameter of 20.1 m and the two end cups, with a length and a diameter of 5.0 m and 10.7 m respectively. The end-cups enter the two ends of the central toroid, forming an angle of 22.5 degrees.

The barrel Torroid is presented in Figure 2.17. Each of the three sections consists of eight coils, which are arranged radially and symmetrically around the beam axis. Regarding the pseudorapidity, in $|\eta| < 1.4$, the magnetic bending is provided by the central toroid. In contrast, for values of η between 1.4 and 2.7, the end-cups are

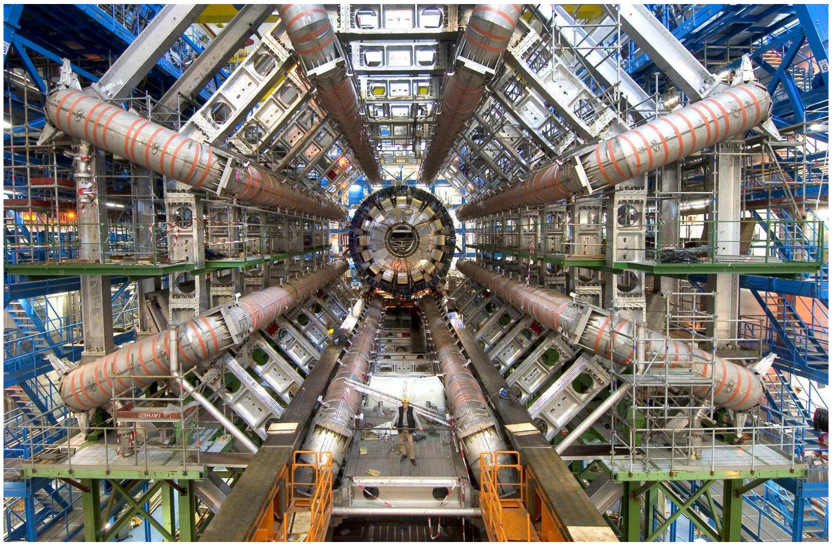

Figure 2.17: The ATLAS barrel Toroid

responsible for the bending. In the intermediate range of pseudorapidity (transition region), $1.4 < |\eta| < 1.6$, there is a combination of the two fields.

The created magnetic field is, in the bigger part, orthogonal to the muon trajectories. The same type of field is responsible for minimizing the losses caused by the multiple scattering that undergo the particles, during their passage through the detector.

The efficiency of the magnetic field, in terms of the bending power, is characterized by the integral $\oint B \cdot \ell$ (with B being the azimuthal component of the field intensity). The integral is taken along a straight line between the inner and outer radius. This integral is not stable, but it depends on the pseudorapidity. In the central part of the detector, the integral varies between 2 and 6 $\mathrm{T} \cdot \mathrm{m}$ and in the end-caps between 4 and 8 $\mathrm{T} \cdot \mathrm{m}$. The variation of the bending power in terms of eta is shown in Figure 2.18(a).

The shape of the field is not perfectly toroidal, but displays a ripple, as shown in Figure 2.18(b)

The toroidal magnetic field is responsible for the high spatial coverage of the Muon Spectrometer, as well as for its high resolution.

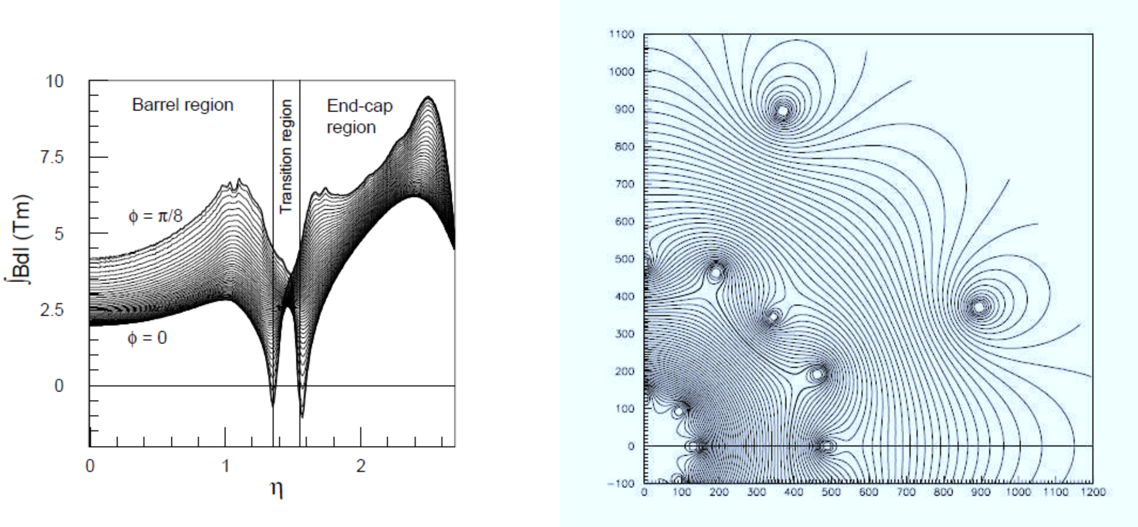

(a) (b)

Figure 2.18: Torroid field details: Bending power $\int B d\ell$ vs. η (left), Field map in the transition region (right)

2.3.7 Trigger system

Due to the huge data flow that ATLAS has to deal with (of the order of billion collisions per second), a specialized trigger system is necessary, in order to select only the most interesting, in terms of physics content and new discovery potential, events.

The Trigger System of the ATLAS detector ([40],[41]) does the selection in three levels. Each trigger level refines the decisions made at the previous level and, where necessary, applies additional selection criteria. Starting from an initial bunch-crossing rate of 40 MHz (interaction rate $\sim 10^9$ Hz at a luminosity of $10^{34}\text{cm}^2\text{s}^{-1}$), the rate of selected events must be reduced to ~ 100 Hz for permanent storage. While this requires an overall rejection factor of 10^7 against minimum-bias processes, excellent efficiency must be retained for the rare new physics that is expected in ATLAS.

2.3.7.1 Level-1 Trigger

The level-1 (LVL1) trigger makes an initial selection based on reduced granularity information from a subset of detectors.

The high P_T muons are identified using only the Trigger muon chambers, resistive-plate chambers (RPCs) in the barrel and thin-gap chambers (TGCs) in the endcaps of the Muon Spectrometer. The calorimeter selections are based on reduced granularity information from all the ATLAS calorimeters (electromagnetic and hadronic; barrel, endcap and forward). Objects searched for by the calorimeter trigger are high P_T electrons and photons, jets, and taus decaying into hadrons, as well as large missing and total transverse energy.

It requires about 2 micro-seconds to reach its decision, including the propagation delays on cables between the detector and the underground counting room where the trigger logic is housed. All of the information from the detector must be stored in pipeline memories until the LVL1 decision is available.

From the 40 million bunch crossings per second, less than 100,000 pass LVL1.

2.3.7.2 Level-2 Trigger

The LVL2 trigger must work at the LVL1 accept rate with an average event treatment time of $\sim$ 10 ms.

In order to operate within this time interval, the LVL2 trigger will use a sequence of highly optimized trigger selection algorithms which operate on only a fraction (typically 2%) of the event data. The LVL1 trigger identifies regions in the detector where it has found interesting features (the so-called Regions Of Interest -RoI). The RoI Builder (RoIB) combines the RoI information from the various parts of the LVL1 trigger and passes it to the LVL2 supervisor (L2SV). The L2SV allocates an event to one of the computing nodes in a PC farm and transfers the RoI information for the event to the allocated processor. These RoIs are then used to seed the LVL2 algorithms.

Less than 1000 events per second pass LVL2.

2.3.7.3 Event Filter

The Event Filter works at the LVL2 accept rate with an average event treatment time of about 1 second.

The EF receives fully built events and so the entirety of the data is available locally for analysis. All the selection processing for a given event is done in a single processor of the EF processor farm.

Events not selected by the EF are deleted and those accepted are passed on the appropriate storage system for offline analysis.

2.4 ATLAS Muon Spectrometer

In this section, great emphasis is given on the description of the Muon Spectrometer of ATLAS [42], since the present study refers to the Z' decay in a pair of muons. The Muon Spectrometer is therefore an essential tool for studying the possible discovery of this new boson.

The study of procedures that give two leptons at the final state will play a crucial role in discovering new physics. Especially, processes leading to muon-antimuon pair production are very promising, given the small probability of interaction within the detector (muons are Minimum Ionizing Particles, thus they can propagate at a very long distance from the interaction point, without losing, in the majority of cases, a significant amount of their energy), the purity of the signal and also their relatively small -and, in general, easily restricted- background. The muon spectrometer is an excellent and very effective tool towards this direction, which ensures on one hand the triggering of events with highly energetic muons in the final state and, on the other hand, the identification and the study of the motion of these muons.

The muon spectrometer of ATLAS forms the outer part of the ATLAS detector, inside of which all the other subsystems (Inner Detector, Electromagnetic and Hadronic Calorimeter) are located. It is composed of a very large number of different types of detectors, located inside the magnetic field of the Toroid.

The several detectors lie within this field. There are two types of detector chamber forming the spectrometer: the trigger chambers, used for triggering the muons, and the precision chambers, which are responsible for determining the tracks. Each of these two categories consists of two different types of detectors.

The triggering chambers are the RPCs (Resistive Plate Chambers), three levels of which are located in the central toroidal, and the TGCs (Thin Gap Chambers), with three levels in the end-caps. The muon trigger chambers measure the muon tracks with a spatial resolution of about 1-2 cm.

The second category is the precision chambers. Accurate measurement of muon tracks is performed through three layers of such chambers, which are the MDTs (Monitored Drift Tubes) in almost all the volume of the spectrometer and the CSCs (Cathode Strip Chambers) in the forward region, for $|\eta| > 2.0$. The precision chambers provide the desirable resolution for the patricle tracks, of about 35 mm.

Figure 2.19 shows a schematic representation of the Spectrometer, where all types of detectors and their relative position within the Spectrometer can be seen.

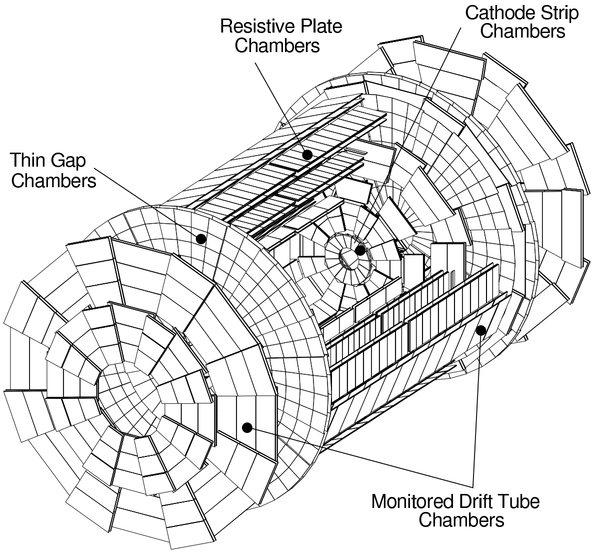

Figure 2.19: Schematic representation of the ATLAS Muon Spectrometer, with its different type detectors

The muon spectrometer of ATLAS can detect muons with transverse momentum above 3 GeV. The design of the subdetector is such as to measure the muon momentum with a spatial resolution of 3%, over most of the kinematic range, apart from very high momenta, where it increases to $\sim 10\%$. The high particle flux expected in the LHC (nominal luminosity of $10^{34}\text{cm}^{-2}\text{sec}^{-1}$, which corresponds to a data acquisition rate of the order of GHz) was the determining factor in the design and implementation of the spectrometer.

The high spatial resolution of the chambers itself is not enough to provide the determination of momentum with high accuracy. To achieve this, it is necessary to have a continuous information on the location of the chambers inside the detector. The Muon Spectrometer of the ATLAS experiment is also characterized by the very high precision it provides on the determination of the location of the various chambers (accuracy better than $30\mu m$). This is achieved by a system of optical alignment monitoring sensors.

2.4.1 Muon Spectrometer Precision Chambers

2.4.1.1 Monitor Drift Tubes (MDTs)

The MDT is the main device used in the muon spectrometer to provide high precision measurements of the track and momentum of muons.

It is essentially a drift chamber. It consists of an aluminum tube, 30 mm in diameter and with a wall thickness of 400 μm, filled with a mixture of gas Ar/CO2 (93%/7%). In the inner part, there is wire of 50 mm diameter, made of a combination of Tungsten (W) and Rhenium (Re). The wire plays the role of the anode, while the walls of the tube this of the cathode. Like what happens in every drift tube, the passage of a charged particle from the interior generates electrons through ionization. The electrons, due to the voltage difference of 3080 V, move to the anode (the W-Re wire), producing secondary electrons. The drift time, which is the time taken for the electrons to reach the wire, allows to track the point from which the initial charged particle passed. The accuracy of the position determination is of the order of 100 mm.

In Figure 2.20, the drift tube operation in a magnetic field with the curved drift path can be seen.

The ATLAS detector has in total 380000 MDT tubes. These are positioned in groups, forming the MDT chambers (Figure 2.21). Three or four levels of tubes create a super-level. Two super-levels connected together create a chamber. Overall, there are 1194 such chambers in the Muon Spectrometer.

The MDTs cover the pseudorapidity region $|\eta| < 2.0$.

2.4.1.2 Cathode Strip Chambers (CSCs)

The CSC is a chamber with a big number of anode wires, which are located in equal distances from one another.

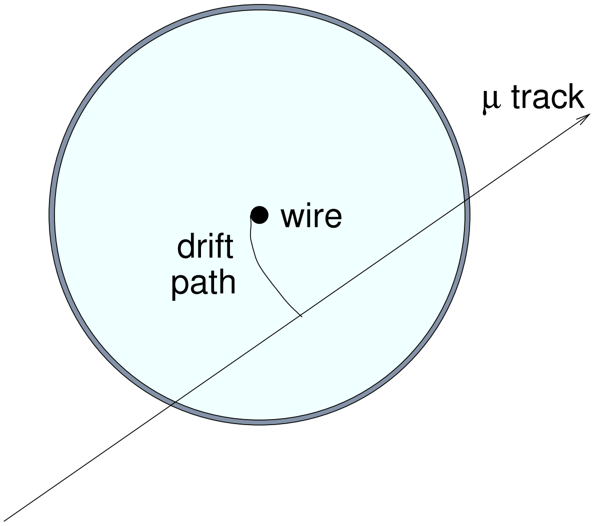

Figure 2.20: The MDT tube operation in a magnetic field

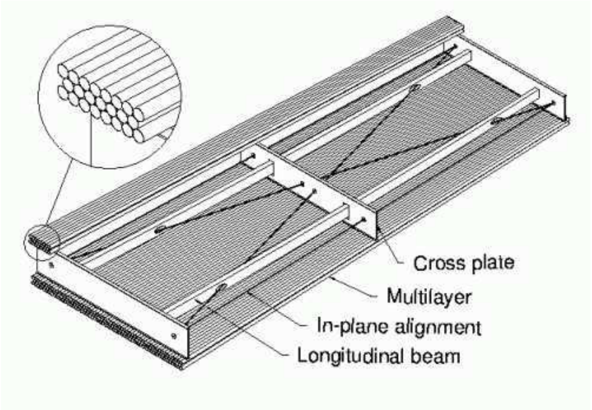

Figure 2.21: An MDT chamber

An intersection of a CSC can be seen in Figure 2.22. The charge induced by the anode is attributed to the cathode strips and, by measuring it, one can estimate the position of the passing particle. The cathode strips are oriented perpendicular to the anode and the precision achieved is of the order of 60 mm. The measurement of the vertical component is done by using another set of strips, parallel to the anode wires -this is the second cathode of the chamber. The gas mixture used in the chamber is a non-flammable mixture of Ar (30%), CO2 (50%) and CF4 (20%), with a total volume of 1.1 m^3. The fact that the gas contains no hydrogen, explains why the sensitivity of the detector to neutrons is small. This feature, combined with the small drift time ($< 30\,\mathrm{ms}$), makes CSCs very useful in areas with large rates of events: this kind of precision chambers are used to cover the region with $|\eta| > 2.0$.

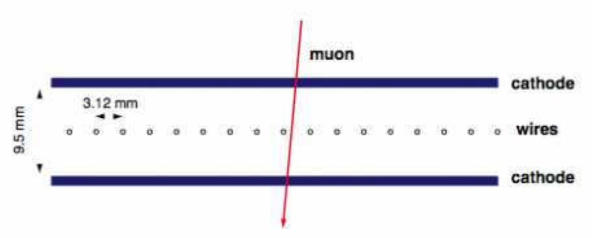

Figure 2.22: Intersection of a CSC chamber

2.4.2 Muon Spectrometer Trigger Chambers

2.4.2.1 Resistive Plate Chambers (RPCs)

The RPCs, like the TGCs (that are analyzed in the next paragraph), are used for muon triggering.

They are gas detectors that provide a typical spatial and time resolution of 1 cm × 1 ns. The basic unit consists of two parallel plates of Bakelite (Figure 2.23), within which there is a gas mixture with C2H2F4 as the main ingredient. The primary electrons, which are produced by ionization due to the passage of a charged particle, are multiplied under the influence of a large, uniform electric field of about 4.5 kV/mm. The electrical signals are then recorded using metal plates on both sides of the RPC.

A chamber is created by two vertical layers, each of which is read by two rows of strips, perpendicular to each other: one row is parallel to the MDT wires of the MDTs, so they are recording the bending of muons, while the second gives the position of the muon in the direction of the wire of the MDTs.

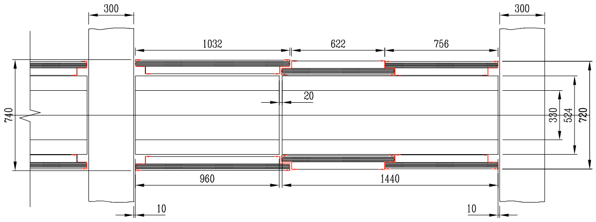

Figure 2.23: Structure of an RPC

2.4.2.2 Thin Gap Chambers (TGCs)

The last category of detectors used in the Muon Spectrometer of the ATLAS experiment are the TGCs (Figure 2.24).

These are designed like the multi-wired proportional chambers with a gas mixture of 55% CO2 and 45% n-C5H12. The signals from the anode wires, which are oriented parallel to those of the MDTs, provide the trigger information. There is also a contribution from strips in the vertical direction, which are measuring the spatial component in the direction of the wire of the MDTs.

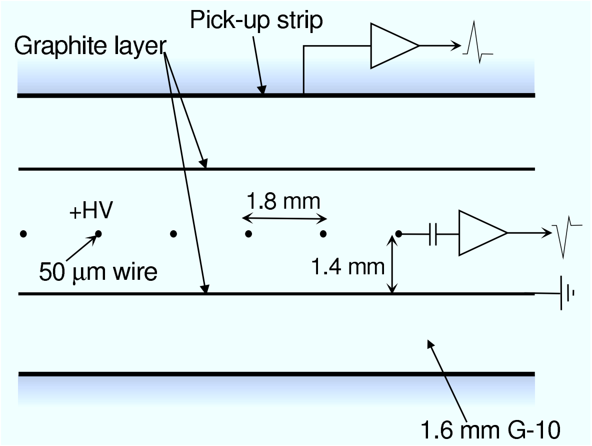

Figure 2.24: TGC structure

2.4.3 Muon Spectrometer Alignment

Since the measurements that will be taken from all the sub-detectors of the Muon Spectrometer require extremely high precision, it is of great importance for their position to be known with great accuracy. For this purpose, an optical alignment system has been developed, in order to continuously monitor all possible shifts or rotations of the system components that can take place throughout the data taking procedure.

A 1 TeV muon track is bent by the magnetic field such as that the corresponding sagitta varies from 500 μm at $\eta = 0$ to 1 mm at rapidity $\eta = 2$. Thus, in order to achieve the resolution of 10% for a muon with a momentum of 1 TeV, the sagitta should be measured with a precision of 50 μm. The single tube resolution of 100 μm (average over the drift distance) makes the MDT contribution to the sagitta error equal to 40 μm. Therefore, the additional error from the alignment of the MDT chambers must not exceed 30 μm in order to meet the specification ($\sqrt{30^2 + 40^2} = 50\,\mu$m).

The basic concept of the muon spectrometer barrel and endcap alignment system is based on two principles, for both the Barrel and the Endcaps.

- The chambers have internal alignment sensors that monitor their individual distortions.
- There is a global alignment system that monitors the positions of the chambers with respect to each other

Still, there are some slightly different strategies between barrel and endcaps, that are going to be described in the next paragraphs.

2.4.3.1 Barrel Alignment

In the ATLAS spectrometer, the MDT chambers and their auxiliary alignment devices are installed with a precision of about 5 mm and 2 mrad with respect to their nominal position. To achieve the accuracy of 30 μm, the alignment system of the barrel [43] determines the location of each chamber relative to that of its neighbors, both within an MDT layer and along the r-z trajectories within MDT towers (r is the radial coordinate).

The chambers of each layer are optically connected by the “axial” and “praxial” alignment systems in such a way that they form a “plane”. Then the three planes are directly connected by the projective alignment system which consists of a set of three-point alignment monitors -see Figure 2.25(a). The relative position of the chamber layers in the directions perpendicular to the projective direction, which is directly related to the measured sagitta of a high energy muon, is controlled by the projective system.

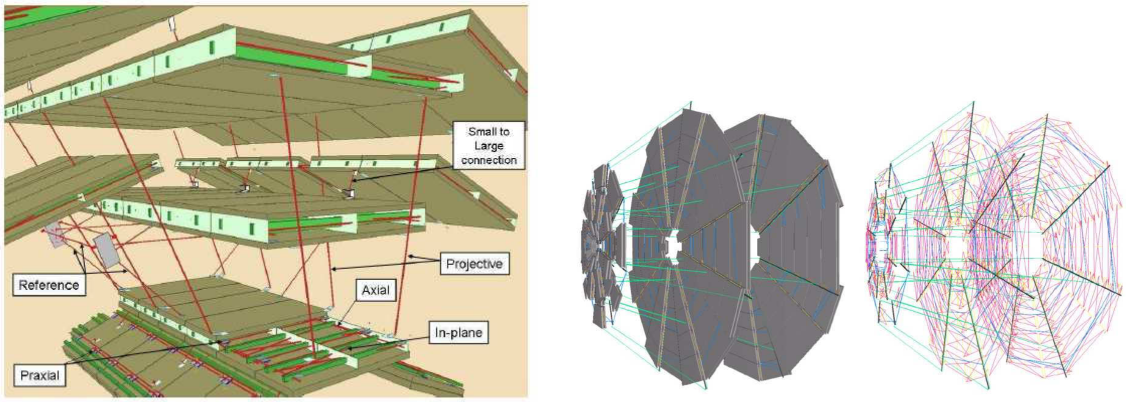

(a) (b)

Figure 2.25: Principle of the alignment of the ATLAS muon spectrometer. Left: Barrel, Right: EndCups

2.4.3.2 Endcap Alignment

The design of the alingnment system in the Endcaps [44] can be seen in Figure 2.25(b).

The global alignment system in the endcap establishes a reference grid using alignment bars whose relative positions are measured by a system of bar-tobar alignment sensors. Chamber positions are then related to the locations of the nearest bars with chamber-to-bar sensors. This information is used to provide corrections to the nominal chamber positions before calculating track sagittae.

Chapter 3

Muon Reconstruction and System Performance

One of the most interesting signatures of the new physics that may appear at LHC will be characterized by the presence of highly energetic muons.

The present work studies the decay of the Z' boson to two oppositely charged muons, so such a clear sign inside the detector is the basic tool of the analysis. The muons that come from the decay of Z' will have a large transverse momentum, due to the large mass of the new boson, and they are also going to appear isolated (by the term "isolated", we mean those particles that are not accompanied by additional activity in the surrounding area, as would be the case, for example, if they were part of a jet of particles).

It is therefore obvious that the correct reconstruction and identidication of the muons is a great tool to study new physics with the ATLAS experiment.

For many points of this chapter, Reference [45] has been used -unless otherwise stated.

3.1 ATLAS muon reconstruction algorithms

The ATLAS detector -and in particular the Muon Spectrometer- is designed to achieve momentum measurement with high efficiency and good resolution over a wide range of transverse momentum, pseudorapidity and azimuthal angle, while simultaneously providing stand-alone triggering capability.

Apart from the detector, important role in the muon studies play the corresponding software used to reconstruct them. In the ATLAS experiment there have been used two independent chains of algorithms for the identification, the reconstruction and the kinematic description of the muons, namely MUONBOY/STACO/MuTag [46] and MOORE/MUID [47].

3.1.1 MUONBOY/STACO/MuTag

The MUONBOY program was developed in order to cope with the challenging task of muon reconstruction in the ATLAS detector.

The strategy of the pattern recognition algorithm can be summarized in four main steps:

(a) identification of "regions of activity" in the muon system, through the trigger chambers

(b) reconstruction of local straight track segments in each muon station of these regions of activity

(c) combination of track segments of different muon stations to form muon track candidates

(d) global track fit of the muon track candidates through the full system

Another relevant task of the reconstruction is to perform backtracking from Muon System down to the beam region.

In order to combine the tracks reconstructed in the Inner Detector and the Muon System, the STACO program (the algorithm name is derived from the term "STAtistical COmbination") applies a strategy based on the statistical combination of the two independent measurements using the parameters of the reconstructed tracks and their covariance matrices.

Finally, the MuTag algorithm has been developed to tag low P_T muons. The principle is to start from the Inner Detector tracks, extrapolate them to the inner station of the Muon System, and try to match them with a segment reconstructed in these stations, not yet associated with a combined track.

An analytical description of the MUONBOY chain algorithms can be found in [46].

3.1.2 MOORE/MUID/MuGirl

MOORE, standing for "Muon Object Oriented REconstruction", is a software package for track reconstruction in the ATLAS Muon Spectrometer, developed in C++ in the ATHENA framework, according to modern Object Oriented design principles.

The MOORE structure is modular with a set of algorithms based on data objects that can be shared by different types of algorithms. It was designed to take full advantage of the ATLAS ATHENA offline framework and, in particular, adhere to the separation of data-like objects from algorithm-like objects. Thanks to its modularity, it could be very easily adapted both as Event Filter in the High Level Trigger environment and for the reconstruction of test beam data.

The reconstructed objects are tracks whose parameters are expressed at the first measured point inside the Muon Spectrometer. A full event reconstruction requires the extrapolation of the track parameters to the vertex. To accomplish this task the MUID (MUon IDentification) package is used.

The purpose of MUID consists in combining tracks found in the Muon Spectrometer with the corresponding Inner Detector ones. It takes the calorimeter information into account, in order to provide the best estimate of the kinematic parameters of the muons at the vertex. The first step is the extrapolation of tracks from the Muon Spectrometer to the vertex region, in order to have a set of track parameters comparable to those from the Inner Detector reconstruction. In this step, MUID accesses to the MOORE track and propagates it through the magnetic field in order to obtain the track parameters and their associated covariance matrix at the point of closest approach to the beam intersection. The multiple scattering in the Calorimeters is parametrized with a set of scattering planes; the muon energy loss is evaluated either from the calorimeters measurements or from a parametrization as a function of η and the muon momentum.

In the next step, Inner Detector and Muon tracks are matched by forming a χ^2 with five degrees of freedom from the parameter differences and summed covariance. A combined fit is performed for all combinations with a χ^2 probability above a certain cut. When no match satisfies this criterion, a combined fit is attempted for the best match around the muon track. Tracks are combined using hits from the two subdetectors which were found and used separately by the standalone reconstruction programs. All the matches to the Inner Detector giving a satisfactory combined fit are retained as identified muons.

All the above and even more details about the MOORE chain algorithms can be found in [47].

3.2 Parameters of a Muon Track

A track is fully reconstructed if all the parameters necessary for its determination are measured.

In order for a track to be fully determined, two things need to be known: its momentum and at least one point in space from which it passes. This means that a total of six parameters are required for each particle (the three coordinates of its position and three for its momentum). It is customary, however, to measure a track at the point of closest approach to the beam axis. This reduces the necessary parameters to five, instead of six: in the point of closest approach, the straight line that connects the primary vertex to the particle momentum vector is perpendicular to the momentum.

The parameters used to define the track of a muon are the following:

- $1/P_T$: The momentum is determined in this form, because the inverse of transverse momentum (and not the momentum itself) is what the system measures.

- ϕ : The phi angle in spherical coordinates

- tanθ: The tangent of the theta angle in spherical coordinates

- d_0: The transverse impact parameter (the vertical distance of the track from the beam axis, at the point of closest approach)

- z_0: The longitudinal impact parameter

3.3 Muon Reconstruction

3.3.1 Categories of Muon Reconstruction

The muons that appear in the experiment can be rebuilt using three different procedures. Both the Muon Spectrometer and the Inner Detector allow the reconstruction of trajectories of charged particles passing through them, so the various reconstruction processes can make use of the information of one of the systems at a time or the combined one.

In the first case, only the information from the Muon Spectrometer is used. Muons reconstructed this way are called “standalone muons”. The standalone muons are identified by reconstructing their trajectories at the Muon Spectrometer, and then extending them to the beam line. This reconstrucion procedure is followed for muons that fall outside the Inner Detector acceptance (i.e. possess a pseudorapidity of $|\eta| > 2.5$).

The second category is the “tag muons” . Here, the procedure is reverse. The reconstruction is performed using the information from the Inner Detector and then extending the track to the muon track system and seek close hits there (i.e., we are doing a matching between the Inner detector tracks and the track segments that appear in the Muon Spectrometer). This reconstrucion procedure is followed for low energetic muons, that can not reach the outer layers of the Muon Spectrometer.

The third category is essentially a combination of the above procedures and muons reconstructed this way are called “combined”. In principle, it consists of performing a comparison between the standalone muon tracks (reconstructed in the Muon Spectrometer) with those of the Inner Detector. Then, between the latter, those that have the required characteristics, in order to be considered as extension of the former, are selected. Therefore, the combined information is used, so that a single track is reconstructed.

Both reconstruction collections, MOORE and MuonBoy, are capable of using all the above mentioned techniques.

3.3.1.1 Reconstruction of Standalone Muons

For the reconstruction of standalone muons only the information from the spectrometer is used.

The reconstruction methods is based on initially building segments of the track in each of the three muon stations and then combine them in a final track. To extend the track back to the Inner Detector the effects of multiple scattering of muons and energy losses in the Calorimeters should be taken into consideration. The Muonboy calculates the energy loss based on the material penetrated by the muons in the calorimeter, while MUID additionally uses the measurements of the calorimeter where they are sufficiently larger than the most probable value and the muon appears to be isolated [48].

The standalone muons, compared with the other categories mentioned, have the advantage that the reconstruction can be done in a larger area of pseudorapidity η, compared with the η obtained when using the Inner Detector (eg. combined muons). While Inner Detector covers the region $|\eta| < 2.5$, the Muon Spectrometer has a slightly larger coverage ($|\eta| < 2.7$).

Of course, gaps in coverage appear in the locations of the various provisions of the detector, i.e. for $|\eta| \sim 0$ and $|\eta| \sim 1.2$ (see Figure 3.1[1]).

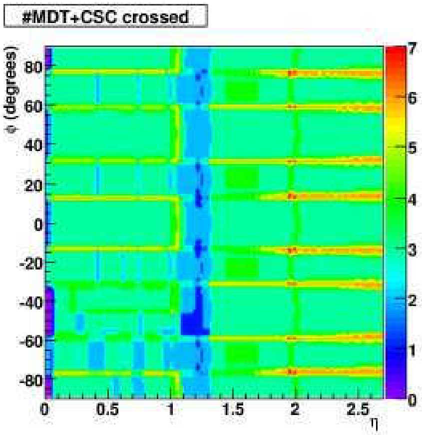

Figure 3.1: Gaps in Muon Spectrometer coverage, as a function of η and ϕ

---

[1] Figure taken from Reference [45]

One drawback of the standalone muon reconstruction is that it becomes difficult in the case of low energy muons, since it is hard for them to reach the outer layers of the spectrometer.

3.3.1.2 Track reconstruction in Inner Detector

The reconstruction of tracks in the Inner Detector is done, briefly, as follows: The points in the pixel and microstrip detectors from which the particle has passed are combined, so as to construct track seeds in the four inner layers of the Inner detector. The actual tracks are found by extending these seeds to add measurements from the outer layers.

The method gives excellent accuracy throughout the pseudorapidity area covered by the Inner Detector: $|\eta| < 2.5$.

3.3.1.3 Reconstruction of Combined Muons

The next step is to combine the measurements of the Inner Detector and the Muon Spectrometer, i.e. the tracks that have been reconstructed by the two subsystems.

What we want to to is to match to each track reconstructed by the muon system the one of the Inner Detector that fits it best. The muons that satisfy this condition (i.e. have a good couple of tracks) are called, as already mentioned, combined muons.

The good fit of the two individual tracks is being ensured by a match chi-square between them. More specifically, we consider the following format:

$$\chi^2_{match} = \left(\mathbf{T}_{MS} - \mathbf{T}_{ID}\right)^T \left(\mathbf{C}_{ID} - \mathbf{C}_{MS}\right)^{-1} \left(\mathbf{T}_{MS} - \mathbf{T}_{ID}\right) \tag{3.1}$$

In the above relation, $\mathbf{T}$ is a vector with the five orbital parameters (at the point of closest approach). Obviously, the ID index corresponds to the variables in the Inner Detector and the MS one to those of the spectrometer. $\mathbf{C}$ is the corresponding covariance matrix. So, in principle, what is being measured is the difference between outer and inner track vectors, weighted by their combined covariance matrix. Based on this variable, one can decide which pairs of MS and ID tracks will be accepted (that is to say, can be considered the one as continuation of the other), and also how good the matching between them is.

The difference between the two group of algorithms at this stage is that while STACO (from the MuonBoy side) makes a statistical comparison between the vectors of the two tracks to extract the one of the final track:

$$\mathbf{T} = \left(\mathbf{C}_{ID}^{-1} + \mathbf{C}_{MS}^{-1}\right)^{-1} \left(\mathbf{C}_{ID}^{-1}\mathbf{T}_{ID} + \mathbf{C}_{MS}^{-1}\mathbf{T}_{MS}\right) \tag{3.2}$$

MUID (from the MOORE side) does a partial refit: it does not directly use the measurements from the inner track, but starts from the inner track vector and covariance matrix and adds the measurements from the outer track. The fitting procedure accounts for the material (multiple scattering and energy loss) and magnetic field in the Calorimeter and Muon Spectrometer.

3.3.1.4 Reconstruction of Tag Muons

The algorithms used for the reconstruction of the tag muons are MuGirl (for the MOORE chain) and MuTag (for the MuonBoy one).

The basic idea is to extend the tracks from the Inner Detector towards the first station of the Muon Spectrometer and then check for neighboring segments of tracks there. MuTag estimates the χ^2 by measuring the difference between each part of the track segment in the Muon System and the corresponding prediction of the extended track of Inner Detector. Instead, the MuGirl uses a artificial neural network to define a discriminant. In both cases, if a track segment in the Muon System is close to the extension of the track of the Inner Detector, then this track is recognized as a tag muon.

There is an important difference in the way these algorithms are run in the standard reconstruction chain. MuGirl considers all Inner Detector tracks and redoes segment finding in the region around the track. MuTag only makes use of Inner Detector tracks and Muon Spectrometer segments not used by Staco. Thus MuTag serves only to supplement Staco while MuGirl attempts to find all muons.

3.3.2 Combining muons of different categories

It is obvious that the use of muons that are reconstructed with more than one ways may increase the system efficiency and performance and it also helps to better identify

-and thus reject- the fake muons.

In such a case, it is obvious that overlap should be avoided, i.e. care must be taken so as not to count as two muons, one muon that was reconstructed with several algorithms (of the same family). For example, standalone muons that are successfully combined are not recorded separately. If a standalone muon is combined with more than one Inner Detector track, exactly one of the muons is flagged as “best match”.

In the MUONBOY collection, the tagged and combined muons do not overlap by construction. In the MOORE collection, overlaps between MuGirl and MUID muons are removed by creating a single muon when both have the same inner detector track.

3.4 Performance evaluation

3.4.1 Truth matching

The performance of muon reconstruction is evaluated by comparing the reconstructed muons with the true ones.

The “true” muons are those within the Monte Carlo truth record. The muons included in the truth record are those which were created in the initial event generation (i.e., the muons coming straight from the Z' decay), but also secondary muons produced during propagation through the tracking volume. Those muons that are produced in the Calorimeter or within the Muon Spectrometer are not included. Apart from that, the truth record excludes as well the very low energetic muons (i.e., the ones with transverse momentum below 2 GeV/c). This is done in order to avoid spurious matches with candidates that are not expected to be reconstructed.

For every event, a one-to-one matching is performed between the reconstructed muons and those in the truth record. In general, the matching can be performed by using two different distance metrics. The first one is the reference distance D_{ref} measured from the true muon to the reconstructed one and is given by the following relation:

$$D_{ref} = \sqrt{\left(\frac{\phi_{reco}-\phi_{true}}{0.005}\right)^2 + \left(\frac{\eta_{reco}-\eta_{true}}{0.005}\right)^2 + \left(\frac{\frac{\Delta P_T}{P_T}}{0.03}\right)^2} \tag{3.3}$$

with:

$$\frac{\Delta P_T}{P_T} = \frac{1/P_{T,reco} - 1/P_{T,true}}{1/P_{T,true}} = \frac{P_{T,true} - P_{T,reco}}{P_{T,reco}} \tag{3.4}$$

The second metric is D_{eva}, the evaluation distance, and it is measured from the reconstructed muon to the true one:

$$D_{eva} = \sqrt{(\mathbf{T}_{reco} - \mathbf{T}_{true})\mathbf{C}_{reco}^{-1}(\mathbf{T}_{reco} - \mathbf{T}_{true})} \tag{3.5}$$

In the above equation $\mathbf{T}$ denotes the vector of the five track parameters (expressed at the distance of closest approach to the beam line), while $\mathbf{C}$ is the associated covariance matrix.

In this study, the matching between the reconstructed and the true muon takes into account only the spatial distance between them. More specifically, what is being tested is the angle formed by the momentum vectors of the two muons, the true and the reconstructed, i.e. the angle in the $\eta - \phi$ space:

$$Dr = \sqrt{(\eta_{true} - \eta_{reco})^2 + (\phi_{true} - \phi_{reco})^2} \tag{3.6}$$

Obviously, the distance Dr should have a value up to some maximum, in order for a pair of true and reconstructed muons to be characterized as associated to each other. In general, this maximum value is set equal to 0.05. The matching is carried out by first examining each reconstructed muon and assigning it to the nearest true muon, using Equation 3.6. The reconstructed muon is left unmatched if no true muon is found in a distance less than the maximum allowed value of 0.05.

The fact that, in this study, the transverse momentum is not taken into account in the Dr relation is useful for avoiding to reject (at least in a first approximation) the muons whose transverse momentum has been wrongly reconstructed (i.e., is much greater or much smaller than the corresponding true value), as well as those muons which have been reconstructed with the wrong charge (since, in these cases, the great value of ΔP_T would cause the rejection of the specific muon pair, which would have a relatively large Dr). Therefore, the use of Equation 3.6 also serves as a measure of how well our algorithm performs the muon reconstruction in terms of momentum.

In the case that more than one matchings can be found for a true muon (i.e. more than one reconstructed muons lie within a Dr distance less than 0.05), the reconstructed muon which is retained and considered as the pair of the true one examined is the one with the smallest Dr.

3.4.2 Track classification

True muons that are matched are said to be "found" and those left unmatched are "lost". Reconstructed muons are considered "real", if they are matched to a true one, and "fake", if unmatched (i.e. there is no muon in the truth record of the event that can be associated to the reconstructed one, in terms of the Dr distance).

These fake muons may correspond to true muons produced outside the tracking volume (e.g. in the calorimeter) and hence are not included in the truth record or even to other objects, such as jets, that are reconstructed by the Muon Spectrometer as muons.

3.4.3 Quality cuts of muons

In general, before proceeding to the analysis, one applies several quality cuts, in order to select the "good" muons in an event, possessing characteristics appropriate for the analysis.

Since the present study concerns massive particles (of the order of TeV), one obvious choice would be to retain muons with a relatively large transverse momentum. Other quality cuts could include the requirement for isolation, the test of the matching between the reconstructed and the true one or even the reconstruction category -for example, in general, it is customary to use the combined muons, so as to have the maximum amount of information possible about them.

The exact quality cuts applied in our Z' analysis will be described into detail in the corresponding chapter.

3.4.4 Performance measures

The performance measures include efficiency, fake rate, resolution and charge misidentification.

3.4.4.1 Efficiency

The efficiency corresponds to the fraction of true muons that are "found" (i.e. there is a reconstructed muon that can be matched to them).

It is applied after the matching procedure and typically evaluated for some kinematic selection. More analytically, one can plot, for example, the η distribution for the found true muons over the total true muon η distribution. The histogram of the division will correspond to the η efficiency (and respectively for other kinematic variables).

In general, for a sample, one can evaluate either the P_T-, η- or ϕ- efficiency or all three of them -see also Section 3.5.2.

3.4.4.2 Fake Rate

Another important aspect which characterizes the performance of the Muon Spectrometer is the "fake rate".

The fake rate is calculated with respect to the true information of the sample under investigation and is defined as the mean number of fake muons per event.

3.4.4.3 Resolution

The resolution is a measure that shows how well a kinematic variable of a reconstructed muon is estimated.

For a given variable r, the relation used is described by the following format:

$$\delta r = \frac{r_{true} - r_{reconstructed}}{r_{true}} = \frac{\Delta r}{r} \tag{3.7}$$

Five kinematic variables characterize a track, but the most usual choices for estimating the resolution are the transverse momentum and the pseudorapidity (in some rare cases also the ϕ angle can be used).

The usual procedure one follows, in terms of resolution estimation, is to plot the above distribution for all matched reconstructed muons and then fit it with a Gaussian. The resolution is then defined to be the σ of this fit.

The tails in the distributions are often more important than the core resolution itself and are characterized by evaluating the fraction of found muons in several tail categories. Namely, one checks the magnitude of this residual in a certain region of the distribution (eg., $|\delta r| > 1$) to see if it exceeds a specific percentage. This region could indicate, for example, the muons whose sign is incorrectly measured (which are called "mischarged") or even those for which the measured momentum is more than two times larger than the true value.

3.4.5 Charge misidentification

Another measure of the performance of the muon reconstruction is the quality of the reconstruction of the muon charge.

This is tested by comparing the charge (or, equivalently, the sign of the P_T) of the reconstructed muon to the associated one within the Monte Carlo truth record (after the "matching" procedure).

Misreconstruction and charge misidentification rates are around 0.01% for the combined muons instead of 0.1% for the standalone

3.5 Efficiency estimation methods

3.5.1 The Tag-And-Probe method

The "Tag-And-Probe" method, which has already been used successfully in the Tevatron ([49],[50]) is a method developed in order to estimate the efficiency of the Muon Spectrometer with the use of the real data. The name of the method is derived from the terms "Tag" muon and "Probe" track, the definition of which is given in the following.

The method is initially performed in the simulated data, in order to later estimate the efficiency of the real data taken from the experiment. The purpose of the following paragraph is to make an evaluation of the method and examine how well it can be applied in the experiment.

The basic idea is as follows. First of all, we require a clean signal with two muons in the final state. As such, we can use, for example, the (conventiontal) Z boson decay into two muons: $Z \rightarrow \mu^+\mu^-$. Then, in order to reduce the backgrounds, we combine a 'good' muon in the sample with all the Inner Detector tracks and we seek to find which pair (muon-track) gives an invariant mass within the mass region of the initial particle (here, Z boson) and, at the same time, have opposite charges. Then, we check whether the particular Inner Detector track can be identified with another reocnstructed muon in the event.

This measure gives the efficiency: out of the total number of tracks, we count how many were also reconstructed as muons. The several steps of the method are analyzed in the following paragraphs.

3.5.1.1 Tag Muon

We start by selecting every muon in the spectrometer, which meets certain quality criteria. The latter are:

1. A transverse momentum adequate large (usually of the order of $P_T > 20\,\text{GeV}$).
2. The muon should be combined, namely should have been "seen" by both the Muon Spectrometer and the Inner Detector (therefore, its pseudorapidity is automatically limited to $|\eta| < 2.5$, since this is the η coverage of the Inner Detector).
3. Even if the muon is combined, it should be "well" combined. This means that the fit between the parameters of two individual tracks (the Muon Spectrometer and the Inner Detector ones), that were associated to each other to form the final combined track, should have a match $\chi^2 < 100$, for five degrees of freedom.
4. The muon should be isolated, namely it should not be accompagnied by a lot of additional activity in the space around it.

A muon which meets the above criteria is called "Tag". Most muons in the $Z \rightarrow \mu^+\mu^-$ sample we use satisfy the above conditions; therefore, we can usually use two tag muons per event, which doubles the statistics.

3.5.1.2 Probe Track

The next step regards the Inner Detector. We request there an appropriate, “good” track, which should again satisfy certain criteria. Those are:

1. The transverse momentum, again, should be large enough (of the same order as the muon momentum).
2. The track should be isolated from any other activity in the Inner Detector. This is ensured by requesting the total transverse momentum in a certain cone around the track to be less than a small percentage of the track transverse momentum itself.

Every good track is then tested in combination with the tag muon, in order to see whether the pair can result to an invariant mass within the Z boson mass region. Usually, we let for a diversion of ± 10 GeV. The pair (muon and Inner Detector track) should also possess opposite charges.

If a track satisfies all above conditions, it is called “Probe” (so we have a “Tag-And-Probe” combination). In case we find two such tracks for a tag muon, we select the one that gives an invariant mass closer to the Z boson peak -namely to 91.2 GeV.

3.5.1.3 Identification of the track as a muon

The next step is to check whether the Probe track can be identified with another good muon in the event (the partner of the tag muon).

This is done by combining the track with all the other muons (except from the Tag one) and checking whether the pair track-muon lies within a small cone in dR, where:

$$dR = \sqrt{(d\eta)^2_{tag-probe} + (d\phi)^2_{tag-probe})} \tag{3.8}$$

What is being measured is the ratio of the probe tracks that have been reconstructed by the Spectrometer over the total number of the probe tracks in the test sample (and, later, the real data).

The Tag-and-Probe technique is not restricted to the measurement of the standalone reconstruction efficiency. It can, for instance, be used to measure the muon reconstruction efficiency of the inner detector or the trigger efficiency.

An analytical example of the Tag-And-Probe method will be presented in later chapters, where the main analysis on the ATLAS pp data is presented (chapters 4 and 5).

3.5.2 Generated Efficiency

The simplest way to measure the efficiency of the Muon Spectrometer with the simulated data is to use the information from the particle generator that produced the simulated samples (in other words, the truth information of each sample). This is called "generated efficiency".

The process to obtain the generated efficiency is very simple. Essentially, we measure the ratio of muons reconstructed from the Spectrometer (and follow, of course, some adequate selection criteria, for example a cut on the transverse momentum: $P_T > 20\,\mathrm{GeV}$) over the total number of muons generated (the true muons). For the true muons there are also some loose selection criteria. For example, a necessary cut that has to be applied on the true muons is the pseudorapidity cut: $|\eta| < 2.5$; this is done in order to avoid a fictitious reduction of the efficiency due to the limited η coverage of the Inner Detector, which affects the reconstructed -combined- muons.

Usually, we express the generated efficiency in terms of η and P_T. This is done by using two histograms for each case. First the η (or P_T, accordingly) for all the generated muons (that pass the imposed cuts) and then the η (P_T) of those true muons that have been matched (i.e., associated) with a reconstructed muon (usually, a combined one). The ratio of the two histograms gives the generated efficiency, in terms of η (P_T).

Chapter 4

ATLAS 2010 pp data Analysis

The present chapter describes the analysis that has been performed on the 2010 ATLAS pp data, at center-of-mass energy of 7 TeV.

4.1 Structure of data taking - Run Periods

The ATLAS experiment started taking real data in November 2009. After March 2010, the center-of-mass energy was raised to 7 TeV, which is half the designed maximum value and the world record, up to now[1]. It is anticipated that, after a long upgrade stop in 2012-2014, it will gradually reach its design energy of 14 TeV.

4.1.1 Run Periods and Subperiods

The data taken by ATLAS is divided to different parts. The primary division is done in "Run periods". The periods take their name from the 26 letters of the english alphabet (A-Z, e.g. Period D) and these names are expected to be repeated every year.

These periods are divided in "Subperiods". The subperiods within the same period are differentiated by numbers (e.g., subperiod H2). The definition of a new period/subperiod is based on the status of the detectors and the configuration of the beam. A change in the configuration like the number of the bunches or the spacing

---

[1] end of 2011

between the beams or the trigger objects or even some change in the configuration of the detector defines a new period -or subperiod.

Each subperiod is, in its turn, divided into runs. A run is a time interval of (constant) data taking, the length of which can vary from a few hours up to a few days. The runs depend on the status of the beam and they are, therefore, determined by the LHC. Every run is divided in luminosity blocks: they are fractions of the whole run with a duration of a few minutes.

4.1.2 Description of a run

The procedure of a run is as follows. First, LHC control room declares the existence of stable beams (which means that the data to be taken is useful for physics and the High Voltage in the detectors can be risen). After this notification, the Shift Leader has to ensure that every detector is in a state to take good physics data (i.e. the high-voltage of each detector has reached its nominal value). There is a short delay, which gives the detectors enough time to respond. The Shift Leader, from the Run Control desk, declares the “warm start” command[2]. This is the moment when the “ReadyForPhysics” flag is set and the actual data taking begins.

A similar procedure is followed when a run ends. At some point, LHC reports that it is about to remove the stable beams condition. The several detectors then should go down with High Voltage and we, thus, have a “warm stop” period (when the “ReadyForPhysics” flag is removed). When the whole system goes back to the not-taking-data state, the run is completed.

4.1.3 2010 data taking

ATLAS was taking 7 TeV p-p collision data from March 2010 until the end of October of the same year, when the Heavy Ion running started.

The results presented in this chapter involve all 2010 Periods of p-p collision data, which means that we are dealing with an integrated luminosity of the order of $42\,\mathrm{pb}^{-1}$. The details of those periods, along with the corresponding luminosities, are shown in

---

[2] so-called, because the run is technically already underway and ATLAS is triggering on cosmics

Table 4.1. The efficiency of the detector, in terms of the recorded luminosity, was of the order of 94% (see Section 4.12).

Period	Dates of data taking	no. of Runs	no. of Events	Integr. Luminosity (nb^{-1})
A	Mar 30 - Apr 19	19	52,680,828	0.4
B (B1-B2)	Apr 25 - May 17	12	82,076,869	9
C (C1-C2)	May 18 - Jun 05	8	27,776,622	9.5
D (D1-D6)	Jun 24 - Jul 19	21	166,041,737	320
E (E1-E7)	Jul 29 - Aug 18	22	134,651,378	1118
F (F1-F2)	Aug 19 - Aug 30	10	76,047,580	1980
G (G1-G6)	Sep 22 - Oct 07	18	110,117,334	9070
H (H1-H2)	Oct 08 - Oct 18	9	41,045,862	9300
I (I1-I2)	Oct 24 - Oct 29	7	72,903,547	23000

Table 4.1: ATLAS 2010 data taking periods

The whole 2010 amount of data taken by ATLAS was used in order to search for high-mass resonances, such as heavy neutral gauge bosons Z', decaying to two muons. The present chapter presents the results of this analysis. The methods are described in detail and, since no Z' signal was observed, the limits on the cross section times branching ratio ($\sigma \times B$) are set for the new boson.

Throughout the rest of the chapter, Reference [51] is widely used.

4.2 Skimming and slimming of the data samples

Due to the large (and continuously growing) amount of data, the basic format of the analysis objects (AODs) have to undergo a specific proccess, in order for their volume to be reduced.

This processing would remove entire events ("skimming"), remove entire data containers (i.e., specific variables) within an event ("slimming") and remove parts of data container ("thinning") that were not needed for a particular analysis. The resulting object (DPD) will be smaller, so that more events can be stored locally and be much faster to analyze[3].

For the scopes of our analysis, the preselection of the data samples that we have used required the presence of at least one combined MuID muon, with $P_T > 25\,\mathrm{GeV}$ and for the events to have pre-passed the trigger requirement.

4.3 Signal and Monte Carlo Samples

The Monte Carlo samples that are used in this analysis (both Z' signal and background ones) are generated and simulated within the ATHENA MC10 framework [52].

4.3.1 Z' Signal

For the signal, we have used the Sequential Standard Model (SSM), already described in an earlier section, in which a heavy gauge boson (Z') is considered identical to the Z boson, i.e. it has the same couplings to fermions.

The samples were generated with Pythia [53], using MRST2007lomod[4] PDFs [54], with the Z' interference with γ and Z boson switched on. For the present analysis, we

---

[3] http://atlas-service-enews.web.cern.ch/atlas-service-enews/2007-8/features_07-8/features_data.php

[4] also known as LO*

have generated the $Z' \to \mu^+\mu^-$ procedure for eight different Z' masses, raising from 250 GeV to 2 TeV.

The details for those signal samples are shown in Table 4.2. The cross-sections are given on Leading Order level, since the higher-order corrections estimation is described later in the text, in a dedicated paragraph (4.6).

Pole Mass (GeV)	Mass Threshold (GeV)	σB[pb] (LO)
250	125	36.136
500	250	2.664
750	375	0.488
1000	500	0.129
1250	625	0.042
1500	750	0.015
1750	875	0.006
2000	1000	0.003

Table 4.2: The $Z' \to \mu\mu$ signal samples, used in the analysis

4.3.2 Backgrounds

The final state of the Z' decay we are working on is characterised by the presence of two, oppositely charged, muons. Therefore, any procedure with the same signature can be a background process in our study.

The dominant and irreducible background is due to the $Z/\gamma^* \rightarrow \mu\mu$ (Drell-Yan) process to muons. For this background, in order to increase the statistics, many binned samples were produced, for the large masses. A $Z/\gamma^* \rightarrow \mu^+\mu^-$ inclusive sample of 5 million events is used up to 250 GeV, then the high-mass binned samples are added.

Next is the $t\bar{t} \rightarrow \mu^+\mu^-$ process (with the top quark mass set to 172.5 GeV), generated with a 2 muon with $P_T > 15\,\text{GeV}$ filter, and the Diboson production (WW, WZ, ZZ) (one muon filter). Other, less important, backgrounds include the production of a W (decaying to a muon: $W \rightarrow \mu\nu$) accompanied by jets, with $P_T > 20\,\text{GeV}$ filter (6 generated samples, according to the number of partons: 0-5), when one jet is misidentified as a muon and, finally, the QCD procedures $b\bar{b} \rightarrow \mu^+\mu^-$ and $c\bar{c} \rightarrow \mu^+\mu^-$ (originally generated with a one muon with $P_T > 15\,\text{GeV}$ filter, then skimmed by Athens group to have an additional muon).

The cosmic rays can also be a potential background source (an analytical study on the cosmic background has been performed and will be presented in section 4.9).

For the production of the background samples, PYTHIA was used for the Z samples. For the $t\bar{t}$, the samples are generated with MC@NLO [55] to generate matrix elements, JIMMY [56] to describe multiple parton interactions and HERWIG [57] to describe the remaining underlying event and parton showers. CTEQ6.6 [58] parton distribution functions are used for the $t\bar{t}$ sample. The W + jets background is generated with ALPGEN to generate matrix elements, JIMMY to describe multiple parton interactions and HERWIG to describe the remaining underlying event and parton showers. CTEQ6L1 [58] PDFs are used. Finally, the QCD background is simulated using PYTHIA hard-QCD processes, i.e. quark-quark, quark-gluon and gluon-gluon scatters.

In our analysis, all the above mentioned backgrounds are estimated from the Monte Carlo simulation, apart from $b\bar{b}$ and $c\bar{c}$, for which, due to the large uncertainty on their cross-section, a data-driven estimation should be performed.

Several details for the Monte Carlo background samples used in our analysis can be seen in Table 4.3. The “generated” cross-section is given by the generator (e.g., Pythia), while the “calculated” ones have the higher order corrections incorporated (apart from the Drell-Yan sample, for which a more dedicated study has been performed -section 4.6).

4.4 Pile-Up Reweighting

Our Monte Carlo background samples incorporate in-time and out-of-time pile-up effects[5], in order to simulate the pile-up conditions that are most representative of the real data. In Figure 4.1[6], a real event with four (pile-up) vertices can be seen.

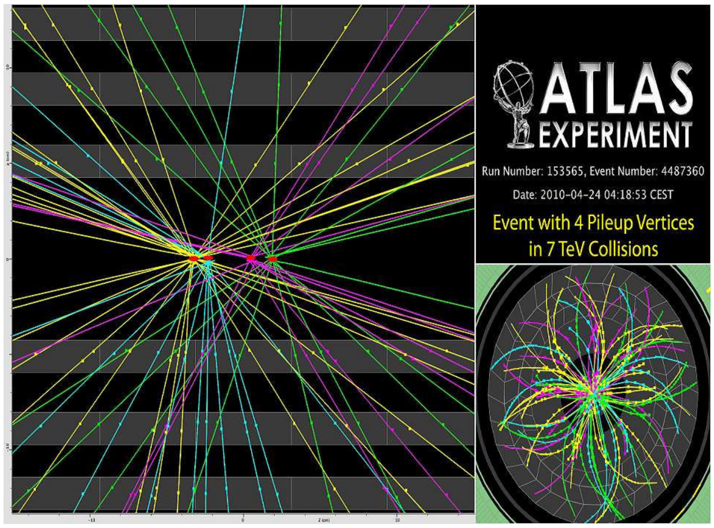

Figure 4.1: An event with four reconstructed primary vertices, consistent with an event with four primary proton-proton collisions in the same beam-crossing

A way to “adjust” our background samples to the real pile-up conditions is to compare them to the data, in terms of the number of the reconstructed vertices -as a measure of how much pile-up there was in a given event.

The ATLAS exotics group has performed a study [51] on the compatibility of the

---

[5] in high-luminosity colliders, there is a non-negligible probability that one single bunch crossing may produce several separate events

[6] https://twiki.cern.ch/twiki/bin/view/AtlasPublic/EventDisplayPublicResults

Process	σB[pb] (gen.)	σB[pb] (calc.) (NNLO)	Equiv.Luminosity (fb^{-1})
Z$\rightarrow \mu\mu$ ($60 < M_{gen} < 250$)	856	(see Section: 4.6)	5.84E+00
$Z(250, 400) \rightarrow \mu\mu$	0.416		4.81E+01
$Z(400, 600) \rightarrow \mu\mu$	0.0672		2.98E+02
$Z(600, 800) \rightarrow \mu\mu$	0.0112		1.43E+03
$Z(800, 1000) \rightarrow \mu\mu$	0.00274		7.30E+03
$Z(1000, 1250) \rightarrow \mu\mu$	0.000918		2.18E+04
$Z(1250, 1500) \rightarrow \mu\mu$	0.000249		8.03E+04
$Z(1500, 1750) \rightarrow \mu\mu$	0.000077		2.60E+05
$Z(1750, 2000) \rightarrow \mu\mu$	0.000026		7.69E+05
$Z(> 2000) \rightarrow \mu\mu$	0.000015		1.33E+06
$t\bar{t} \rightarrow \mu^+\mu^-$	80.2	89.4	1.12E+01
WW (one lepton filter)	29.59	17.46 (NLO)	1.42E+01
WZ (one lepton filter)	11.23	5.543 (NLO)	1.26E+01
ZZ (one lepton filter)	4.59	1.261 (NLO)	1.98E+02
W$\rightarrow \mu\nu$ (W+ 1 jet)	1304.2	1561.6	4.10E-01
W$\rightarrow \mu\nu$ (W+ 2 jets)	377.8	453.5	4.14E-01
W$\rightarrow \mu\nu$ (W+ 3 jets)	101.9	121.7	4.19E-01
W$\rightarrow \mu\nu$ (W+ 4 jets)	25.8	31.0	4.19E-01
W$\rightarrow \mu\nu$ (W+ 5 jets)	6.9	8.3	4.22E-01
$b\bar{b} \rightarrow \mu\mu$	28400	see Section: 4.8	1.41E-01
$c\bar{c} \rightarrow \mu\mu$	73900	see Section: 4.8	1.35E-02

Table 4.3: The Monte Carlo samples used in the $Z' \rightarrow \mu\mu$ analysis

number of vertices of the Monte Carlo and the whole real data set[7], using the $Z \rightarrow \mu\mu$ sample. Based on this study, we apply a weight on each event of all the Monte Carlo samples, which corresponds to the ratio of the data and Monte Carlo primary vertices.

The vertex distribution for the data and the $Z \rightarrow \mu\mu$, before and after pile-up reweighting, is presented in Figure 4.2. The applied weights can be seen in Table 4.4.

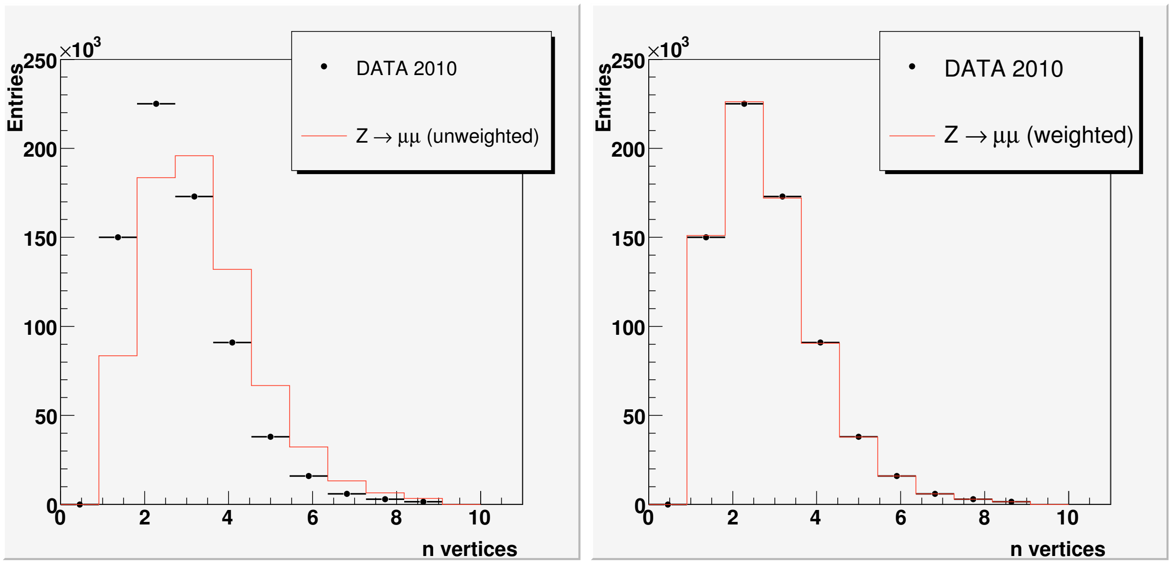

(a) (b)

Figure 4.2: The vertex distribution for the data and the $Z \rightarrow \mu\mu$, before (left) and after (right) pile-up reweighting

$N_{vertices}$	1	2	3	4	5	6	7	8	9
Weight	1.7955	1.2259	0.8834	0.6890	0.5686	0.4945	0.4511	0.4583	0.4513

Table 4.4: Event weights for the Monte Carlo samples

---

[7] the comparison was made using data events passing the good run list and the trigger requirement

An example of the effect of the pile-up reweighting for the Drell-Yan and theZ' sample of 1TeV can be seen in Figure 4.3, where the ratio of the invariant mass, before and after the weighting of the events, has been plotted.

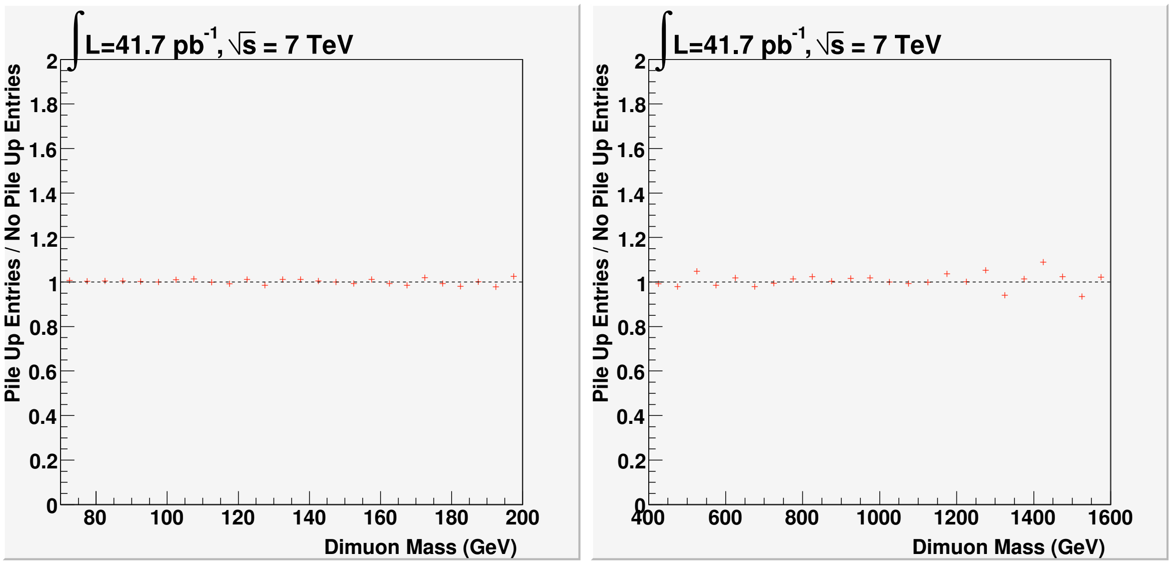

(a) (b)

Figure 4.3: Ratio of the mass distributions of Drell-Yan (left) and 1 TeV Z' (right), before and after the pile-up reweighting

4.5 Analysis Selection Criteria

Not the whole amount of data taken by ATLAS is appropriate to be analysed. In order for an event to be taken into account in the analysis, certain quality criteria should be fulfilled. Those, in general, ensure on one hand the quality of the events that apply for analysis and, on a second level, that a Z' boson oriented analysis is applied.

The selection criteria can be divided, therefore, in two parts: the selection criteria applied on the events and those applied afterwards to the muons within the event.

4.5.1 Event Selection Criteria

4.5.1.1 GRL selection

To define a good dataset we need Data Quality (DQ) information, as assessed by the DQ group. This is done by producing dedicated lists of runs and luminosity blocks for every Period, known as “Good Run Lists” (GRLs). The GRLs are special scripts, produced for every data run, that select those Luminosity Blocks that are appropriate for physics analysis.

A Good Run List is formed by applying the appropriate DQ criteria to the whole list of all physics runs and Luminosity Blocks and test which parts of data pass them. What characterizes those criteria are the “Data Quality status” flags [60]. Each subdetector (e.g, the Muon Spectrometer) or system (e.g., the Trigger) has its own flags and it’s responsible for filling them. The filing of each flag is performed in every Luminosity Block. Those flags vary from detector conditions (for example, the voltages and temperatures, usually automatically filled) up to more complex issues that have to do with hardware and data-taking.

In Table 4.5, we present the collection of all the Data quality flags that are used for the $Z' \rightarrow \mu\mu$ analysis.

4.5.1.2 Trigger Selection

In order for an event (that has already passed the Good Run List criteria) to further proceed for analysis, at least one of the candidate muons has to pass the muon trigger with the lowest available threshold momentum.

This trigger is not common for all runs but it changes with time, to adjust to the continuously increasing luminosity, during the several data periods.

The triggers used for every period/run are presented in Table 4.6, along with the corresponding luminosity.

4.5.1.3 Primary Vertex Selection

In order to ensure that the event we are testing is, indeed, a result of a proton-proton collision, we request the existence of at least one reconstructed primary vertex with at

Flag Type	Flag Name
General	ATLGL,ATLSOL,ATLTOR,LUMI
Muon Detector	MDTBA ,MDTBC, MDTEA, MDTEC, CSCEA, CSCEC, RPCBA, RPCBC, TGCEA, TGCEC
InnerDetector	PIX0, PIXB, PIXEA, PIXEC, SCTB, SCTEA, SCTEC, TRTB, TRTEA, TRTEC, IDGL, IDAL
Trigger	L1MUE, L1MUB, TRMUO
Muon Reconstruction	MSTACO, MMUIDCB

Table 4.5: Data quality flags used for the $Z' \rightarrow \mu\mu$ analysis

Period / Run	Trigger	Luminosity (pb^{-1})
A - E3 (152166 - 160879)	L1_mu10	0.78
E4 - G4 (160899 - 165818)	EF_mu10 ||EF_mu10_MG	6.02
G5 - I1 (165821 - 167576)	EF_mu13 ||EF_mu13_MG	15.80
I1 - I2 (167607-167844)	EF_mu13_tight||EF_mu13_MG_tight	19.08

Table 4.6: The triggers used for every Run Period for $Z' \rightarrow \mu\mu$ analysis

least three associated tracks.

4.5.2 Muon Selection Criteria

After the good events are chosen, additional criteria have to be applied on the muons of the event, which should be appropriate for a Z' boson oriented analysis. In addition to that, the good reconstruction of the muons should be ensured, since a small P_T, reconstructed as a large one, will "transfer" background events in the signal region, while the opposite procedure (reconstruction of a large P_T as a small one) would make us lose signal events ("transfer" to the background region).

The cuts described below should be passed by at least two muons, in order for each event to further proceed for analysis.

4.5.2.1 Muon Reconstruction Algorithm

For the present analysis, among the two muon reconstruction algorithms that are used in this initial part of ATLAS data taking, MUID was chosen.

Both algorithms presented similar performances for resolution and efficiency (at least in the P_T region below 100 GeV, since the statistics did not allow for a higher region study). However, a problem in the MDT hits variables of STACO (which are used in the analysis, as it will be described in Section 4.5.2.6) was the reason that MUID was favored.

4.5.2.2 2 Combined Muons

Since the most important aspect of this type of analysis are the two produced muons, we only allow events which are characterized by the presence of at least two muons, with the extra requirement that these muons are also combined (i.e., reconstructed by both the Muon Spectrometer and the Inner Detector). This choice gives us the maximum amount of information possible.

4.5.2.3 Pseudorapidity

The muons of the event are restricted to have a pseudorapidity value within the geometrical acceptance of the Muon Trigger System, namely $|\eta| < 2.4$. The latter should apply for both muons that pass the previous cut.

4.5.2.4 Transverse Momentum

A cut in the transverse momentum value is necessary, in order to reject all the low energy -and of no particular interest- physics. Hence, a $P_T > 25\,\text{GeV}$ cut is applied for the two muons under study.

4.5.2.5 Inner Detector Hits

Combined (as well as tagged) muons have associated inner detector tracks. Some cuts on the associated inner detector tracks have to be applied, in order to ensure the quality of the latter.

The cuts are constructed in such a way that the detector conditions are taken into account for the silicon systems. For example, if a passed module is dead, it is added to the hit count, ignored in the hole count and (in some special cases) the B-layer expectation canceled.

- B-layer cut: We require a pixel B-layer (the innermost layer of the Pixel detector) hit on the muon, except from the case where the extrapolated muon track passed an uninstrumented or dead area of the B-layer (in this case we cancel this expectation)
- Pixel hits + Pixel Dead Sensors >= 2
- SCT Hits + SCT Dead Sensors >= 6
- Pixel Holes + SCT Holes <= 1
- TRT hits: A successful extension into the TRT. Namely, we require a minimum number of TRT hits and a maximum one for the outliers (e.g., those hits that are close to a track, but not associated to it).

$|\eta| < 1.9$: Hits+Outliers >= 5 and $\frac{\text{Outliers}}{\text{Hits+Outliers}} < 0.9$
$|\eta| >= 1.9$: If Hits+Outliers >= 5, then $\frac{\text{Outliers}}{\text{Hits+Outliers}} < 0.9$

This cut is important to reject fake tracks.

4.5.2.6 Muon Spectrometer Hits

After the restrictions on the track that constructs the combined muons, we should also impose some quality cuts on the Muon Spectrometer hits, so as to ensure the good reconstruction of the muon.

- At least three hits in all of Barrel or Endcap Inner, Middle and Outer MDT/CSC precision layers.
- At least one phi hit (in CSC/RPC/TGC chambers)
- We also veto BEE, EE and BIS78, due to alignment reasons.

The 3-station measurement is giving the best muon resolution estimation (compared to the cases where muons have track segments in two layers only -for a relative study, see Appendix B). So, under this selection, we avoid sources of badly reconstructed high P_T events.

4.5.2.7 Impact Parameter Cuts

In our analysis, special care is taken in order to reject the muons coming from cosmic rays.

Those muons, since they are not originating from the interaction point, will have, in the majority of the cases, a large set of impact parameters (z_0, d_0), compared to the muons that come from collisions.

Therefore we remove muons that appear, in general, quite displaced with respect to the primary vertex:

$$z_0 < 1\,\text{mm} \tag{4.1}$$

$$d_0 < 0.2\,\text{mm} \tag{4.2}$$

In the vast majority of the cases, a muon fails to satisfy both Impact Parameter cuts at the same time: a clear indication that we are dealing with a cosmic event.

In Figure 4.4, the distribution of the z_0 and d_0 variables is presented, for muons passing all cuts except the Impact Parameters cut, for the data and all the background samples. All samples are normalized to unity.

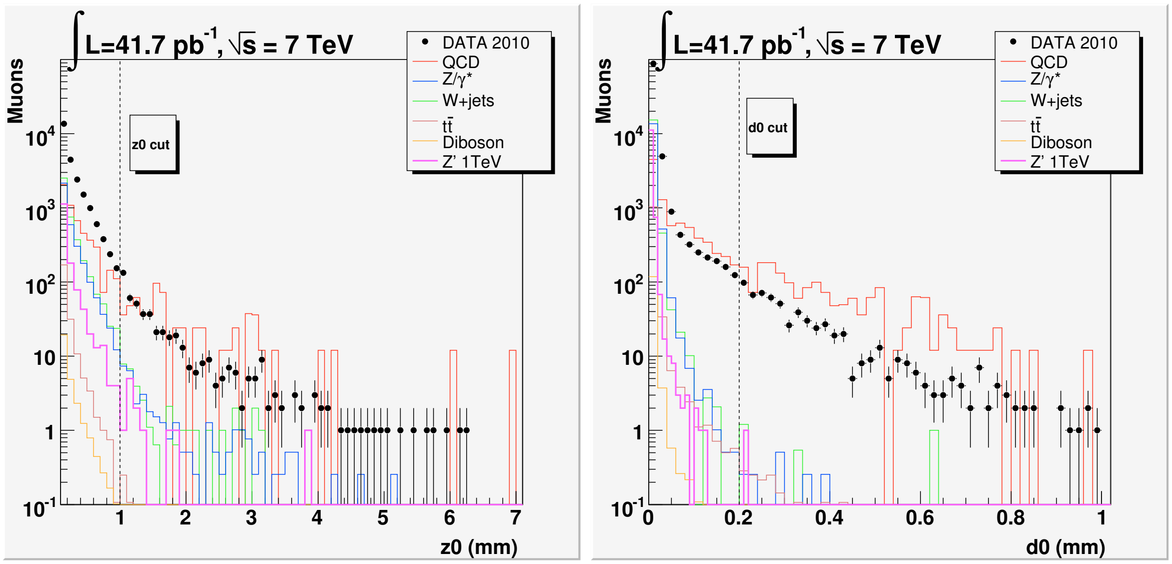

(a) (b)

Figure 4.4: The z_0 (left) and d_0 (right) distributions (all samples normalized to unity)

Further study of the Impact Parameter cut and a demonstration that it does indeed reject muons from cosmic rays is presented in section 4.9.

4.5.2.8 Isolation

A very important characteristic of the muons coming from the Z' boson decay is the fact that they are going to appear isolated. Therefore, we request, for both muons in the event, to have no additional activity in the surrounding area.

The above condition is fulfilled by asking the sum over all the tracks' P_T (with the P_T of the muon itself not being taken into account), in a $\eta - \phi$ cone around the muon equal to 0.3, to be less than a small percentage of the P_T of the muon:

$$\frac{\sum_{dR<0.3} P_{T,tracks}}{P_{T,muon}} < 5\% \tag{4.3}$$

The distribution of the ratio of Equation 4.3 is presented in Figure 4.5, for data and background[8], for muons passing all other cuts, except the Isolation one. All samples are normalized to unity.

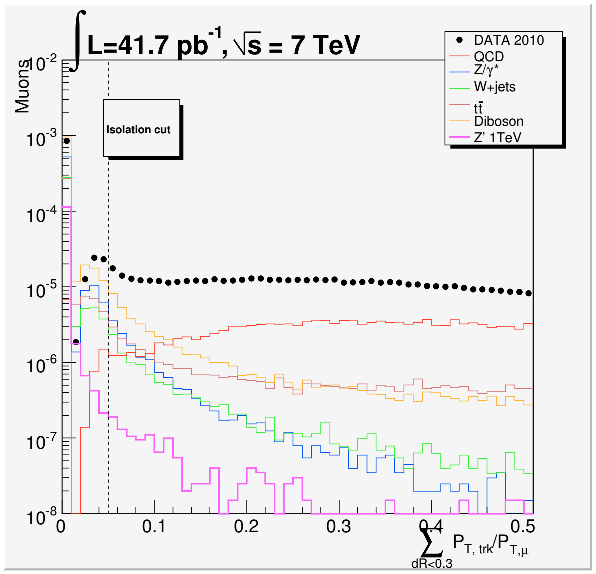

Figure 4.5: The Isolation variable distribution (all samples normalized to unity)

The isolation cut has been optimized, after trying several cone values and P_T thresholds. The combination of $\frac{\sum_{dR<0.3} P_{T,tracks}}{P_{T,muon}} < 5\%$ was selected among others, since it enhances the QCD rejection, while keeping the largest part of the signal. In addition, the relatively small cone of 0.3, ensures that we avoid large pile-up contributions to the sum of the tracks' P_T.

---

[8] the peak in the low region of the QCD distribution is due to the fact that the $P_{T,tracks}$ variable is counted taking into account only tracks with $P_T > 1\,\text{GeV}$

4.5.3 Cuts on the muon pair: Opposite Charge and Invariant Mass

After applying all the above selection criteria, we have to test if the pair of muons that made it to the final step of the selection form a good Z' boson candidate.

At this particular point, we test whether the two muons possess opposite electric charges. If so, we form their Invariant Mass and require for the latter to be greater than 70GeV, in order for the event to be processed in the mass plot[9].

In the case that we result with more than two good muons in the final stage of the analysis, we search for the two most energetic ones and do the same as above (in general, one every 300 data events possess more than two muons that pass all the steps of our selection).

All the selection cuts that are applied in this analysis are summarized in Tables 4.7 (Event Selection) and 4.8 (Muon Selection).

Event Selection Cut	Description
GRL	LumiBlocks with Detector in full operation
Trigger	Trigger P_T increases with RunNumber / Luminosity
Primary Vertex	>= 1 reconstructed P.V. with >= 3 associated tracks

Table 4.7: Selection Cuts for Z' analysis - Event Selection

In Table 4.9 we present the cut flow for the data samples, while Table 4.10 is the corresponding table for the background procedures (for reasons of compatibility, the skimming of the data has been applied to the background samples, as well). Finally,

---

[9] in a dedicated study of the ATLAS exotics group, it was estimated that only one out of 15,000 muons is misreconstructed, in terms of their electric charge

Muon Selection Cut	Description
Reconstruction Algorithm used	MUID
Combined muons	>= 2 Combined muons
Pseudorapidity	$\|\eta\| < 2.4$
Transverse Momentum	$P_T > 25\,\text{GeV}$
Inner Detector Hits	>= 1 B-layer hit (unless a dead area passed) Pixel Hits + Pixel Dead Sensors >= 2 SCT Hits + SCT Dead Sensors >= 6 Pixel Holes + SCT Holes <= 1 TRT: $\|\eta\| < 1.9$: (Hits+Outl. > 5),$\frac{Outl.}{Hits+Outl.} < 0.9$ $\|\eta\| >= 1.9$: If (Hits+Outl. > 5), then $\frac{Outl.}{Hits+Outl.} < 0.9$
Muon Spectrometer Hits	>= 3 hits in all of Barrel or Endcap Inner, Middle and Outer MDT/CSC precision layers >= 1 ϕ hit no BEE, EE or BIS78 hits
Impact Parameter Cuts	$z_0 < 1\,\text{mm}$, $d_0 < 0.2\,\text{mm}$
Isolation	$\frac{\sum_{dR<0.3} P_{T,tracks}}{P_{T,muon}} < 5\%$
Charge	Two muons with opposite charge
Invariant Mass	$\text{Mass}_{\mu^+\mu^-} > 70\,\text{GeV}$

Table 4.8: Selection Cuts for Z' analysis: Muon Selection

Table 4.11 presents the cut flow for three Z' samples.

4.5.4 Further examining of the Selection Cuts

We studied the more dedicated cuts that have been applied (i.e., Inner Detector hits, Muon Spectrometer hits, Impact Parameters and Isolation), in terms of their affect on the data events.

For the whole amount of the 2010 data and for the four cuts mentioned above, we plot the dimuon mass distribution for the events that undergo every cut requirement, except a particular one (at a time). Then we reapply the whole set of cuts, to see how many and what type of events this particular cut rejected.

The result of the above process can be seen in Figures 4.6 and 4.7. In general, it can be seen from these plots that there seems to be no bias concerning the invariant mass of the events rejected by each of the cuts.

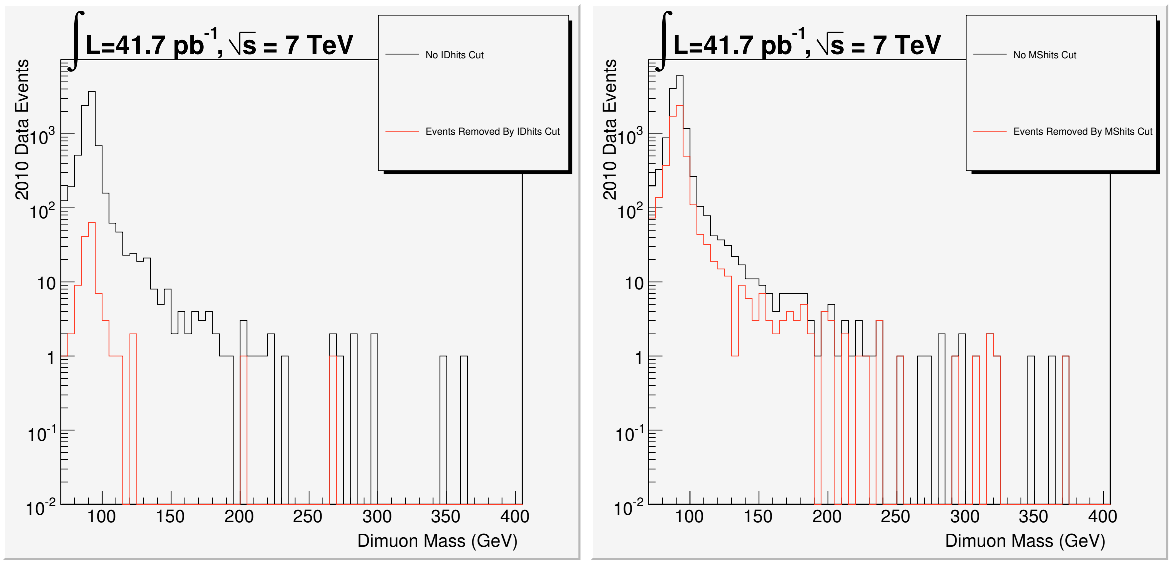

(a) (b)

Figure 4.6: The events removed by IDhits cut (left) and MShits cut (right)

It has been estimated that, in the Inner Detector hits case, a percentage of 1.6% of the events failed the cut, while for the Impact Parameter, the Isolation and the Opposite

Selection Cut	Absolute Efficiency (%)	Relative Efficiency (%)
Trigger	100	100
Primary Vertex	99.83	99.83
2 CB muons	12.38	12.40
$\eta < 2.4$	11.80	95.35
$P_T > 25\,\mathrm{GeV}$	3.13	26.52
ID hits	3.03	96.95
MS hits	1.77	58.43
Impact Parameters	1.72	97.53
Isolation	1.56	90.38
Opposite Charge	1.56	99.99

Table 4.9: Cut Flow for the 2010 Data samples (after skimming: one muon with $P_T > 25\,\mathrm{GeV}$ plus trigger)

Cut	Z/γ^*(%)	$t\bar{t}$(%)	Dibosons(%)	W+jets(%)	$b\bar{b}$(%)	$c\bar{c}$(%)
Trigger	100	100	100	100	100	100
PV	99.68	99.77	99.79	99.82	99.39	99.48
2CB	71.03	98.71	20.02	3.72	95.48	96.47
η	66.54	97.06	18.98	3.49	93.61	94.77
P_T	54.5	24.13	9.75	0.14	3.2	2.98
ID hits	53.05	23.12	9.47	0.13	2.93	2.55
MS hits	31.72	13.55	5.71	0.04	1.64	1.4
IP	31.61	12.1	5.68	0.03	0.9	1.01
Isolation	29.9	7.17	5.22	0.01	0	0
Op. Charge	29.9	7.12	5.05	0.01	0	0

Table 4.10: Cut Flow for the background samples (after skimming: one muon with $P_T > 25\,\mathrm{GeV}$ plus trigger). $t\bar{t}$(%) is produced with a two muon filter and Diboson samples with one lepton filter

Cut	Z' 750 GeV	Z' 1000 GeV	Z' 1250 GeV
Trigger	93.92	94.01	93.84
PV	93.65	93.76	93.60
2CB	76.67	77.20	76.75
η	74.34	75.48	75.29
P_T	73.60	74.71	74.70
ID hits	71.22	72.17	72.27
MS hits	41.58	41.64	41.71
IP	41.48	41.57	41.67
Isolation	40.38	40.42	40.68
Op. Charge	40.38	40.42	40.66

Table 4.11: Cut Flow for the Z' samples

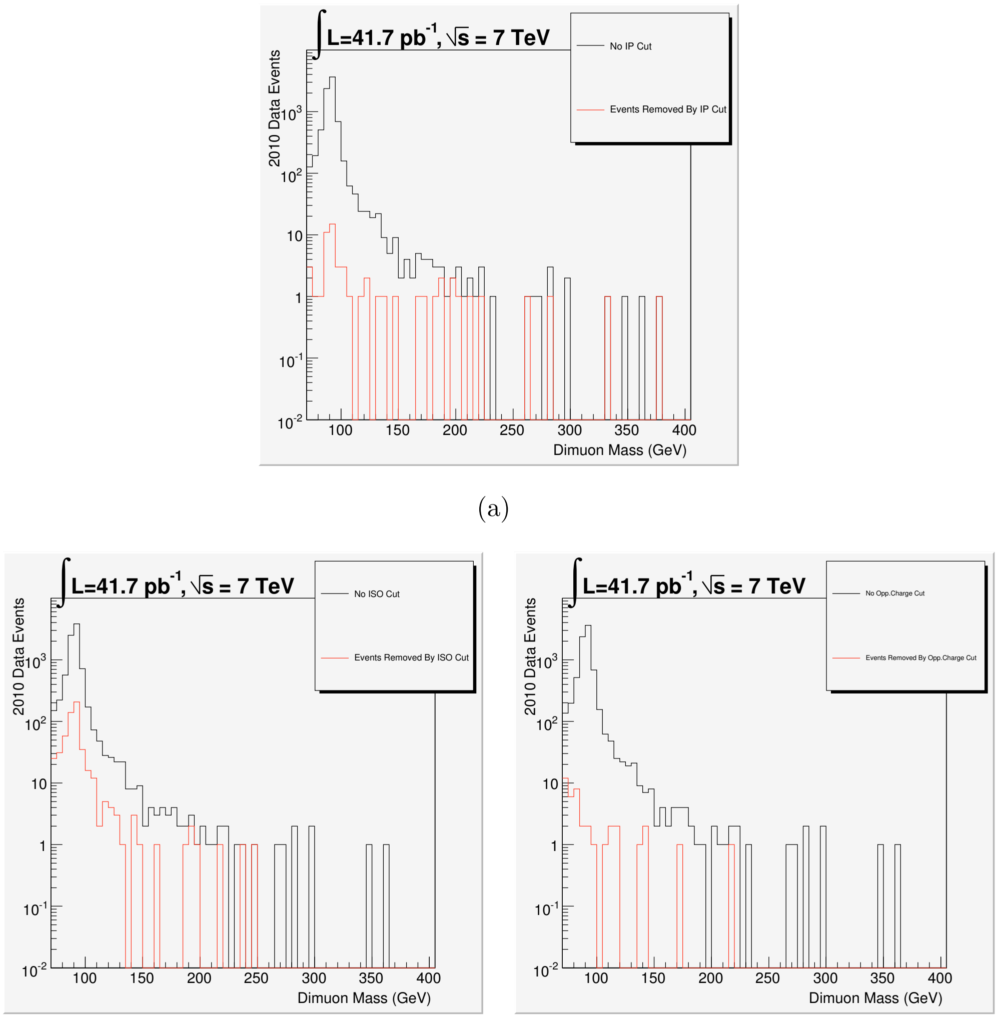

(a)

(b)

(c)

Figure 4.7: The events removed by the IP cut (a), Isolation cut (b) and opposite charge cut (c)

Charge cuts the percentage was 0.8% and 9.8% and 10% correspondingly. The Muon Spectrometer hits cut was the stricter one, since it rejects a 41% of the data events.

4.6 Cross Sections' Higher Order corrections

All our Monte Carlo samples were typically generated using the Leading Order (LO) cross sections and the corresponding Parton Distribution Functions (PDFs)[10]. However, higher-order QCD (Next to Leading Order -NLO- and Next to Next to Leading Order -NNLO) corrections and also Electroweak (E/W) ones should be taken into account, which will affect the generated LO cross sections. The methods used to estimate those corrections, for both cases, are described in the following.

4.6.1 QCD corrections

To estimate the NLO/NNLO corrections, we use the PHORZ program [61] with various PDF sets.

The PDFs represent analytical fits obtained using a combination of theory and experimental data. One possible parameterization of the PDFs, MSTW2008, is shown in Figure 4.8 [62].

What we want to do is to extract a k-factor, which will then be used to multiply the LO differential cross section to yield the NNLO one: $k_{NNLO} = \frac{\sigma_{NNLO}}{\sigma_{LO}}$. In the Drell-Yan case, the k-factor is not a fixed number, but, instead, a mass dependent function: $k_{NNLO} = f\left(M_{\mu^+\mu^-}\right)$.

For convenience, we assume that all colorless final states are characterized by the same QCD radiation in their initial state. This allows us to use the same k-factor for both the Drell-Yan background and the Z' signal.

The Standard Model group has performed extensive studies of the Drell Yan cross section and associated uncertainties [63]. The general procedure is as follows: choice of a kinematic region, which is valid in the approximations of the NNLO calculation and the Monte Carlo generator and, then, normalization of the MC to NNLO in this region. Some of the parameters used for this particular study are presented in Table 4.12.

---

[10] probability to find a parton, within the proton, with a momentum fraction x: $f(x, Q^2)$

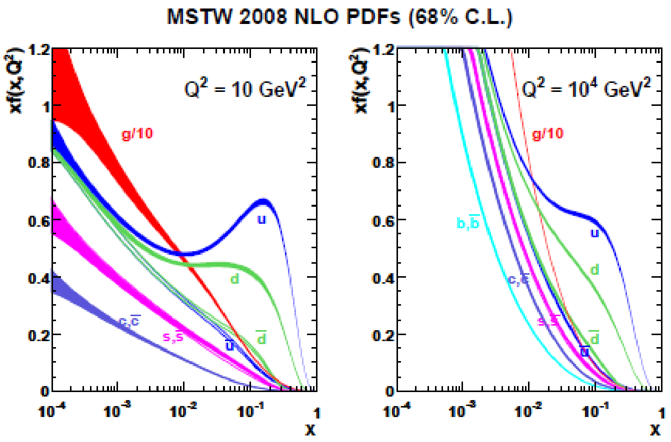

Figure 4.8: The MSTW 2008 NLO PDFs at $Q^2 = 10GeV^2$ (left) and $Q^2 = 10^4 GeV^2$ (right)

Parameter	Symbol	Value
Z width	Γ_Z	2.4958 GeV
Fermi constant	G_F	$1.16637 \times 10^{-5} GeV^{-2}$
Electromagnetic coupling	α_{em}	1 / 132.34
Electroweak mixing	$sin2\theta_W$	0.22255

Table 4.12: Common parameters used in the NNLO k-factor estimation

The differential production cross section $M_{\ell\ell}^2 \frac{d_{\sigma NNLO}}{dM_{\ell\ell}^2}$ was calculated at NNLO using the MSTW2008NNLO PDF for dilepton masses $10\,\mathrm{GeV} < M_{\ell\ell} < 3\,\mathrm{TeV}$ and so was the mass dependent k-factor:

$$K^*_{NNLO}(M_{\ell\ell}) = \frac{d_{\sigma NNLO}}{dM_{\ell\ell}^2}(\mathrm{MSTW2008NNLO})/\frac{d_{\sigma LO}}{dM_{\ell\ell}^2}(\,\mathrm{MRST2007LO}^*) \qquad (4.4)$$

$K^*_{NNLO}(M_{\ell\ell})$ is based on a LO prediction using the MRST2007* [54] modified LO PDF set[11] and shows a modest dependence on $M_{\ell\ell}$ over a wide range of the dilepton masses.

In Table 4.13, we present several indicative values of the k-factor, for the Drell-Yan procedure and for three Z' masses used in this analysis. The resulting mass dependent function is schematically presented in Figure 4.9.

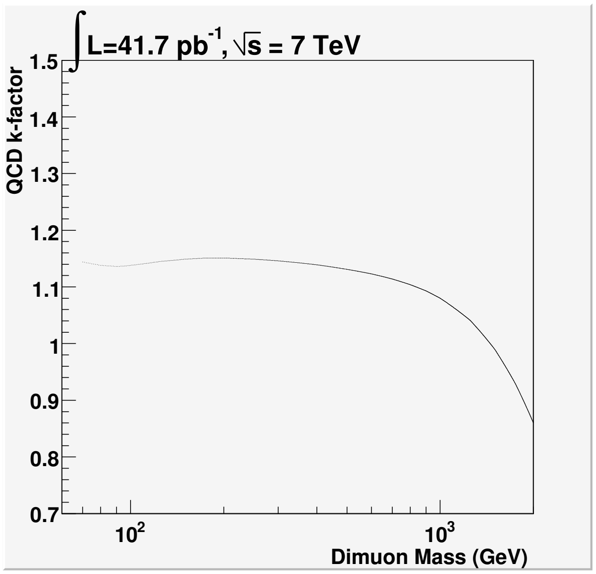

Figure 4.9: Cross section ratio (QCD k-factor) for Drell-Yan pair and Z' production, as a function of the dimuon mass

---

[11] the MRST2007LO* PDF is used in the Monte Carlo production

Drell-Yan Mass (GeV)	QCD k-factor	Z' mass (GeV)	QCD k-factor
70	1.144		
80	1.138		
91.2	1.136		
100	1.138		
200	1.151	250	1.149
400	1.139		
500	1.131		
700	1.114	750	1.109
1000	1.080	1000	1.080
1250	1.041	1250	1.041
1500	0.990	1750	0.929
2000	0.860	2000	0.860

Table 4.13: NNLO Drell-Yan lepton pair and Z' production k-factors, as a function of the dimuon mass

4.6.2 Electroweak (E/W) corrections

Apart from the QCD corrections, the electroweak ones should also be taken into account. For these, we use the HORACE program ([64],[65]).

The electroweak corrections are a sum of final state photon radiation, electroweak loop corrections and the contribution of the initial photons (because of proton's structure). The final state photon radiation (real QED correction) is already simulated by the PHOTOS program [66] and incorporated in our Monte Carlo samples. Therefore, we only consider the remaining two corrections and extract an electroweak k-factor. This is also a mass dependent scale factor, which should be applied, additionally to the QCD one, to the LO cross sections of the sample.

We define cross section weights (i.e., the correction factors) as a function of the dilepton pair invariant mass M, as follows:

1. The ratio of the exact $O(\alpha)$ calculation matched with higher order QED contributions over the prediction including only final state QED radiation in the parton shower approximation (including higher orders): the correction due to electroweak loop contributions

2. The ratio of the prediction including contributions with initial photons over the one excluding these processes (with both calculations using the exact O_α calculation matched with higher order QED contributions): the correction due to the photon contribution of the proton structure

The final correction will be a combination (product) of the above two.

For the differential cross section calculations we have used the MRST2004QED PDF set [67], which provides a photon distribution function based on photon radiation and splitting kernels, and a lepton acceptance of $|\eta_\ell| < 2.5$ and $P_{T,\ell} > 20\,\mathrm{GeV}$. As this acceptance does not properly match the data selection applied, we have recalculated the electroweak K factor for $|\eta_\ell| < 2.4$ and $P_{T,\ell} > 25\,\mathrm{GeV}$. It has been estimated that the two predictions agree on a level of $\sim 0.2\%$.

Of course, due to the second contribution (electroweak loop corrections), the electroweak k-factor can not be applied to the Z' signal, since it depends on the couplings of the latter to the weak bosons, W and Z (i.e, it is not universal, but, instead, model dependent).

The mass dependence of the E/W k-factor for the Drell-Yan sample is presented in Fig 4.10, while in Table 4.14 we give some indicative correction values.

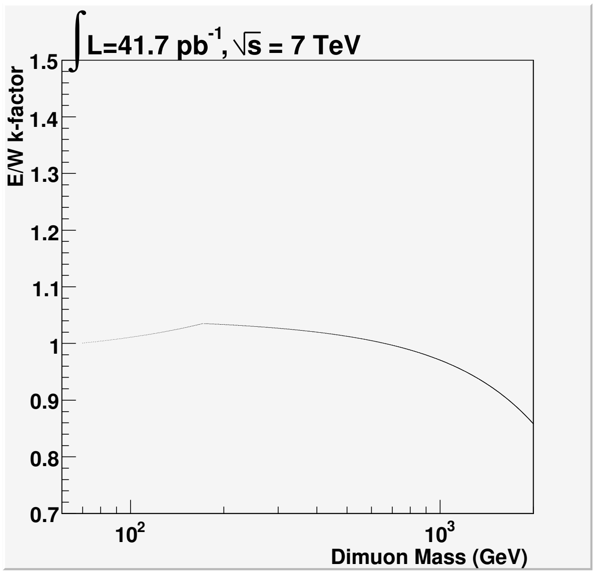

Figure 4.10: Electroweak correction factor (E/W k-factor) for Drell-Yan pair production (only), as a function of the dimuon mass

In Figure 4.11 the dimuon mass of the $Z \to \mu\mu$ sample can be seen, before and after the higger-order corrections of both types, for two different mass ranges. In Figure 4.12, the corrected plot for the Z' signal is presented (in this case, as explained earlier, only the QCD corrections are applied).

4.7 Momentum scale and resolution smearing

The resolution function can be fitted with the sum in quadrature of three terms: the uncertainty on the energy loss corrections P_0, the multiple scattering term P_1 and the intrinsic resolution P_2:

$$\frac{\sigma(P_T)}{P_T} = \frac{P_0}{P_T} \oplus P_1 \oplus P_2 \times P_T \tag{4.5}$$

Drell-Yan Mass (GeV)	EW k-factor
70	1.000
80	1.004
90	1.008
100	1.011
200	1.033
400	1.020
500	1.013
700	0.997
1000	0.971
1250	0.946
1500	0.919
2000	0.858

Table 4.14: Electroweak k-factors for the Drell-Yan pair production, as a function of the dimuon mass

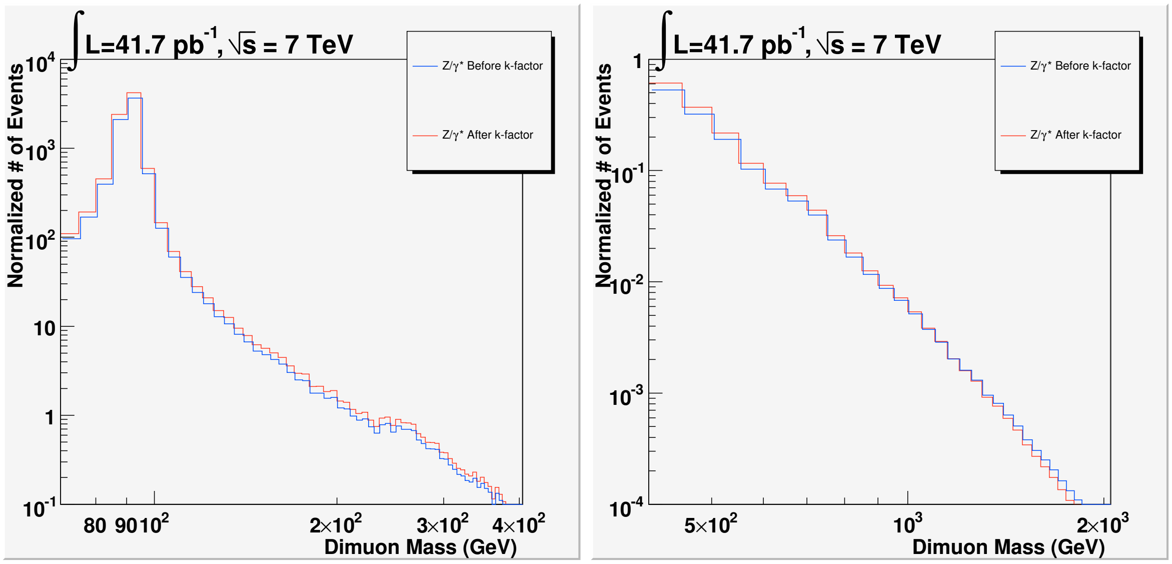

(a) (b)

Figure 4.11: QCD and E/W corrections: Dimuon mass for the Drell-Yan background before (blue) and after (red) applying the k-factors. Left: $70 < M_{\mu\mu} < 400$, Right: $M_{\mu\mu} > 400$

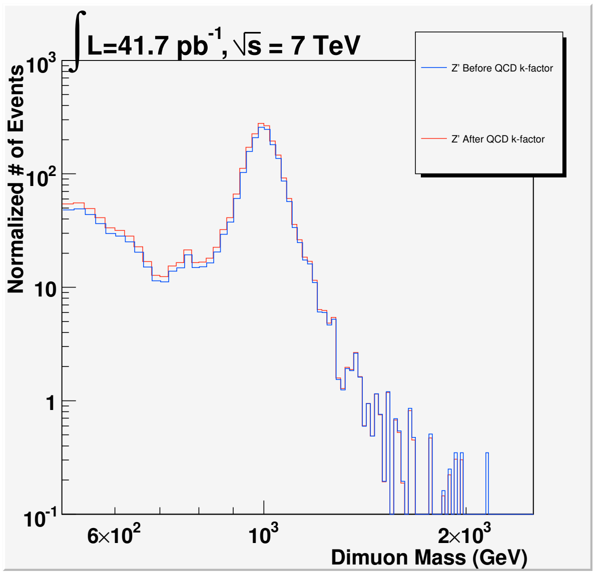

Figure 4.12: QCD corrections: Dimuon mass for the $Z' \rightarrow \mu\mu$ sample of 1 TeV, after the QCD k-factor implementation

At high transverse momentum, the first term can be neglected, as it can be seen from Figure 4.13.

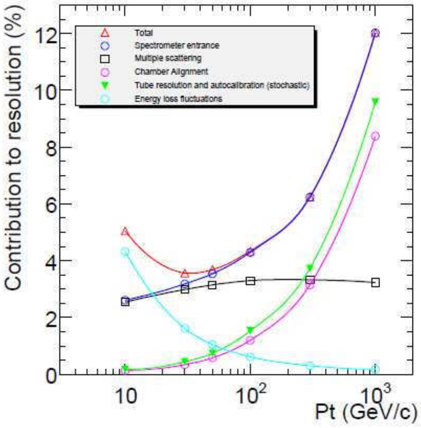

Figure 4.13: Contributions to the muon resolution vs. muon P_T

To adjust the muon momentum resolution in simulations to the data, a gaussian smearing of the Inner Detector and the Muon Spectrometer P_T is performed, such that:

$$\delta\left(\frac{q}{p_T}\right) = S_1 \cdot g_1 \cdot \frac{q}{p_T} + S_2 \cdot g_2 \tag{4.6}$$

In the above equation, g_1 and g_2 are random gaussian variables with mean=0 and r.m.s=1 and S_1, S_2 are the smearing constants. These smearing constants are determined by computing the quadratic differences in the resolution parameters between data and simulations:

$$S_i = P_i^{data} \ominus P_i^{MC} \tag{4.7}$$

Finally, the corrected combined P_T is the weighted average of the smeared P_T's from the Inner Detector and the Muon Spectrometer.

The S_2 constant dominates the resolution in the higher P_T region (since the term $S_1 \cdot g_1 \cdot \frac{q}{p_T}$ falls rapidly with the increase of P_T). Furthermore, since we are working with combined muons, it is the Muon Spectrometer that dominates the measurement of the transverse momentum (see Figure 4.14). Thus, the S_2 parameter of the Spectrometer plays the most important role in the determination of the S_2 of the combined track of the muon.

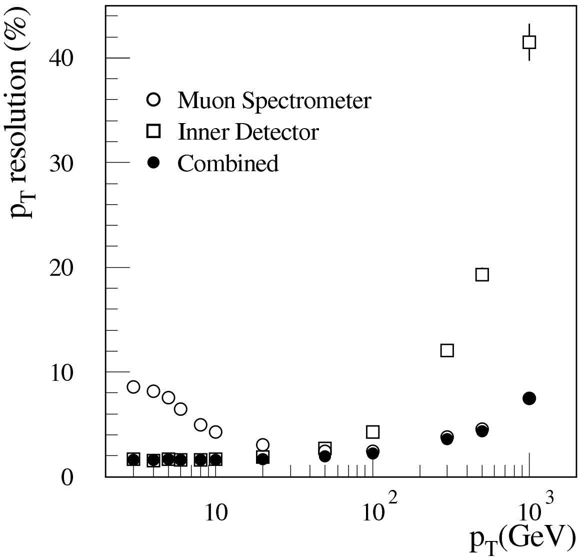

Figure 4.14: P_T resolution contributions on the combined muons

We assume that the ATLAS simulation correctly models the tracker geometry of the Inner Detector and the Muon Spectrometer and any mismatch between the data and the Monte Carlo arises from possible misalignments in the Spectrometer. Therefore, it is the Spectrometer misalignments that mainly determine the S_2 parameter.

In this study, we have used the results of the ATLAS Muon Combined Performance (MCP) group on the subject [70]. After analytic study of the Spectrometer misalignments, the MCP group concluded that by combining the intrinsic curvature resolution and the misalignments we get a factor $\delta\left(\frac{q}{p_T}\right) = (0.2 \pm 0.04)\,\mathrm{TeV}^{-1}$ for the barrel and endcaps and $\delta\left(\frac{q}{p_T}\right) = 0.7 \pm 0.2\,\mathrm{TeV}^{-1}$ for the CSC region (i.e. $|\eta| < 2$). There is also an intrinsic resolution (found from the simulation) of $0.086\,\mathrm{TeV}^{-1}$ in the barrel, $0.096\,\mathrm{TeV}^{-1}$ in the endcaps and $0.12\,\mathrm{TeV}^{-1}$ in the CSC.

To estimate the total smearing parameter S_2, we subtract this small simulation value in quadrature and we finally get:

- Barrel / Endcup: $S_2 = (0.18 \pm 0.04)$ TeV^{-1}

- CSC region: $S_2 = (0.69 \pm 0.2)$ TeV^{-1}

For the S_1 parameter, which plays a role in the low transverse momentum region, we are constrainted from the measured width of the $Z \rightarrow \mu^+\mu^-$ peak. The Monte Carlo is smeared using several different values for the parameter and the one chosen is the one that gives the best with respect to the data.

Again, the study is performed separately in the several regions (barrel, endcups, CSC). The final values are:

- Barrel : $S_1 = 0.00569^{+0.0045}_{-0.00338}$
- Endcups : $S_1 = 0.0199^{+0.00825}_{-0.00262}$
- CSC region : $S_1 = 0.0267^{+0.015}_{-0.009}$

In Figure 4.15, the effect of the P_T smearing is presented on the Drell-Yan background, for the low and the high mass region. The same effect for the Z' sample can be seen in Figure 4.16.

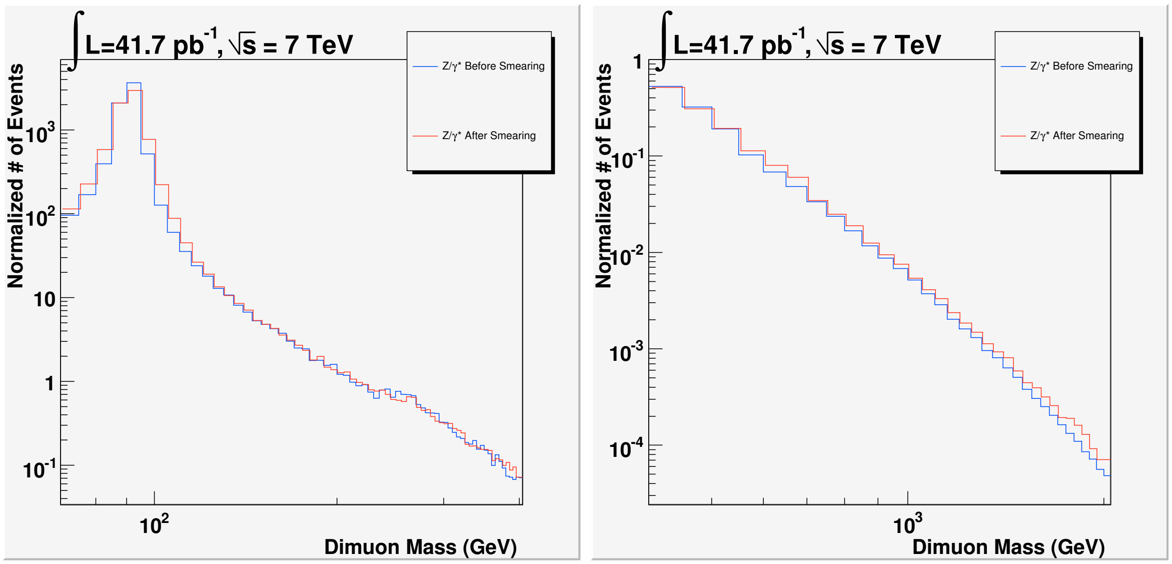

(a) (b)

Figure 4.15: Effect of the P_T smearing on the Drell-Yan background. Left: Low mass region (70 - 400 GeV) Right: High mass region (400 - 2000 GeV)

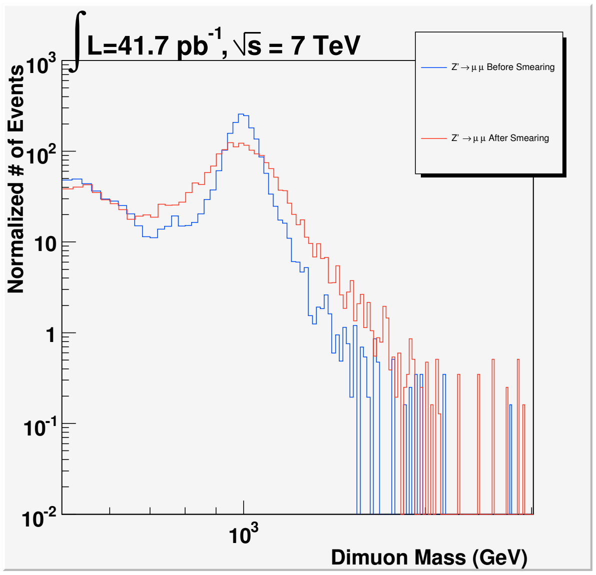

Figure 4.16: The effect of the P_T resolution smearing on the $Z' \to \mu\mu$ sample of 1TeV

4.8 Data driven QCD background estimation

The QCD procedures ($b\bar{b} \to \mu^+\mu^-$, $c\bar{c} \to \mu^+\mu^-$), despite the fact that they do not have an important effect to our analysis, should be treated in a special way, since, due to the large uncertainty on their cross section, the estimation of their contribution should be based on the data ("data driven").

The idea is to compare the Monte Carlo samples of the QCD procedures with the data and try to adjust the two distributions. This is going to be done by subtracting the (well known) $tt \to \mu\mu$ and Drell-Yan (with the NNLO cross-section) procedures.

At this point, since we are trying to estimate -and not to reject- the QCD background, which is characterized by non-isolated muons, we remove the isolation cut and instead add an anti-isolation one: we request that the sum of the tracks' P_T in a cone 0.3 around the muon, relative to the muon P_T, to be greater than 0.10 from the data. Then we try to find a scale factor that adjusts the QCD distributions to the remaining of the data[12].

So, we firstly construct the mass distributions (with the anti-isolation cut applied)

---

[12] The anti-isolation cut erases almost completely the remaining backgrounds (dibosons and W+jets) and this is the reason why they are not taken into account in the QCD study

for the two QCD Monte Carlo samples as one common distribution. This is done by appropriately multiplying each of the distributions by the following factor α:

$$\alpha_{b,c} = \frac{\sigma_{b,c} \cdot L}{N_{b,c}} \tag{4.8}$$

where $\sigma_{b,c}$ corresponds to the cross-section of the $b\bar{b}$ and $c\bar{c}$ procedures, L is the luminosity ($41.68\,\mathrm{pb}^{-1}$) and N is equal to the generated number of events in each sample.

The two weighted mass distributions are then added to give the total QCD one. We then construct the same (anti-isolated) distribution for the $41.68\,\mathrm{pb}^{-1}$ amount of data and we select a mass region where we have the highest statistics, in order to compare the two distributions. As such, it has been selected the 50-100 GeV one.

The dimuon mass plot, with the anti-isolation cut applied, for the QCD background, the data and the other two backgrounds to be removed can be seen in Figure 4.17.

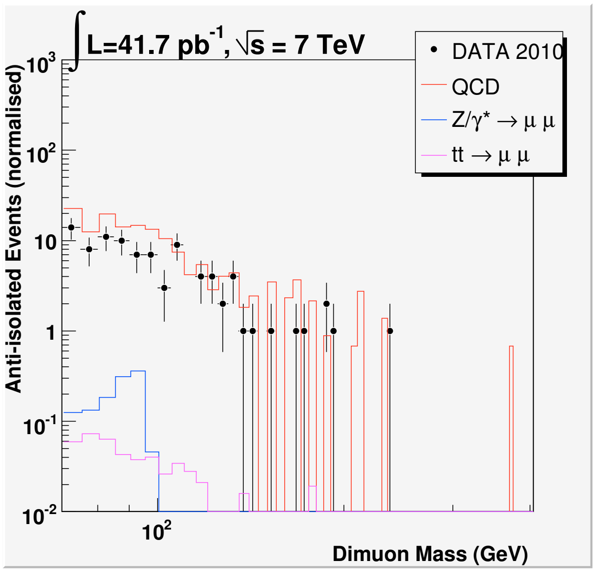

Figure 4.17: Dimuon Mass distribution, with the anti-isolation cut, for the QCD background (red), the Data (black dots) and the $Z \to \mu\mu$ (blue) and $t\bar{t} \to \mu\mu$ (magenta) procedures

The next step is the measurement of the Scale Factor, which will be used to adjust the QCD background distribution to this of the data. To calculate it, we subtract the other two backgrounds ($Z \to \mu\mu$ and $t\bar{t} \to \mu\mu$) from the data mass distribution and then divide the new mass plot with the QCD one. So, we get a ratio (per mass bin), which we try to fit with a polynomial function. This way, we can test whether there is a mass dependence of the Scale Factor (i.e., we should use a different one, depending on the mass region) or it can be considered stable.

From Figure 4.18, we see that, within statistics, we can not estimate a slope for the ratio. Therefore, we use the zero degree polynomial, thus the Scale Factor can be considered stable and equal to $S.F._{Data/QCD} = 0.64 \pm 0.06$, at least for the mass region we are testing.

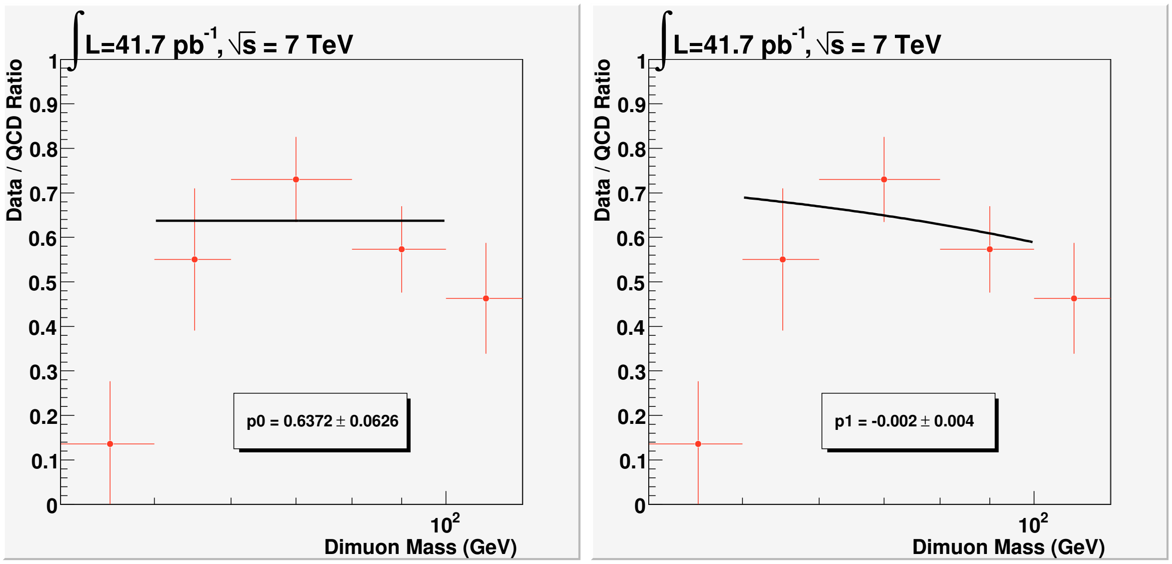

(a) (b)

Figure 4.18: Fits on the fraction Data/QCS in the Anti-Isolation case. Left: Zero degree polynomial Right: First degree polynomial

Therefore, we have to rescale the QCD distribution of Figure 4.17 with the $S.F._{Data/QCD} = 0.64$, in order to fit it to the data. The rescaled distribution can be seen in Figure 4.19.

We can now transfer the results of the anti-isolation mass plot to the isolation one, by calculating the ratio of the QCD distributions in the two cases (isolated dimuon mass / anti-isolated dimuon mass). This ratio will give us a new scale factor that will help us estimate how much QCD background we will have in the high mass region, when the isolation cut is applied (i.e., after the whole set of the selection criteria).

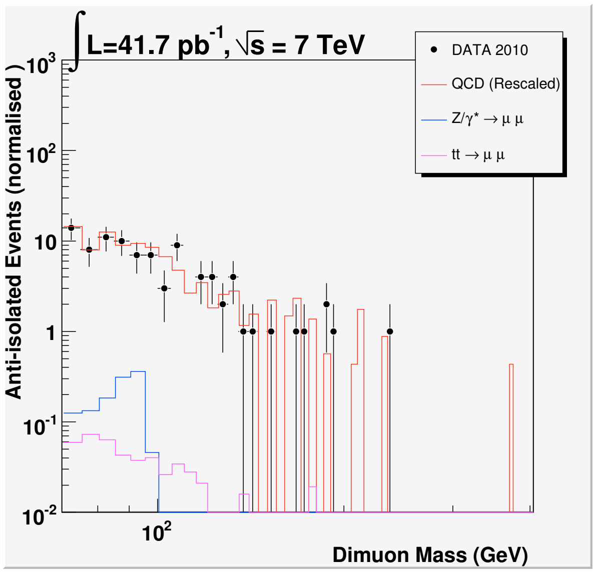

Figure 4.19: Dimuon Mass Distribution (Anti-Isolation) for the rescaled QCD background (red), Data (black dots), $Z \rightarrow \mu\mu$ (blue) and $t\bar{t} \rightarrow \mu\mu$ (magenta)

In order to increase the statistics (and reduce the errors), we perform this study by using the distribution when at least one muon is isolated (instead of both) and convert the results appropriately to the "both muons isolated" case.

We count the number of events for the at-least-one-muon-Isolated and the both-muons-AntiIsolated mass plots in the region (50GeV,100GeV) -see Figure 4.20- and we get:

$$p_1 = \frac{N_{1\mu\mathrm{Iso}}}{N_{2\mu\mathrm{Anti}}} = 4.9 \times 10^{-4} \tag{4.9}$$

Now, if p is the efficiency of exactly one muon being isolated (with respect to the case where both muons are anti-isolated), the efficiency of both being isolated is equal to p^2. Therefore the efficiency of at least one muon being isolated can also be expressed as:

$$p_1 = 2 \times [p\,(1 - p)] + p^2 \tag{4.10}$$

In the Equation 4.10, since we want the case where "at least" one muon is isolated, we have a contribution of two terms: "exactly" one muon being isolated plus both

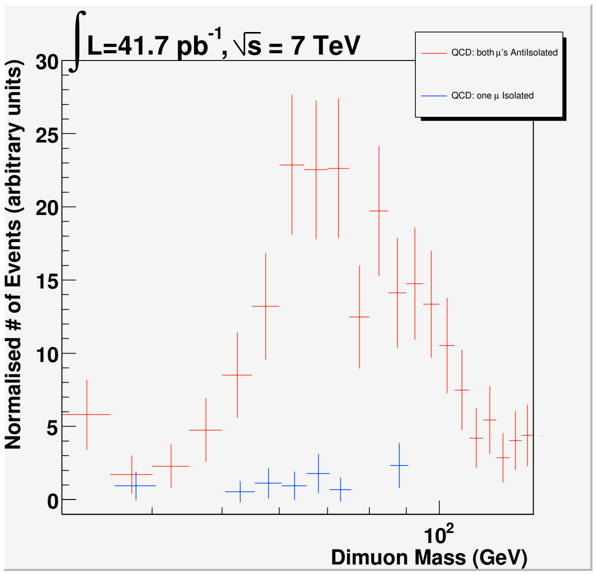

Figure 4.20: The QCD dimuon mass distributions comparison, when at least one muon is isolated (blue) and both muons are Anti-Isolated (red)

muons being isolated. This is represented in the two terms of 4.10: the first term, $[p\,(1-p)]$, gives the efficiency of one muon being isolated (p), while the other is not isolated (1-p) (the multiplication by 2 is performed to account for both muons in the event) and the second term is inserted to account for the case where both muons are isolated ($p \times p$).

So, for the efficiency p of exactly one muon being isolated, we get a second degree equation:

$$p^2 - 2p + p_1 = 0 \tag{4.11}$$

By solving Equation 4.11, we get p=0.022, therefore we conclude that the efficiency of both muons being isolated, which gives the Scale Factor for the (Both Muons Isolated)/(Both Muons AntiIsolated) distributions, is equal to:

$$p^2 = S.C._{2\mu\mathrm{Iso}/2\mu\mathrm{Anti}} \sim 5 \times 10^{-4} \tag{4.12}$$

So, we get to the point where we can extract the dimuon mass distribution of the QCD background after the final selection (i.e., including isolation): we simply rescale the anti-isolation one with the extracted Scale Factor of 5×10^{-4}. The original and the rescaled distributions are presented in Figure 4.21.

Finally, for the QCD background, since it is expected to have an extremely small contribution, we assign an uncertainty of 100%.

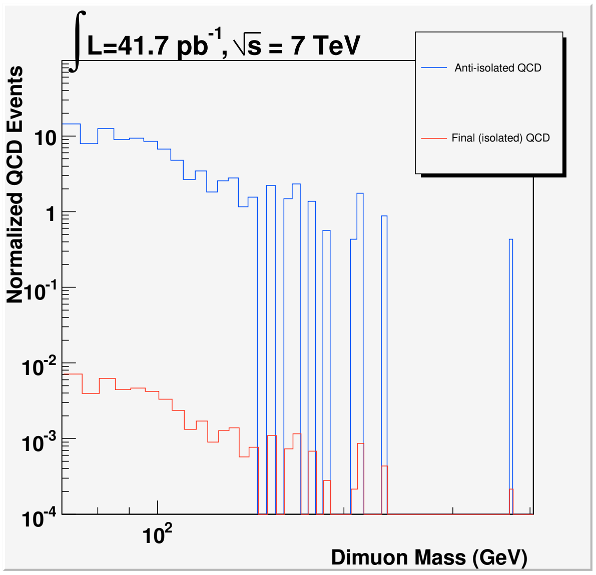

Figure 4.21: QCD background dimuon mass distributions: Anti-isolated (blue), Isolated (red)

4.9 Cosmic Background

The cosmic background can not be modeled by Monte Carlo simulation and, thus, has to be estimated directly from the data.

The cosmic background is not a real background. A cosmic particle, traversing the ATLAS detector, can be reconstructed by the Muon Spectrometer as two muons, that will appear back-to-back ($\delta\phi \sim 2\pi$). Those particles can be rather energetic and also isolated, therefore, if they remain in our sample, they can fake a signal signature. It is obviously important that we find a way to remove them.

A basic characteristic of those particles is the fact that they can not be associated to a primary vertex. The distribution, therefore, of their Impact Parameters (z_0, d_0)

will appear much broader than the one for particles from actual collisions. This is the main tool we have in our disposal to reject them: we impose some strict limits on the impact parameter values (see Section 4.5.2.7).

A demonstration of the fact that the large Impact Parameters correspond to cosmic muons can be seen in Figure 4.22, where we have plotted the z_0 and d_0 variables versus the cosine of the angle between the muon pair. It can be seen that the pairs that are characterised by large z_0 and d_0 values have a cosine extremely close to unity, therefore they appear back-to-back (i.e., it is the same track, reconstructed as two different ones).

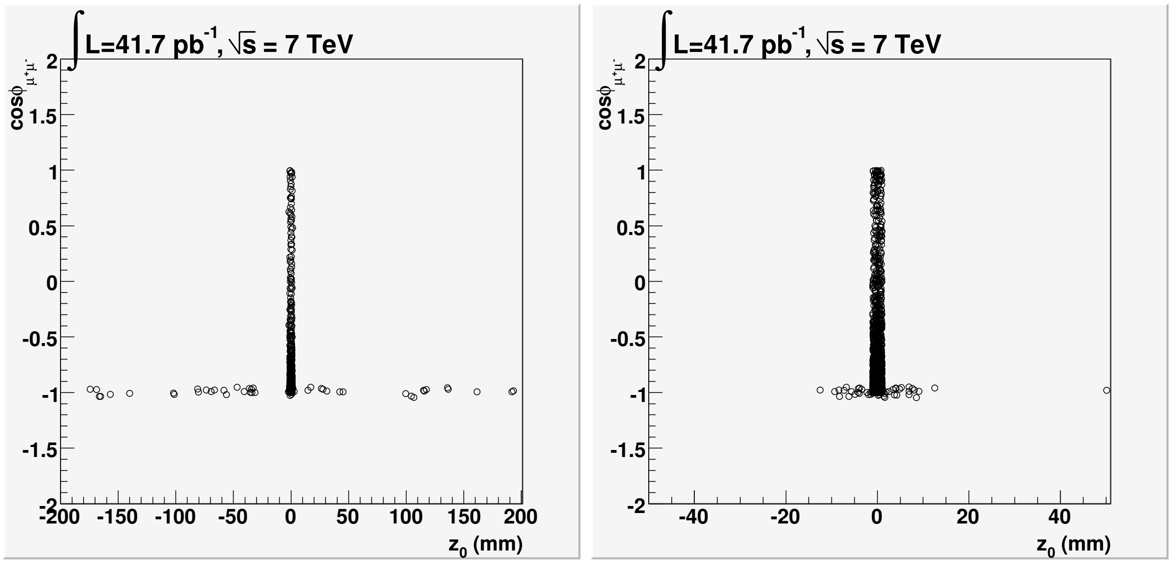

(a) (b)

Figure 4.22: Cosine of the angle of the dimuon pair versus a) z_0 and b) d_0

However, the cosmic particles traverse the detector randomly in space and time. Therefore a small fraction of them will accidentally pass close to a primary vertex, thus will not be rejected by the impact parameter cut and will remain in our data, even after the whole selection is applied. This fraction of cosmic background we try to estimate in the present section.

4.9.1 "Constructing" a cosmic-including sample

In order to study the discrimination between collisions and cosmics events, we want to use a sample that will contain cosmic particles.

Such a sample can be created from the real dataset, but with selection criteria that have less rejection power against cosmics. At the same time, though, we want to keep the high quality muon selection from the main analysis (see previous sections).

Therefore, first of all, we remove the Impact Parameter cuts and also the requirement that the dilepton pair vertex should be classified as the primary vertex. All other selection criteria remain unchanged and can be seen in Tables 4.7 and 4.8.

4.9.2 Estimation of Cosmic background Events

In Figure 4.23, we present the 2D distribution of the Impact Parameters (z_0 vs. d_0) for the muons that make it to the final step of the dedicated selection described above (i.e., no impact parameter cuts and no vertex requirements).

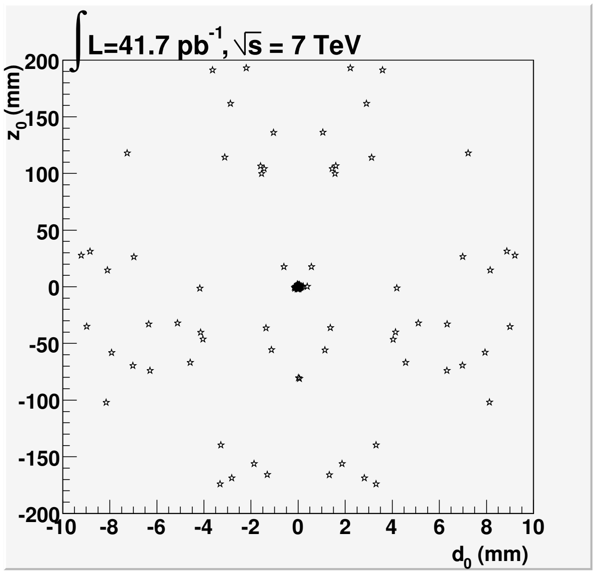

Figure 4.23: Distribution of the Impact Parameters for all muons, after cosmic dedicated selection

For estimating the total amount of cosmic background we will have within our data, we use the Impact Parameter distribution and measure the fraction of entries that lie outside the region that we reject in our main analysis ($z_0 > 1$ mm and $d_0 > 0.2$ mm, i.e. the fraction of the actual cosmic muons that are normally rejected by our criteria), over the total number of muons in the sample. More specifically, we choose the region of Figure 4.23 described by the following equations:

- $5\,\mathrm{mm} < |z_0| < 200\,\mathrm{mm}$
- $1\,\mathrm{mm} < |d_0| < 10\,\mathrm{mm}$

and count how many muons fall within. Then, assuming a uniform distribution, we extract the number of (cosmic) muons in the "accepted" region by normalizing this number to the ratio of the integrals of the two regions under study (rejected / accepted).

It turned out that we except 0.0033 cosmic events (corresponding to 0.0066 muons) after our final selection (i.e., cosmics within the impact parameter accepted region).

We repeat the same study with two more test regions:

- $5\,\mathrm{mm} < |z_0| < 100\,\mathrm{mm}$
- $1\,\mathrm{mm} < |d_0| < 10\,\mathrm{mm}$

and

- $5\,\mathrm{mm} < |z_0| < 50\,\mathrm{mm}$
- $1\,\mathrm{mm} < |d_0| < 10\,\mathrm{mm}$

The expectations, for all three test regions, are shown in Table 4.15.

So, by summarizing the results of the three different regions, we can have the final estimation for the number of cosmic events that we expect to remain within our data after the whole selection is applied:

- Cosmics Events After Final Selection $= 0.0033 \pm 0.0015\,(\mathrm{syst.}) \pm 0.0006\,(\mathrm{stat.})$

Test Region	Cosmics in Test Region	Expected Cosmics In Data
$5\,\text{mm} < \lvert z_0\rvert < 200\,\text{mm}$ $\lvert d_0\rvert < 10\,\text{mm}$	33 ± 5.74	0.0033 ± 0.0006
$5\,\text{mm} < \lvert z_0\rvert < 100\,\text{mm}$ $\lvert d_0\rvert < 10\,\text{mm}$	19 ± 4.34	0.0038 ± 0.0009
$5\,\text{mm} < \lvert z_0\rvert < 50\,\text{mm}$ $\lvert d_0\rvert < 10\,\text{mm}$	12 ± 3.46	0.0048 ± 0.0013

Table 4.15: Expected number of cosmic events in the three different test regions (second column) and after the total set of the selection criteria (third column)

4.9.3 Estimation of Cosmic background mass distribution

We now want to have an estimation about how these cosmic events that remain in our data are distributed, in terms of the dimuon mass.

To do that, we plot the dimuon mass of the events that pass all the other cuts of the analysis, but are characterised by large Impact Parameter values (namely $|z_0| > 5\,\mathrm{mm}$ and $|d_0| > 1\,\mathrm{mm}$). We then normalize this distribution to the 0.0033 events that we expect.

The dimuon mass distribution of the cosmic background that we expect to remain within our data after the final selection can be seen in Figure 4.24.

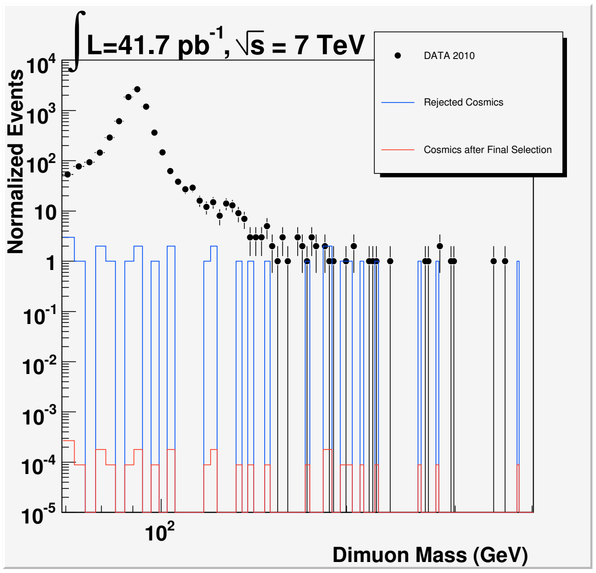

Figure 4.24: Expected dimuon mass distribution of Cosmic background rejected by (blue) and passing (red) our selection criteria. Black dots correspond to the final Data distribution

4.10 Acceptance of the Z' signal samples

In Figure 4.25, we present the dimuon invariant mass of several Z' samples, after our final selection. The total acceptance for those samples can be seen in Table 4.16. In Figure 4.26 the variation of the acceptance, versus the Z' mass, is presented.

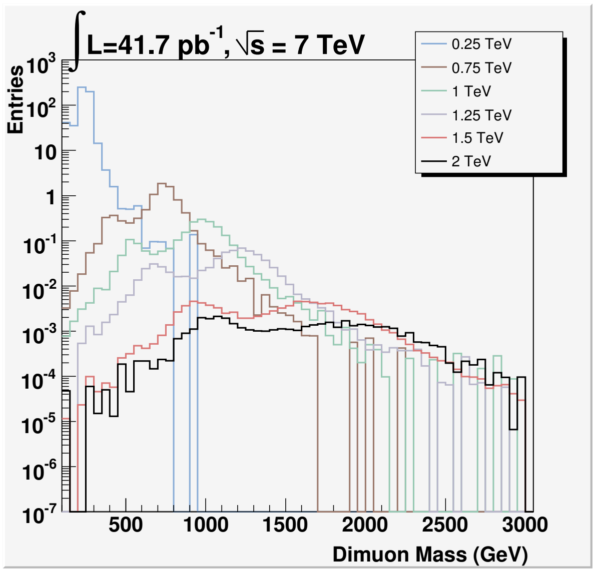

Figure 4.25: Z' dimuon invariant mass, after final selection

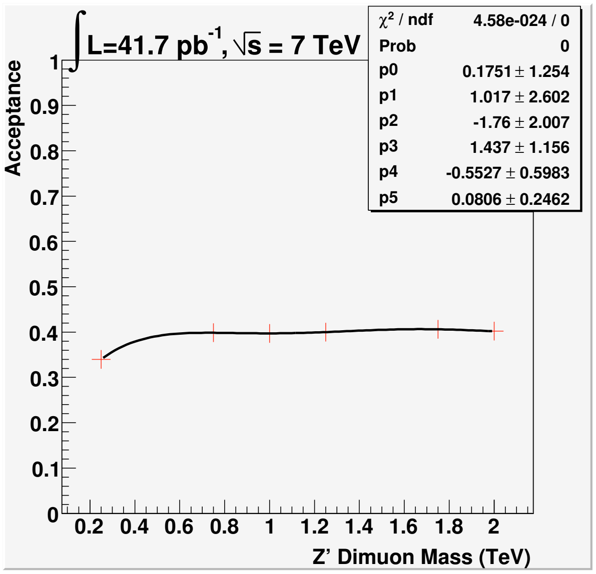

Figure 4.26: Z' overall acceptance versus mass

The total acceptance includes the kinematic, fiducial and all the selection efficiencies. As it can be seen from Figure 4.26, the overall event acceptance is of the order of 40%.

In the parallel study of the $Z' \to e^+e^-$ channel, the corresponding number was close to 60%. The main reason for having a lower acceptance in our study is the requirement that hits are observed in all three layers of the Muon Spectrometer, a fact that reduces the coverage in some regions of η. This effect, however, is expected to be recoverd in the future.

Z' Mass (GeV)	Overall acceptance (%)
250	33.9
750	39.8
1000	39.7
1250	40.0
1750	40.6
2000	40.2

Table 4.16: Overall Acceptance for several Z' masses

4.11 Efficiencies

Muons from Z' decays are expected to be quite energetic and this could cause inefficiencies at high energies. Such effects may not be well reproduced in our Monte Carlo samples and could, therefore, deteriorate the trigger efficiency. For this reason, we had to estimate the trigger efficiency on the data and then compare the Monte Carlo one to the results.

In addition, a similar study has to be performed on the reconstruction efficiency, so as to validate the Monte Carlo assumptions.

4.11.1 Trigger Efficiency

The single muon trigger efficiency has been measured by the ATLAS exotics group, using the Tag-And-Probe method (see Section 3.5.1) on $Z \rightarrow \mu\mu$. Both muons are required to pass all the offline selection cuts. The tag muon is further required to be triggered by the different triggers used in the main analysis. The invariant mass of the dimuon system has to be within the Z mass window ($|M_{\mu\mu} - M_Z| < 20\,\text{GeV}$) in order to make sure the probe muon is a real muon from Z decays. Both muons are also required to be back to back with $\Delta\phi > 0.5\pi$ and to come from the same primary vertex with $\Delta d_0 < 0.2\,\text{mm}$ and $\Delta z_0 < 1\,\text{mm}$.

The trigger efficiency is defined as the fraction of events where the probe muon is matched to the L1 and HLT trigger objects within a cone of $\Delta R < 0.4$ for the L1 trigger and $\Delta R < 0.2$ for the HLT. The efficiency, averaged over the four trigger periods, is $(83.0 \pm 0.5)\%$ for the barrel and $(94.5 \pm 0.3)\%$ for the encaps. The corresponding numbers for the Monte Carlo are $(82.32 \pm 0.06)\%$ and $(93.56 \pm 0.04)\%$. The data/MC scale factor resulted equal to 1.008 ± 0.006 for barrel and 1.011 ± 0.004 for endcap (statistical errors).

To estimate the systematic uncertainty on the trigger efficiency, several sources were considered. First, the matching cone size for the offline muon and online trigger objects, changed from the default value of 0.4 (0.2) for L1 (HLT) to 0.3 (0.1) for L1 (HLT) and also 0.5 (0.3) for L1 (HLT). The next thing that was checked was the η dependence of the data/MC scale factor for the whole period to reduce the statistical uncertainty. The (scale factor vs. η) distribution was fitted by a maximum likelihood fit, for barrel and endcap separately, to extract systematic deviation from mean value of scale factor. Finally, the size of the mass window was also changed ($\pm 15\,\text{GeV}$). The total systematic error on the trigger efficiency was measured equal to 2.1% (1.1%) for barrel (endcap) and it is dominated by the uncertainty in the η dependence.

Since either muon can trigger the whole event, it is necessary to define an event-based scale factor:

$$SF_{\mu\mu} = \frac{[1-\epsilon_{\mu 1}(Z, data)][1-\epsilon_{\mu 2}(Z, data)]}{[1-\epsilon_{\mu 1}(Z, MC)][1-\epsilon_{\mu 2}(Z, MC)]} \tag{4.13}$$

The event-based scale factor is $1.002 \pm 0.002\,(\text{stat.}) \pm 0.006\,(\text{syst})$, for both muons in the barrel, $1.002 \pm 0.001\,(\text{stat.}) \pm 0.002\,(\text{syst})$ if one muon is in barrel and the other in the endcap and, finally, $1.0009 \pm 0.0004\,(\text{stat.}) \pm 0.0011\,(\text{syst})$ if both muons are in the endcaps.

4.11.2 Reconstruction and Identification Efficiency

We are using the Tag-And-Probe method to estimate the muon reconstruction efficiency in both data and Monte Carlo and derive the data/MC scale factor.

First, we look for a good muon in the event. This muon has to pass all the selection criteria of the main analysis and it is also requested to have fired the trigger (this way we do not take into account the trigger efficiency). Every muon satisfying those conditions is the Tag.

The next step is to find the Probe track. The tracks are required to pass certain quality criteria: $P_T > 25\,\text{GeV}$, $\eta < 2.4$ and $z0 < 10\,\text{mm}$. We also want these tracks to be isolated. If the track possess an opposite charge to the tag charge and forms with it an invariant mass close to the Z boson pole mass ($81\,\text{GeV} < M_{\mu\mu} < 101\,\text{GeV}$)[13], it is characterized as the Probe. In case more that one tracks satisfy the above conditions, the one giving an invariant mass[14] closest to the Z boson pole mass is retained.

We then examine the Probe to see whether it corresponds to a real muon: there should be another muon (except the particular Tag) in the event in a adequately small dR distance from the Probe, namely $dR < 0.01$. This procedure defines the efficiency: it is the ratio of the matched probes over the total number of probes in our samples.

In the Monte Carlo part, we used the Z sample (the inclusive one) and the $t\bar{t}$. The QCD procedures ($b\bar{b}$ and $c\bar{c}$) were considered as well, but there were no events found that passed the full selection criteria. In all samples, the smearing of the P_T was applied.

---

[13] so as to remove the backgrounds

[14] with the Tag muon

In Figures 4.27 and 4.28 we present the muon reconstruction efficiency, as a function of P_T, η and ϕ, for the data (red) and the Monte Carlo (blue).

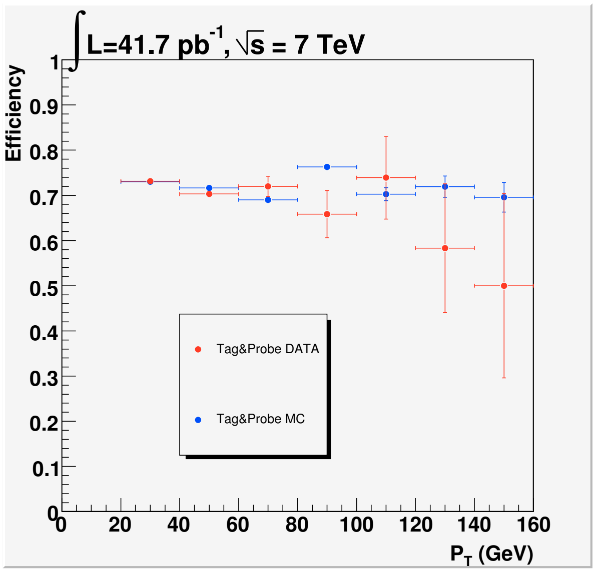

Figure 4.27: Muon reconstruction efficiency vs. P_T

The overall efficiencies for the data and the Monte Carlo were found equal to:

$$\text{Effi}_{\text{data}} = 0.698 \pm 0.006 \tag{4.14}$$

and

$$\text{Effi}_{\text{bkg}} = 0.707 \pm 0.0012 \tag{4.15}$$

The 3 Muon Spectrometer hits requirement is the reason for the decrease of the efficiency to the level of 70% (see also Appendix C).

Combining Equations 4.14 and 4.15, we get the data/MC scale factor per muon:

$$SC_{\mu} = 0.987 \pm 0.0019 \tag{4.16}$$

In order to get the scale factor per event, we multiply Equation 4.16 with itself:

$$SC_{\text{event}} = 0.974 \pm 0.004 \tag{4.17}$$

Therefore, all our Monte Carlo samples have to be normalized to the data efficiency, using the SC_{event} factor of Equation 4.17.

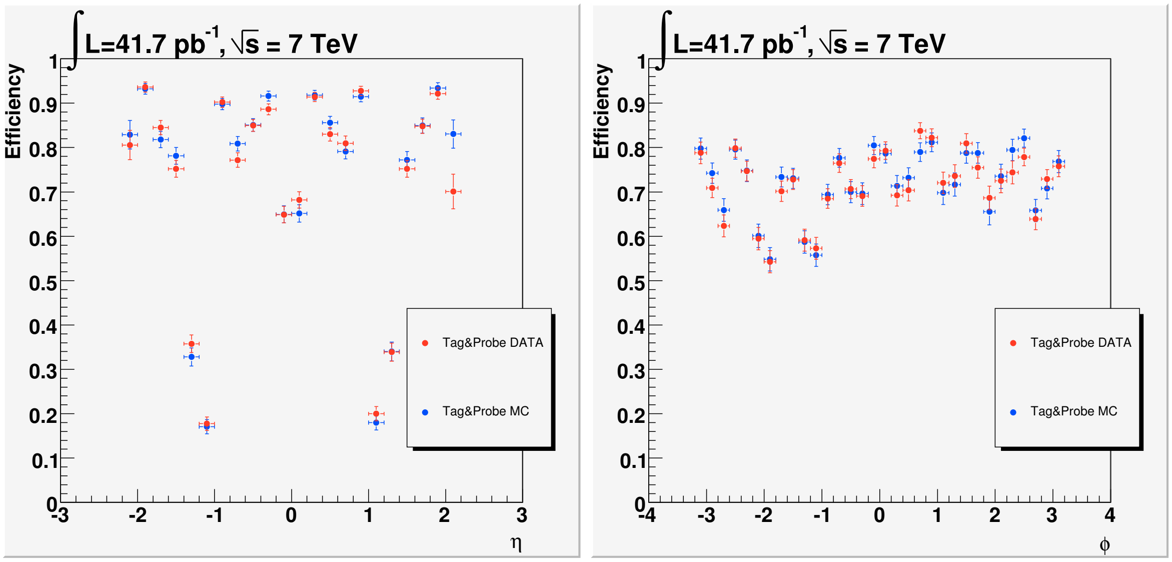

(a) (b)

Figure 4.28: Muon reconstruction efficiency vs. η (left) and ϕ (right)

4.11.2.1 Estimation of the systematic uncertainties on the Reconstruction Efficiency

We have estimated the systematic uncertainty, by applying the following alteriations:

1. MassWindow: The invariant mass cut was varied from the nominal value (81 GeV, 101 GeV) to (86 GeV, 96 GeV) and to (76 GeV, 106 GeV)
2. Track isolation: The sum of the P_T in a cone of 0.2 where the relative value with respect to the P_T of the probe track is less 0.04.
3. Tag muon P_T : Varying the P_T threshold from the nominal value 25 GeV to 20 GeV and to 30 GeV
4. Background: 10% of the backgrounds.

The systematic uncertainties are not correlated and are added in quadrature. Therefore, for the reconstruction efficiency, we conclude:

$$SC_{event} = 0.974 \pm 0.006(\text{syst.}) \pm 0.004(\text{stat.}) \tag{4.18}$$

4.11.2.2 Extrapolation to the high-P_T region

The Tag-And-Probe method provides a direct measurement of the muon identification and reconstruction efficiency. However, the method applies only to the lower P_T region, due to the low statistics in momenta above 100 GeV. At the same time, the majority of muons from the Z' decay have momenta of the order of 500 GeV and above. At such high momenta, the impact of the intrinsic single-point detector resolution dominates and muons become much more likely to lose energy via bremsstrahlung.

A dedicated study of the ATLAS exotics group showed that, although the impact of catastrophic bremsstrahlung is high (an efficiency drop of about 30% for energy loss as large as 600 GeV), at the same time the probability for a muon to radiate large amounts of energy is small, for example 1.4% of muons from the 1 TeV Z' radiate more than 50 GeV of energy.

Therefore, in general we don't expect a large drop on the efficiency at the large P_T region, however we take all the drop expected by the Monte Carlo to be the systematic uncertainty on the efficiency.

4.12 Luminosity uncertainty and normalization

ATLAS has a dedicated group (the "ATLAS luminosity group") working on the determination of the instantaneous and integrated luminosity for any data sample -with sufficient data quality.

In Figure 4.29, we present the ATLAS Total Integrated Luminosity during the 2010 data taking. The "delivered" luminosity accounts for the luminosity delivered from the start of stable beams until the LHC requests ATLAS to turn the sensitive detectors off (to allow a beam dump or beam studies). The "recorded" one is the luminosity as determined from counting rates measured by the luminosity detectors.

In Figure 4.30, we present the ATLAS data taking efficiency in 2010. The denominator is the luminosity delivered between the declaration of stable beams and the LHC request to turn the sensitive detectors off to allow a beam dump or beam studies. The numerator is the luminosity recorded by ATLAS. Each bin represents a week. The empty bins are due to weeks in which no stable beams were delivered by the LHC. The

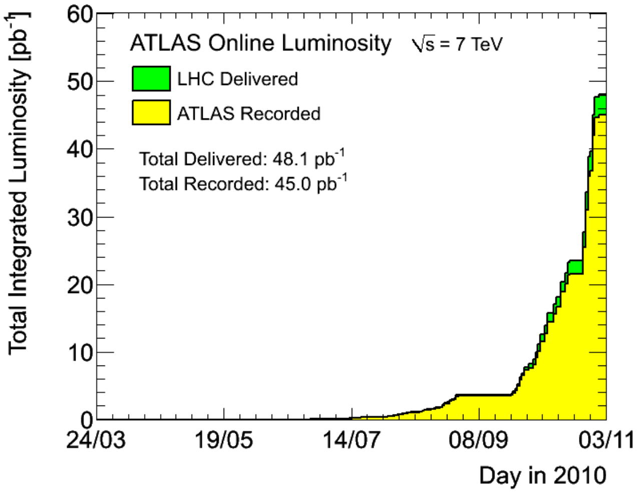

Figure 4.29: 2010 ATLAS luminosity versus day, during stable beams and for pp collisions at 7 TeV centre-of-mass energy: delivered to (green), recorded (yellow) by ATLAS

efficiency integrated (and weighted by the weekly luminosity) over this data taking period is 93.6%. The inefficiency accounts for the turn-on of the high voltage of the Pixel, SCT and some of the muon detectors (2.0%) and any inefficiencies due to deadtime or due to individual problems with a given subdetector that prevent the ATLAS data taking to proceed (4.4%)[15].

ATLAS controls the systematic uncertainties that affect the determination of the absolute luminosity using several luminosity detectors and comparing their measurements [71]. The luminosity of a pp collider can be expressed as:

$$\mathcal{L} = \frac{\mu n_b f_r}{\sigma_{inel}} \tag{4.19}$$

where μ is the average number of inelastic interactions per bunch crossing, n_b is the number of bunch-crossings producing collisions per machine revolution, f_r is the machine revolution frequency, and σ_{inel} is the pp inelastic cross-section. The product $R_{inel} = \mu n_b f_r$ gives the the rate of inelastic collisions.

ATLAS monitors the delivered luminosity by measuring the observed interaction rate per crossing μ_{vis} independently with the variety of detectors and using several

---

[15] https://twiki.cern.ch/twiki/bin/view/AtlasPublic/LuminosityPublicResults

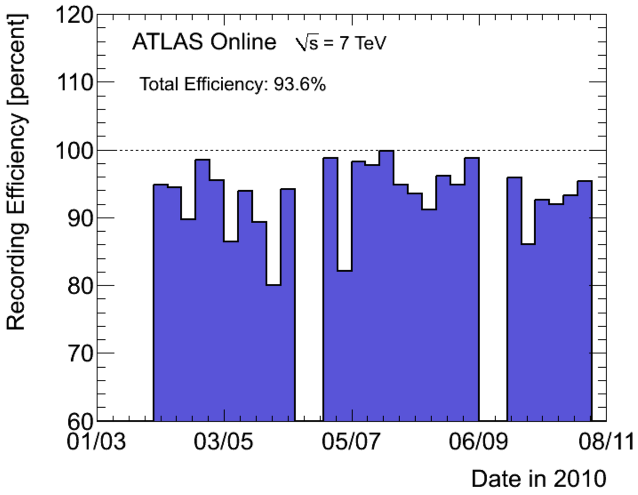

Figure 4.30: ATLAS data taking efficiency in 2010.

different algorithms. The total luminosity can then be written as:

$$\mathcal{L} = \frac{\mu_{vis} n_b f_r}{\sigma_{vis}} \tag{4.20}$$

where $\sigma_{vis} = \epsilon\sigma_{inel}$ is the total inelastic cross-section multiplied by the efficiency ϵ of a particular detector and algorithm.

These multiple detectors and the algorithms used have different characteristics, in terms of acceptance, response to pile-up and sensitivity to instrumental effects and to beam-induced backgrounds. The level of consistency across the various methods, over the full range of single-bunch luminosities and beam conditions, provides valuable cross-checks as well as an estimate of the detector-related systematic uncertainties.

Further analysis on the luminosity determination procedure is out of the aim of this study. However, what is important here is the fact that we have to find a way to overcome the uncertainty in the data luminosity determination.

This is achieved in our analysis, by normalizing the total amount of the background events to those of the data, in the Z pole mass region (70-110 GeV), where the majority of our statistics lie. The resulting normalization factor, f_{DM}, is then used to rescale the mass distribution of the Monte Carlo backgrounds (with the exeption of the QCD one, since it is already data-driven).

f_{DM} is extracted by Equation 4.21:

$$f_{DM} = \frac{N_{\text{Data}}}{N_{\text{Bkg}} \times f_E} \tag{4.21}$$

In this equation, the N_{Data} gives the number of the dimuon events in the Z pole region, which was measured equal to 7563, and N_{Bkg} is the number of the events for all background procedures:

$$N_{\text{Bkg}} = \sum_i N^i_{\text{Bkg}} \tag{4.22}$$

Finally, $f_E = 0.974$ is the reconstruction and identification efficiency scale factor per event.

4.12.1 Weighting of the Monte Carlo samples

Each one of the Monte Carlo dimuon mass distributions is getting into the final mass plots after being weighted by an appropriate factor.

For every background procedure "i", the number of events in the test region (in reality the whole dimuon distribution) has to be multiplied by a constant weight w_i, which is given by equation 4.23:

$$w_i = \frac{L_{\text{Data}} \sigma_i}{N^i_{\text{gen}}} \tag{4.23}$$

Here, $L_{\text{Data}} = 41.68 pb^{-1}$ is the most precise estimate of the ATLAS 2010 integrated luminosity[16] of the dimuon dataset, σ_i is the cross-section of the i^{th} Monte Carlo sample and N_{gen} the number of the initially generated events of each process. Therefore, if there are in total N^i_{sel} events of the i^{th} sample in the selected mass region, the number of this particular background events in the final dimuon mass plot will be equal to:

$$N^i_{\text{Bkg}} = w_i \times N^i_{\text{sel}} \tag{4.24}$$

---

[16] at the time that this study was being performed, i.e. February 2011

By summing over all the background samples, we get the total number of background events in the Z pole:

$$N_{\text{BKG}} = \sum_i w_i \times N^i_{\text{sel}} \tag{4.25}$$

This procedures gives a total of 8182.69 bacground events in the $70GeV < M_{\mu^+\mu^-} < 110GeV$ region. Therefore, the f_{DM} factor of equation 4.21 is equal to:

$$f_{DM} = 0.949 \pm 0.026 \tag{4.26}$$

4.13 Final Dimuon mass distribution - Results

In Table 4.17, the number of all background events are presented, after being normalized to the data events in the mass region 70 - 110 GeV. The final mass distributions of the data and (normalized) Monte Carlo background samples are presented in Figure 4.31. The mass distributions for three different Z' masses (750 GeV, 1000 GeV and 1250 GeV) can also be seen.

In Figure 4.31, we see that our Monte Carlo samples give a very good description of the data points. The most signal-like feature is the event with a dimuon invariant mass of 768 GeV.

4.13.1 The event at 768 GeV and the data p-value

A display of the highest invariant mass dimuon event can be seen in Figure 4.32. The dimuon pair mass was calculated equal to 768 GeV. The leading muon (in terms of momentum) has a P_T of 186 GeV and the (η, ϕ) pair equal to (-2.39, -1.54). The numbers for the second muon are, correspondingly, 165 GeV and (0.46, 1.95).

In searches for new hypothetical particles, like the present one, when one finds an excess in the distribution of the data compared to the expectation of the background, in terms of some observable -in our case, the excess in the dimuon mass- before coming to any conclusion, oughts to test if the particular excess is *statistically significant*[17].

---

[17] For a more analytical description of statistical methods, see Appendix A

Mass (GeV)	70-110	110-130	130-150	150-170	170-200
Z/γ^*	7546.6 ± 7.6	96.9 ± 2.6	33.4 ± 1.0	17.3 ± 0.6	12.8 ± 0.5
$t\bar{t}$	5.9 ± 0.2	2.3 ± 0.1	1.7 ± 0.1	1.2 ± 0.1	1.21 ± 0.1
Dibosons	10.2 ± 0.2	0.8 ± 0.0	0.6 ± 0.0	0.5 ± 0.0	0.4 ± 0.0
W+jets	0.2 ± 0.0	0.0 ± 0.0	0.0 ± 0.0	0.0 ± 0.0	0.0 ± 0.0
QCD	0.1 ± 0.1	0.0 ± 0.0	0.0 ± 0.0	0.0 ± 0.0	0.0 ± 0.0
Total Background	7563 ± 176.1	100.1 ± 2.6	35.8 ± 1.0	19.0 ± 0.6	14.4 ±0.5
DATA	7563	101	41	11	11

Mass (GeV)	200-240	240-300	300-400	400-800	800-2000
Z/γ^*	8.0 ± 0.3	7.5 ± 0.3	3.4 ± 0.2	1.4 ± 0.1	0.1 ± 0.0
$t\bar{t}$	1.0 ± 0.1	0.6 ± 0.1	0.3 ± 0.0	0.1 ± 0.0	0.0 ± 0.0
Dibosons	0.3 ± 0.0	0.3 ± 0.0	0.2 ± 0.0	0.1 ± 0.0	0.0 ± 0.0
W+jets	0.0 ± 0.0	0.0 ± 0.0	0.0 ± 0.0	0.0 ± 0.0	0.0 ± 0.0
QCD	0.0 ± 0.0	0.0 ± 0.0	0.0 ± 0.0	0.0 ± 0.0	0.0 ± 0.0
Total Background	9.4 ± 0.4	8.4 ± 0.3	3.9 ± 0.2	1.6 ± 0.1	0.1 ± 0.0
DATA	7	6	2	1	0

Table 4.17: Expected and observed number of events in the dimuon channel, normalized to the 2010 data luminosity. The uncertainties quoted include both statistical and systematic uncertainties. Entries of 0.0 indicate a value < 0.1

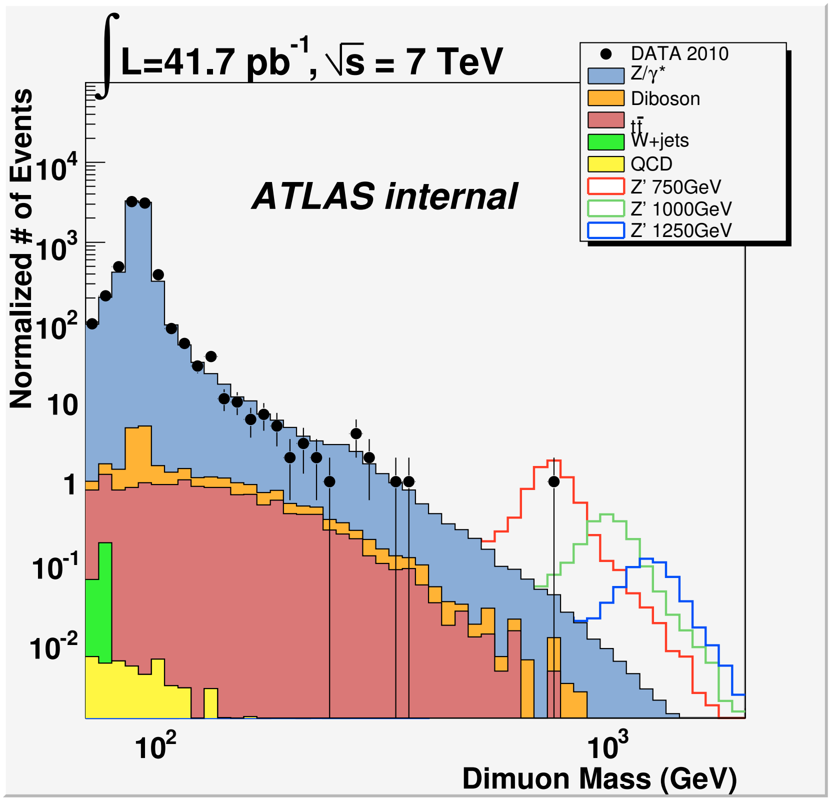

Figure 4.31: Mass distribution for the 2010 ATLAS pp data, background and Z' samples. The Monte Carlo events are normalized to those of the Data, in the Z pole mass region (70 -110 GeV)

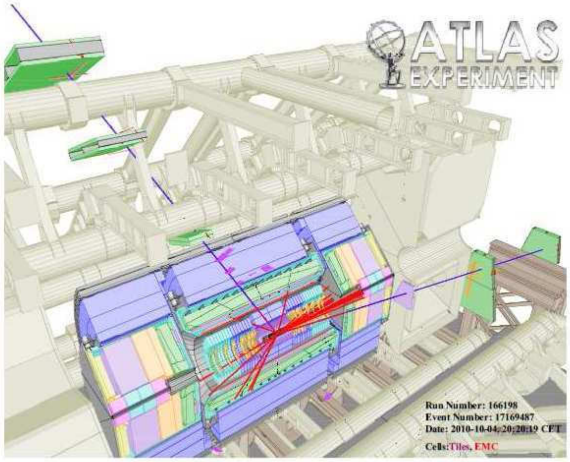

Figure 4.32: The highest dimuon mass event, at 768 GeV

A way to test that it to calculate the *p-value*. The p-value gives the probability, in the absence of signal (or, using statistical terminology, if the “null hypothesis” H0 is valid) to find a particular excess. The common convention is that a p-value less than 1.35×10^{-3} constitutes evidence for a signal (“3σ” excess), while a p-value less than 2.87×10^{-7} constitutes a discovery (“5σ” discovery).

Therefore, in order to decide whether our large event (and the total high-mass data distrubution, as well) is statistically significant, we must calculate the probability, in the absence of a Z' (i.e., only because of the background contribution), to get an event at the particular mass.

The confidence level for excluding the background hypothesis is given by:

$$1 - CL_{H0} = P_{H0}(Q \geq Q_{obs}) \tag{4.27}$$

$1 - CL_{H0}$ is the probability that the null hypothesis will give an outcome that looks at least as signal-like as the one observed in the data.

p-value is estimated with the use of Poisson probabilities. We are searching the whole mass region between 200 GeV and 1.5 TeV and, for each mass bin, using Poisson probabilities, we estimate how many times the background can give an *upward* fluctuation that is equal or greater to the bin entry of the real data. This is the so-called "local" p-value. As expected, the smallest local p-value was found in the mass bin that included the event with the largest mass (768 GeV). This p-value was found equal to 3.8% (which, still, is not small enough to indicate a local excess).

To estimate the *global* p-value, we performed 100k pseudoexperiments, in which we alternate, with Poisson statistics, the Monte Carlo bin contents (including the systematic uncertainties -see Section 4.14.3) and estimate in how many of these we get a local p-value equal or lower than the one observed in the data (3.8%). The global p-value was measured equal to 21.4%.

A p-value of that order means that there is no evidence of signal in our data. Therefore, the next step is, based on our results, to set limits on the Z' boson mass and cross-section. This is the object of the next paragraph.

4.14 Limits

In an analysis where the aim is the discovery of a theoretically predicted particle, another very important task is to also manage to reject it, if it indeed is absent. Therefore a study should be performed, to analyze the conditions required in order to positively state that the particle under investigation does not exist.

4.14.1 Mass template method

Since only a few Z' mass samples are generated and fully simulated by the official production group (see Figure 4.33), we use a flat mass sample which we reweigh to get different mass templates of the signal.

Before describing the method, a few details about the Z' cross-section have to be pointed out. In a proton-proton collision the cross section for a Z' of mass M is the sum of the following three factors[18]:

---

[18] http://highenergy.phys.ttu.edu/~gumus/dijetresonances/usefulnotes/ZpMass.txt

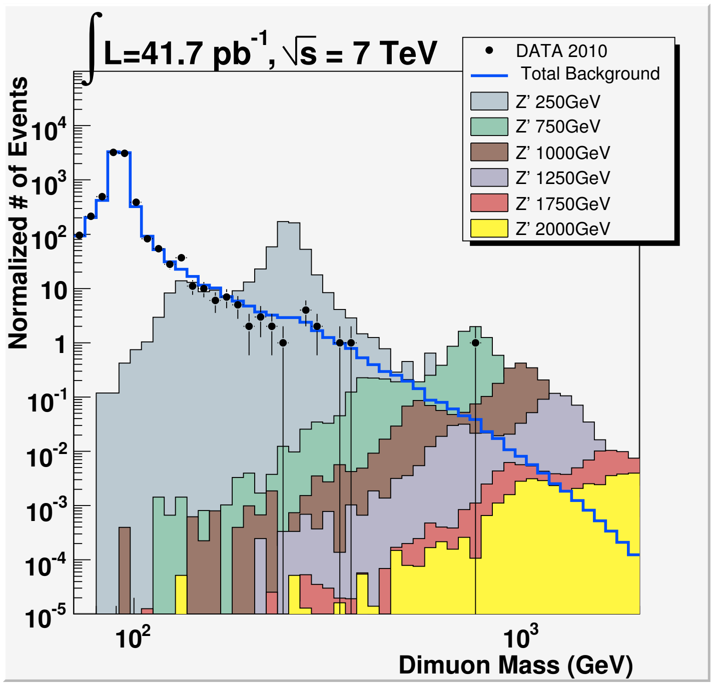

Figure 4.33: The several fully simulated Z' mass samples for 2010 analysis

- $f(q, x_1)$: the probability of finding quark q at momentum fraction x_1 in the proton
- $f(\bar{q}, x_2)$: the probability of finding antiquark $\bar{\text{q}}$ at momentum fraction x_2 in the proton
- $\sigma(m, M)$: the cross section for producing a Z' of pole mass M at actual mass m

The $f(q, x_1)$, $f(\bar{q}, x_2)$ are the *parton luminosities* and have an exponential shape. The factor $\sigma(m, M)$ is a Breit-Wigner, with a pole at M.

Based on the above, a dedicated "flat mass" sample was produced. The appropriate changes were made to Pythia, in order to remove the Breit-Wigner shape, leaving only the parton luminosity exponential shape. This exponential was in turn removed and the final result was a sample flat in mass. The Drell-Yan interference has also been turned off.

A fraction of the final mass distribution of the flat sample, after applying the selection cuts of our analysis, can be seen in Figure 4.34, without any scaling (apart from the pile-up reweigthing).

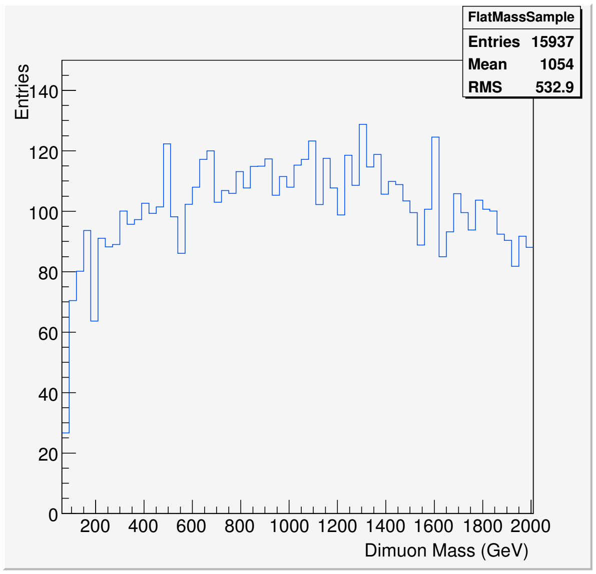

Figure 4.34: The mass distribution of the dedicated flat mass sample

Then we use an inverse procedure, in order to obtain a given mass. We first multiply with an exponential factor, to incorporate the parton luminosity exponential shape (common for all masses). Then, we reincorporate the Breit-Wigner weighting for the several masses, using a Breit-Wigner function with the desired Z' pole mass and width. In other words, we weight the final mass distribution, for each desired sample, with the following factors:

$$W_1 = exp(-\text{ExpFactor}_{Z'} \cdot \text{TrueMass}) \tag{4.28}$$

$$W_2 = \frac{1}{(\text{TrueMass}^2 - \text{PoleMass}^2)^2 + (\text{TrueMass}^2 \cdot \text{PoleWidth}^2)} \tag{4.29}$$

where $\text{ExpFactor}_{Z'} = 0.00195$.

Each template has then to be scaled with the appropriate NNLO cross-section and the luminosity of our data ($41.68\,\text{pb}^{-1}$). Table 4.18 presents the cross-sections, the k-factors and the widths (extracted from Pythia) that were used in the template construction, for the several masses.

Mass (GeV)	LO cross-section (pb)	k-factor	Pythia width (GeV)
300	18.8	1.146	8.34
400	6.40	1.138	11.43
500	2.63	1.131	14.71
600	1.27	1.123	17.99
700	0.66	1.114	21.26
800	0.361	1.104	24.50
900	0.214	1.093	27.73
1000	0.129	1.080	30.94
1100	0.080	1.064	34.15
1200	0.052	1.049	37.37
1300	0.033	1.031	40.58
1400	0.022	1.010	43.80
1500	0.015	0.991	47.02

Table 4.18: LO cross sections, k-factors and widths for the Z' templates production

The produced templates (per unit area) are presented in Figure 4.35, after the reweighting procedure.

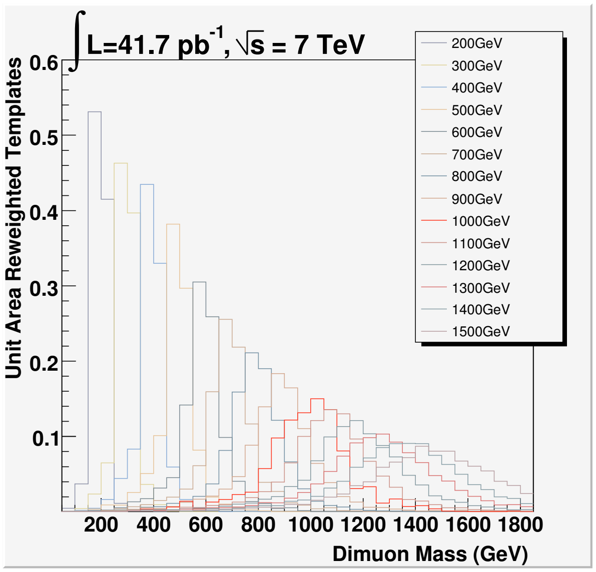

Figure 4.35: The Z' templates used for the limit setting procedure

In order to adjust the templates to the full samples' content, we must find a scale factor that equates the integrals of the two distributions in the region near the pole mass value. To do that, we must first remove the $Z/\gamma*$ interference, which is incorporated in our full samples Z' samples. In Figure 4.36, the dimuon plot for the $Z'/Z/\gamma*$ interference is presented at a pole mass of 250 GeV, along with the $Z/\gamma*$ distribution to be removed.

Then, since we have a limited number of full samples, we parametrize this scale factor, in order to get the corresponding values for all the mass templates that we have. Figure 4.37 shows the several normalization steps for the template for the 1 TeV template and the parametrization of the scale factor over the whole mass region.

The method has been validated at all the mass points where we have the fully simulated samples.

4.14.2 Limit setting method

The method we have used is described in [72].

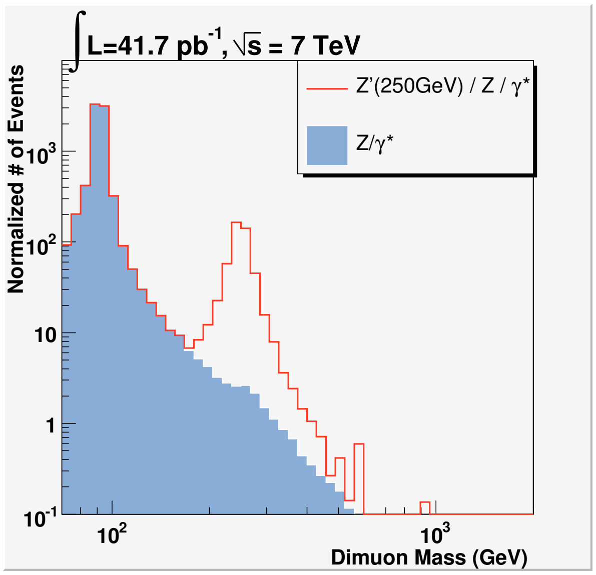

Figure 4.36: Removal of the $Z/\gamma*$ interference (blue) from the 250 GeV Z' (red)

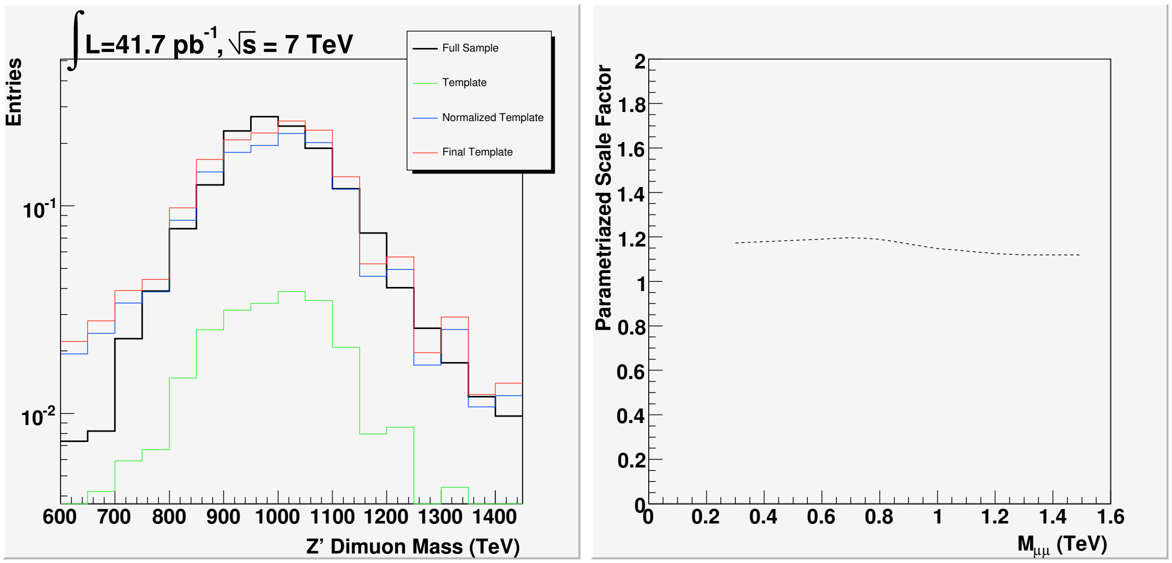

(a)

(b)

Figure 4.37: 1TeV template normalization (left) and scale factor parametrization (right)

In a search like the present one, we expect that both the number of signal and background events in the search region would be quite small and, thus, few candidate events are observed in the data. In such cases, Poisson statistics are required.

The method is based on the computation of Confidence Levels. More precisely, we have to compute the CL_{s+b}, which is the confidence level for the H1 hypothesis, and the CL_b for the H0 one, which can be evaluated by integrating the corresponding LLR distributions (via pseudoexperimets).

If LLR_{obs} is the observed test statistic (derived from the real data), then we have:

$$1 - CL_b = p(LLR \leq LLR_{obs}|H0) \tag{4.30}$$

and

$$CL_{s+b} = p(LLR \geq LLR_{obs}|H1) \tag{4.31}$$

Equation 4.30 gives us the probability that the Standard Model background can give an fluctuation which simulates a "signal-like" outcome, like the one presented in the data (i.e., H0 is still valid). Correspondingly, CL_{s+b} is the probability that the (signal+background) case can lead to a (donwward) fluctuation. A small value of CL_{s+b} tells us that the outcome is inconsistent with the H1 hypothesis (i.e. limit setting).

So, we define the CL_s parameter, which is the ratio of the two confidence levels:

$$CL_s = \frac{CL_{s+b}}{CL_b} \tag{4.32}$$

The exlusion limit for the theoretical particle is determined, if we increase the particle's cross-section until we have:

$$CL_s = 1 - \alpha = 0.05 \tag{4.33}$$

Therefore $\alpha = 0.95$ ensures a 95% confidence level on the exclusion.

4.14.3 Summary of the uncertainties for the limit program

Since, as we have shown in section 4.12, we normalize all backgrounds to the data in the region of $Z \to \mu\mu$ mass peak, the residual systematic uncertainties are small at low mass and grow at high mass.

The mass-dependent systematic uncertainties are incorporated as nuisance parameters in the likelihood function. Our study has proven that a linear increase of the uncertainty with mass is a good approximation for all effects we have considered. Therefore, we assume that the systematic uncertainties grow linearly from the Z boson pole to a specified value at a reference mass of 1 TeV.

The main source of the theoretical uncertainties for the Z' signal and the Drell-Yan background comes from the k-factors (both QCD and electroweak ones) and the Parton Distribution Functions (PDFs).

The uncertainty in the QCD k-factor includes variations of the renormalization and factorization scales by factors of two around the nominal scales and the difference in obtained k-factors when computing them for Z/γ^* vs for Z alone. This systematic uncertainty grows roughly linearly with mass and reaches the level of 2% at 1 TeV.

The uncertainty on the Electroweak k-factors (which is applicable only on the background) arises from potential contributions from $O(\alpha\alpha_S)$ corrections, higher order electroweak corrections and an assumed uncertainty of 10% on the contribution from photon induced processes. As we define the correction factors with respect to the predicted cross sections including FSR QED contributions, an additional uncertainty arises, if these contributions modify the total integrated Z/γ^* cross section. Since we use the G_μ electroweak scheme to calculate the NNLO QCD cross section predictions, which minimizes the correction at low masses, this additional uncertainty can be neglected for small invariant masses. Based on the running of the fine structure constant[19], we estimate the uncertainty to be about 3% for $M \sim 1\,\text{TeV}$.

The PDF uncertainty was estimated to vary from 3% at the Z boson pole, up to 6% at 1 TeV (9% at 1.5 TeV). Each PDF has a set of independent parameters associated with it, the "eigenvectors" of the PDF. For each eigenvector, the Z' cross section is calculated as a function of mass, by generating 100k events in PYTHIA. The (asymmetric) uncertainty is calculated by the following equations:

$$\Delta\sigma^+ = \sqrt{\sum_{i=1}^{n}(max(\sigma_i^+ - \sigma_0, \sigma_i^- - \sigma_0, 0))^2} \tag{4.34}$$

---

[19] $\alpha(Q^2) = \frac{\alpha(0)}{1-\Delta\alpha(Q^2)}$

and

$$\Delta\sigma^- = \sqrt{\sum_{i=1}^{n}(max(\sigma_0 - \sigma_i^+, \sigma_0 - \sigma_i^-, 0))^2} \tag{4.35}$$

where n is the number of the PDF eigenvectors, σ_i^+ is the cross section for the higher value of the i^{th} eigenvector, σ_i^- is the cross section for the lower value of the i^{th} eigenvector, and σ_0 is the cross section for the central value PDF. We take the larger of the two variations as the systematic uncertainty on the Z' cross section.

Regarding the rest of the Monte Carlo samples, the diboson cross section is known to next-to-leading order (NLO) with an uncertainty of about 5%. The W + jets cross section is theoretically predicted at next-to-next-to-leading order (NNLO) with about 28% uncertainty when at least one parton is requested. The $t\bar{t}$ cross section is also predicted at NNLO, with 9.5% uncertainty.

The efficiency uncertainty also increases linearly with mass, with a value of 3% at 1 TeV.

We have used the parametrization performed by the ATLAS exotics group, in order to control the uncertainties, described by Equations 4.36 to 4.39.

$$\mathrm{PDF_{unc}} = 0.0592 \cdot M_{\mu\mu} + 0.0176 \tag{4.36}$$

$$\mathrm{QCD\,k-factor_{unc}} = 0.02 \cdot M_{\mu\mu} \tag{4.37}$$

$$\mathrm{EW\,k-factor_{unc}} = 0.03 \cdot M_{\mu\mu} \tag{4.38}$$

$$\mathrm{Efficiency}_{unc} = 0.03 \cdot M_{\mu\mu} \tag{4.39}$$

where $M_{\mu\mu}$ is expressed in TeV.

In addition to the above, an uncertainty caused by the resolution smearing was considered. We raised the (already smeared) Muon Spectrometer P_T by one standard deviation[20]. This process changes the shape of the mass distribution and, consequently, the number of entries of each signal histogram[21].

---

[20] in the high P_T region, the MS dominates the momentum measurement

[21] mainly in the region around the pole mass, that we use in the limit setting

An example is presented in Figure 4.38.

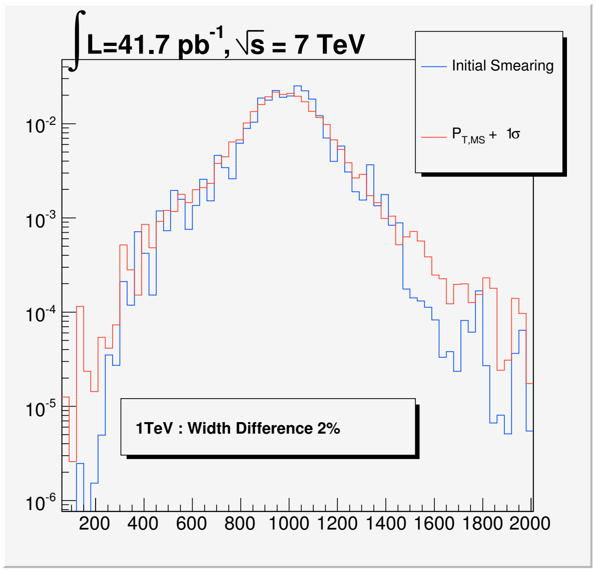

Figure 4.38: Change of smearing after the $P_{T,MS}$ raising by $+1\sigma$

By measuring the entries around the pole mass for every sample of the analysis, we can have an estimation of the uncertainty due to the resolution smearing. In Table 4.19, we present some indicative values.

Finally, the normalization uncertainty arises from the uncertainty on the $Z/\gamma *$ cross section, which is of the order of 5% and mass independent. This last uncertainty is applied to the signal only.

Table 4.20 presents the values of the uncertainty, from the several uncertainty sources, for two reference masses: 90 GeV and 1 TeV.

4.14.4 Z' NNLO cross-section

The limit on the number of produced Z' events can be converted into a limit on the cross section times branching ratio (σB), if we scale it with the observed number of the background and the theoretical value of the σB of Z'.

In order to set limits for the Z' boson mass and cross-section, we must, first of all, calculate its cross-section for the several possible masses.

Mass (GeV)	Smearing Uncertainty (%)
200	1.5
500	3.9
800	6.0
1000	5.2
1200	6.8
1500	8.1

Table 4.19: Uncertainty vs. Mass due to momentun smearing

Uncertainty source	Value at 90 GeV (%)	Value at 1 TeV (%)
PDF	2.2	7.7
QCD k-factor	0.1	2.0
EW k-factor	0.3	3.0
Efficiency	0.3	3.0
Resolution	-	2.0
Normalization (signal only)	5	5
Total	2.3	9.2

Table 4.20: Uncertainty values for two reference masses: 90 GeV and 1 TeV

Using Pythia, we produce the LO cross-section for several different masses and we calculate the values in between those, using linear extrapolation. We then convert them to the NNLO ones, by applying the QCD k-factor corrections, as described in section 4.6.1.

The variation of the Z' cross-sections, versus its mass, both LO and NNLO ones, are presented in Figure 4.39.

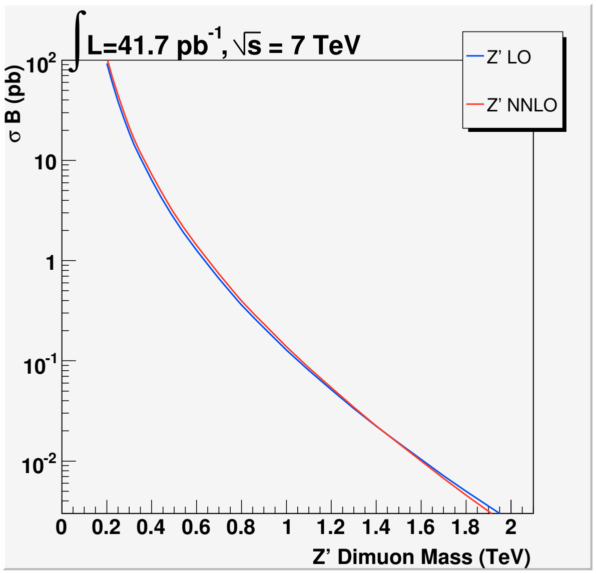

Figure 4.39: LO (blue) and NNLO (red) cross-section of the Z' boson, versus mass

4.14.5 Final Limits for 2010 ATLAS data

Figure 4.40 presents the 95% C.L. observed and expected exclusion limits on σB. For the expected limit, we also estimated the values for a $\pm 1\sigma$ and $\pm 2\sigma$ deviation of the background (the 68% and 95% envelope of the expected limits).

In the same figure, the theoretical cross section times branching ratio for the SSM Z' is presented. The thickness of the theory curve represents the total theoretical uncertainty (i.e., is a quadratic sum of the PDF and QCD k-factor uncerainties).

The observed mass limit on the SSM Z' from the 2010 ATLAS data is found to be equal to 867GeV. The corresponding cross-section that was rejected was 0.278 pb. The expected limits were correspondingly equal to 896GeV and 0.238 pb.

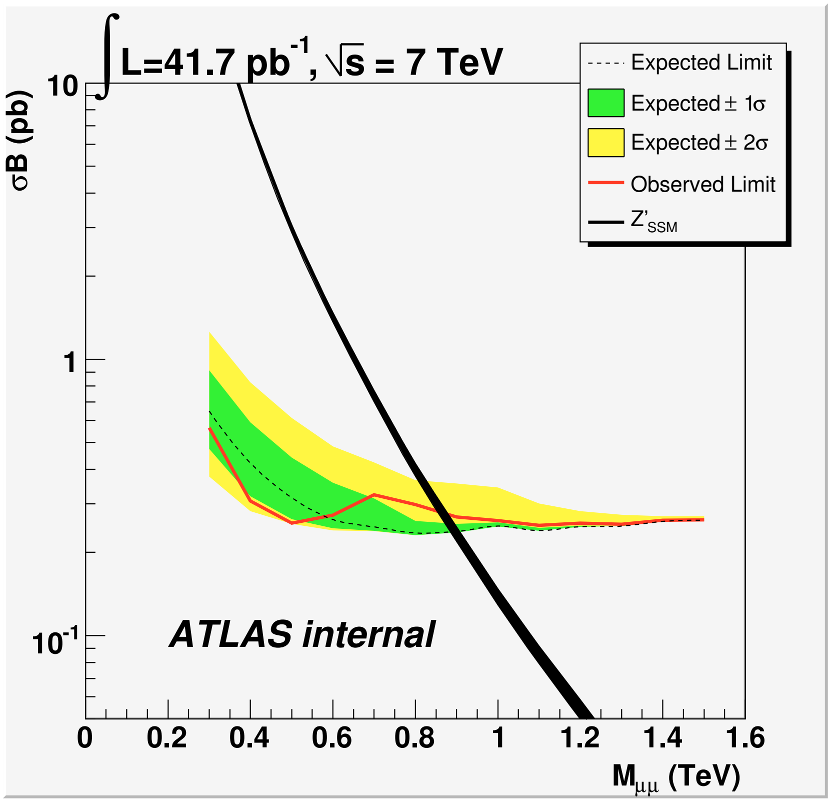

Figure 4.40: Expected and observed 95% C.L. limits on σB and expected σB forZ'

Chapter 5

ATLAS 2011 pp data Analysis

The present chapter describes the analysis that has been performed on the 2011 ATLAS pp data.

The work is based on the 2010 analysis -already presented in the previous chapter. The data used for this second part of the Z' study was collected between March and June 2011.

In the following, Reference [76] is widely used.

5.1 Run Periods

The data covers the ATLAS Run Periods B2 up to H4 for 2011 (data periods in ATLAS are always named after the english alphabet letters and they are distinguished by the year).

In Table 5.1 we present several details of the 2011 Periods we have used. Period A is not included in the table (and, as a consequence, neither in our analysis) due to the fact that a large fraction of the data was taken with solenoid and torroid fields off. For Period B1, the solenoid was on but the torroid was still off. Finally, Period C is also absent, since it was used as an intermediate energy run (at 2.76 TeV).

In Figure 5.1[1], we present the Total Integrated Luminosity in 2011, along with the ATLAS data taking efficiency per day, for the same year.

---

[1] https://twiki.cern.ch/twiki/bin/view/AtlasPublic/LuminosityPublicResults

Period	Dates of data taking	no. of Runs	Integr. Luminosity (pb^{-1})
B (B2)	Mar 22 - Mar 24	3	12
D (D1-D7)	Apr 14 - Apr 29	23	166
E (E1)	Apr 30 - May 03	5	50
F (F1-F3)	May 15 - May 25	17	137
G (G1-G6)	May 27 - Jun 14	28	518
H (H1-H4)	Jun 16 - Jun 28	9	265

Table 5.1: ATLAS 2011 data taking periods

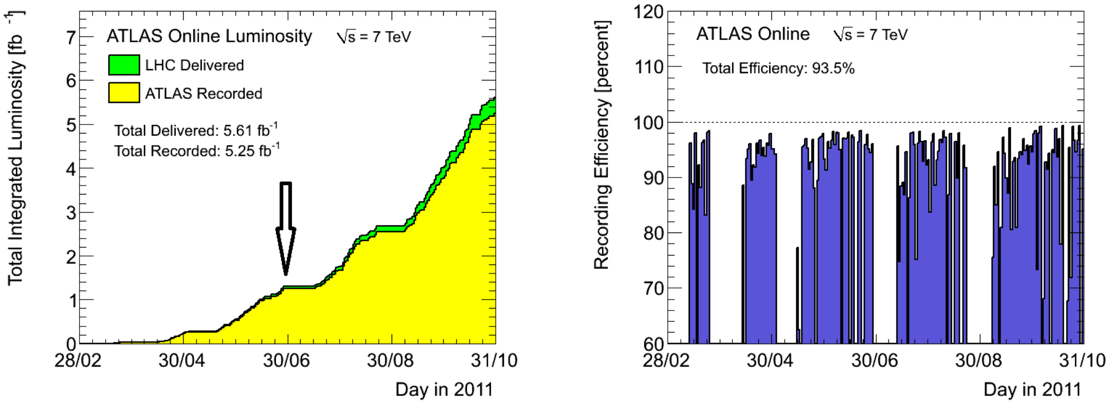

(a) (b)

Figure 5.1: 2011 total integrated Luminosity (left), data taking Efficiency per day (right). The black arrow marks the data used in the present analysis (up to June 2011)

5.2 2011 data samples

The data is skimmed, requiring the presence of at least two combined Staco OR Muid muons with $P_T > 20\,\mathrm{GeV}$. All information in ntuples is kept in the skimming. The luminosity in the muon channel, for the periods included in Table 5.1, was computed by the ATLAS luminosity calculator and found approximately equal to $1.21\,\mathrm{fb}^{-1}$.

5.3 Signal and Monte Carlo Samples

In general, the Monte Carlo samples that we have used possess the same characteristics with those of 2010 analysis (section 4.3).

Nevertheless, this time they were produced using 50 ns LHC bunch spacing, which is consistent with the bulk of the 2011 data.

5.4 Differences from 2010 analysis

In comparison to the 2010 analysis, in the 2011 data there have been some minor differences, which are presented in this chapter.

5.4.1 Pile-up Reweighting

For the 2010 data, we estimated the amount of the pile up there was in a given event by counting the number of the reconstructed vertices. In the majority of the cases, this was accurate, since it demonstrated the true in-time pile up (namely, the number of interactions in the same bunch crossing).

For the 2011 data taking, though, the LHC is running with bunch trains with an in-train bunch separation of 50 ns. This means that, in this case, the out-of-time pile up (i.e., overlapping signals in the detector from other neighboring bunch crossings) is very important. Therefore, instead of the number of vertices in a given event, we need to use the average number of pile up interactions $< \mu >$.

In Figure 5.2[2] the average number of interactions per crossing for the 2011 ATLAS

---

[2] http://atlas.web.cern.ch/Atlas/GROUPS/DATAPREPARATION/InteractionsperCrossing/

data is presented (for a total luminosity of $3\,\mathrm{fb}^{-1}$).

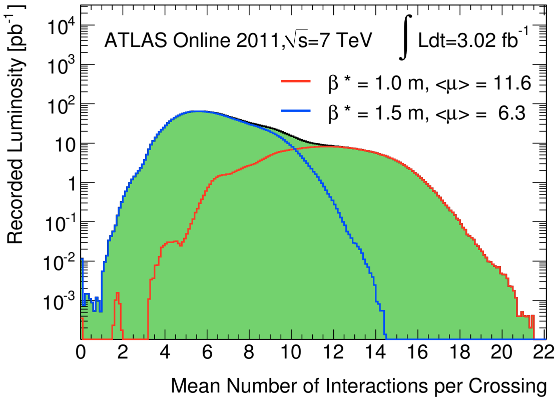

Figure 5.2: Mean number of interactions per crossing for 3 $3\,\mathrm{fb}^{-1}$ 2011 ATLAS data

Table 5.2 shows the pile up weights, which were obtained as the ratio of data/MC of the distributions of the average number $<\mu>$ of pile up interactions. The Monte Carlo samples are produced with the $<\mu>$ variable incorporated per each event and the reweighting is performed according to the table, for every produced histogram.

$<\mu>$	0	1	2	3	4	5	6	7	8	9	10
Periods B-H	0	0	0.0018	0.3506	3.2737	4.8911	3.0816	1.3117	0.0922	0	0

Table 5.2: Pile up weights, obtained as the data/MC ratio of the $<\mu>$ distributions

The ATLAS exotics groups has performed a study on estimating the uncertainty caused by pile-up effects. We plot the μ variable from data, reweight the Monte Carlo to reproduce the μ distribution from the data, then we shift the data μ (±3 RMS), reweight the Monte Carlo one more time based on these shifted distributions and finally we plot the acceptance (as a function of $m_{\mu\mu}$) with the nominal pile up reweighting and the one obtained with the original μ histogram. It has been proven that the ratio of the two curves is, within statistical uncertainties, equal to unity.

5.4.2 Selection Cuts

The selection is more or less identical to the one of the 2010 data.

For the 2011 data, since we are dealing with a much increased luminosity, we have used a set of tighter (i.e., in terms of P_T) triggers, which this time are common for all runs (and the background). We have also removed the η cut we have used in the 2010 analysis.

Another important difference is the removal of the Muon Spectrometer Barrel and Endcap overlap: a study on muons possessing both barrel and encap hits showed that their inclusion significantly worsens the resolution[3]. This is caused by residual misalignments between those two parts of the Spectrometer.

In Table 5.3, we present the differences in the selection cuts, between the two periods of the analysis.

Cut	2011 analysis	2010 analysis
Trigger	EF_mu22||EF_mu22_MG|| EF_mu40_MSonly_barrel	EF_mu13||EF_mu13_MG|| EF_mu13_tight||EF_mu13_MG_tight L1_mu10 (bkg)
$\|\eta\|$	no cut	< 2.4
pix.holes + SCT holes	< 3	< 2
MS barrel/endcap overlap	no	yes

Table 5.3: Summary of changes in selection cut between 2010 and 2011 analysis

The cut flow for the 2011 data, the Drell-Yan background (after applying the data

---

[3] about 0.5% of 3-station Z' muons have mixed barrel-endcap MDT hits

skimming[4], for reasons of compatibility) and the 1.5 TeV Z' sample are shown in Tables 5.4 and 5.5.

Cut	Data (%)	$Z \rightarrow \mu\mu$ (inclusive) (%)
Trigger	97.57	94.75
Primary Vertex (at least 3 tracks)	97.23	94.21
2 Combined muons	94.68	92.61
$P_T > 25\,\mathrm{GeV}$	76.96	82.44
IDhits	74.32	80.15
MShits	42.52	47.56
IP parameters ($z_0 < 1\,\mathrm{mm}$, $d_0 < 0.2\,\mathrm{mm}$)	41.70	47.37
Isolation $\frac{\sum_{dR<0.3} P_{T,\mathrm{tracks}}}{P_{T,\mathrm{muon}}} < 5\%$	37.64	44.66
Opposite Charge	37.63	44.66

Table 5.4: Cut Flow for the 2011 Analysis: Data and $Z \rightarrow \mu\mu$

---

[4] two MuId or Staco combined muons, with $P_T > 20\,\mathrm{GeV}$

Cut	Absolute efficiency (%)	Relative efficiency (%)
Trigger	90.8	90.8
Primary Vertex (at least 3 tracks)	90.4	99.6
2 Combined muons	75.8	83.7
$P_T > 25GeV$	74.8	98.7
IDhits	72.7	97.1
MShits	42.8	58.9
IP parameters ($z_0 < 1mm$, $d_0 < 0.2mm$)	42.7	99.9
Isolation $\frac{\sum_{dR<0.3} P_{T,tracks}}{P_{T,muon}} < 5\%$	41.5	97.1
Opposite Charge	41.5	99.9

Table 5.5: Cut Flow for the 2011 Analysis: Z' 1.5TeV

5.5 2011 ATLAS pp data Analysis

The procedure of the analysis is identical to this of 2010 and it was described in detail in Chapter 4. We examine here the most important steps.

5.5.1 Data driven QCD estimation

As in the 2010 analysis, we have to estimate the QCD background in our study from the data.

Again, we are using the *anti-isolated* muon pairs, in order to rescale the QCD distribution. It is shown that, this time, a polynomial fit of first degree is a more appropriate choice, at least for the low mass region where QCD is dominant (in the anti-isolation case). This is demonstrated in Figure 5.3.

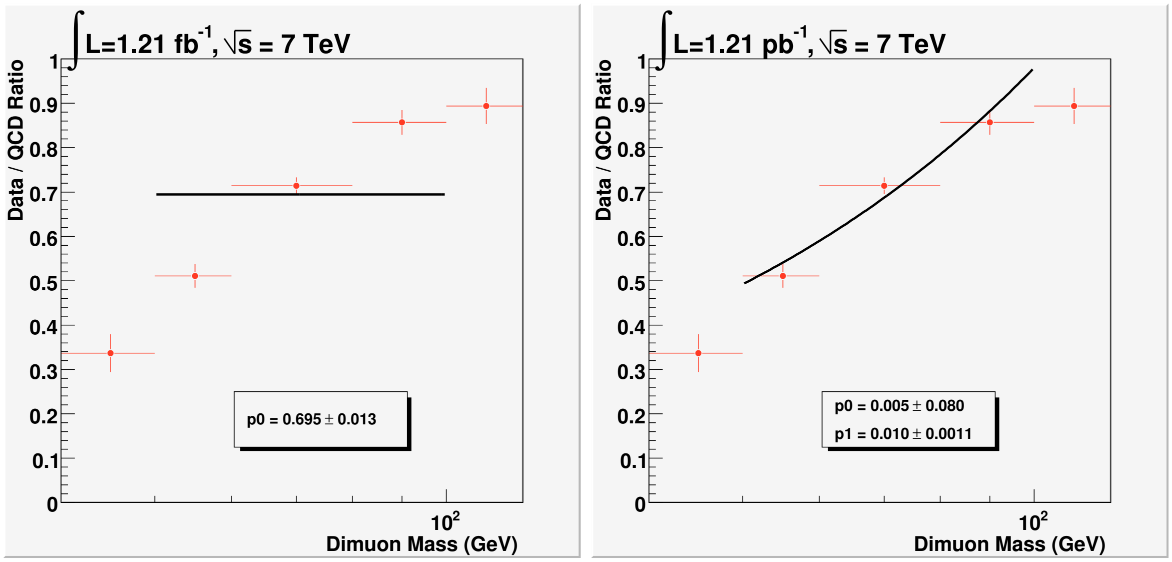

(a) (b)

Figure 5.3: Polynomial fits for the QCD distribution. Left: Pol 0 fit, Right: Pol1 fit

The fit function is:

$$f(x) = 0.005 + 0.010 \times x \tag{5.1}$$

The anti-isolated mass distributions for the data, the QCD background and the other two backgrounds that play a role in this estimation ($Z \to \mu\mu$ and $t\bar{t} \to \mu\mu$) can be seen in Figure 5.4, before and after the QCD rescaling procedure.

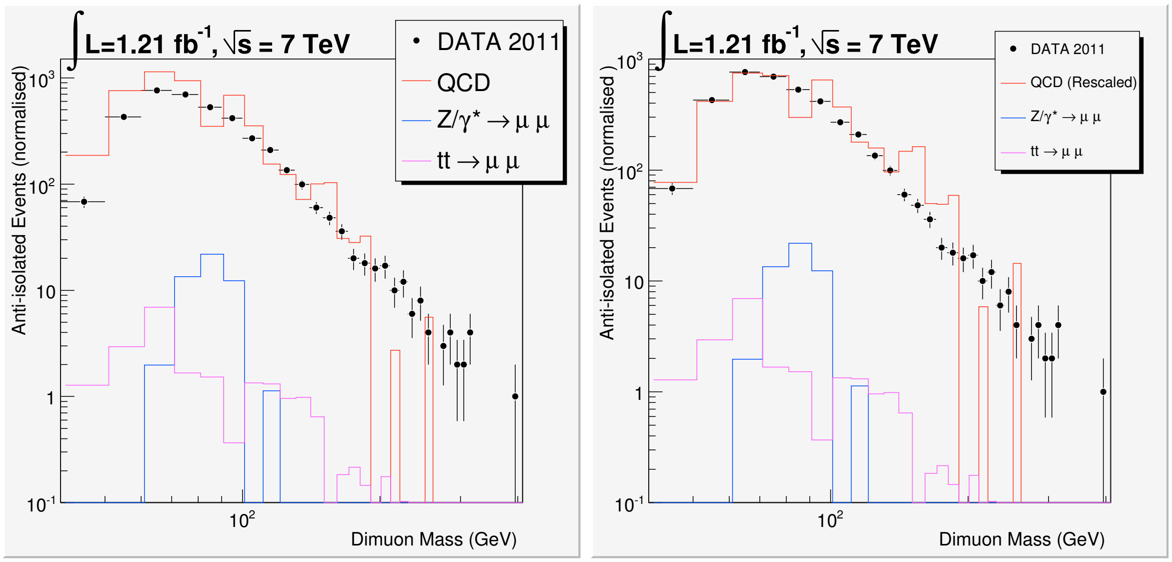

(a) (b)

Figure 5.4: Anti-Isolated dimuon mass, before (left) and after (right) QCD rescaling

The next step is to “transfer” the results in the isolation case. The new Scale Factor which is used to rescale the anti-isolated distribution in order to give the isolation one is 0.00057.

The final expected QCD background distribution is presented in Figure 5.5.

5.6 Cosmic Background

For the estimation of the Cosmic Background, we construct a “new” data sample, keeping all selection cuts immutable, with the exception of the Impact Parameter cuts and the requirement that the dilepton pair vertex should be classified as the primary vertex.

The number of cosmic events that we expect to remain in our 2011 data, after the final selection is:

- Cosmics Events After Final Selection $= 0.0172 \pm 0.0078(\text{syst.}) \pm 0.0013(\text{stat.})$

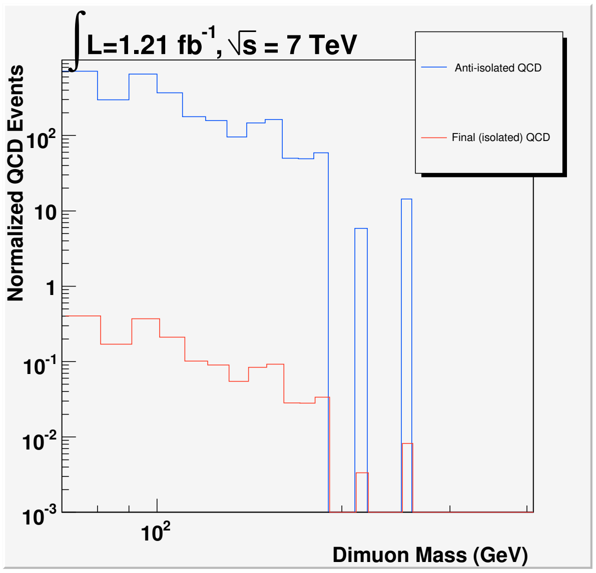

Figure 5.5: Final QCD mass distribution, after all cuts: the red histogramm is extracted from the (anti-isolated) blue one, with a Scale Factor of 0.00057

As in the 2010 analysis (where we expected 0.0033 cosmic events in our final distribution), the cosmic background in our study is negligible.

5.7 Muon efficiency studies

5.7.1 Trigger efficiency

The ATLAS exotic group has perfomed a detail study on the muon trigger efficiency with the 2011 ATLAS data, which is presented in the following.

In the tag-and-probe analysis, the trigger efficiency is defined as the fraction of events where the probe muon is matched to the corresponding HLT trigger objects.

Since we are working on a dilepton channel, there are two chances to pass a single-lepton trigger. It is, therefore, necessary to define an event-based scale factor. This is given by:

$$SF_{\mu\mu} = \frac{[1-\epsilon_{\mu 1}(Z,\mathrm{data})][1-\epsilon_{\mu 2}(Z,\mathrm{data})]}{[1-\epsilon_{\mu 1}(Z,\mathrm{MC})][1-\epsilon_{\mu 2}(Z,\mathrm{MC})]} \tag{5.2}$$

Table 5.6, shows the event-based trigger efficiency and data/MC scale factor. The event-based scale factor is calculated to be $1.0056 \pm 0.0002 \pm 0.0042$ if both muons are in the barrel region, $1.0066 \pm 0.0001 \pm 0.0024$ if one muon is in the barrel region and the other muon is in the endcap region and finally $1.0061 \pm 0.0001 \pm 0.0014$ if both muons are in the endcap region.

	Barrel-Barrel (%)	Barrel-Endcap (%)	Endcap-Endcap (%)
Data	$97.32 \pm 0.02 \pm 0.41$	$98.46 \pm 0.01 \pm 0.24$	$99.11 \pm 0.01 \pm 0.14$
MC	96.79 ± 0.01	97.81 ± 0.01	98.50 ± 0.01
SF	$1.0056 \pm 0.0002 \pm 0.0042$	$1.0066 \pm 0.0001 \pm 0.0024$	$1.0061 \pm 0.0001 \pm 0.0014$

Table 5.6: Event-based trigger efficiency and scale factor

5.7.2 Muon reconstruction efficiency

Again, we are using the Tag-And-Probe method to estimate the muon reconstruction efficiency in both data and Monte Carlo.

The requirements for the Tag muon are the same as the ones of the main 2011 analysis, plus the trigger matching one (with the 2011 trigger objects). The requirements for the Probe track are the same as in the 2010 analysis.

In Figures 5.6 and 5.7 we present the muon reconstruction efficiency, as a function of P_T, η and ϕ, for the data (red) and the background (blue).

The overall efficiency for data and background, along with the resulting data/MC scale factor per muon and per event, are presented in Table 5.7.

The study for the systematic error included, as in the 2010 analysis, the alteriation of the matching cone between the tag and the probe, by $\pm 5\,\mathrm{GeV}$, the change of the

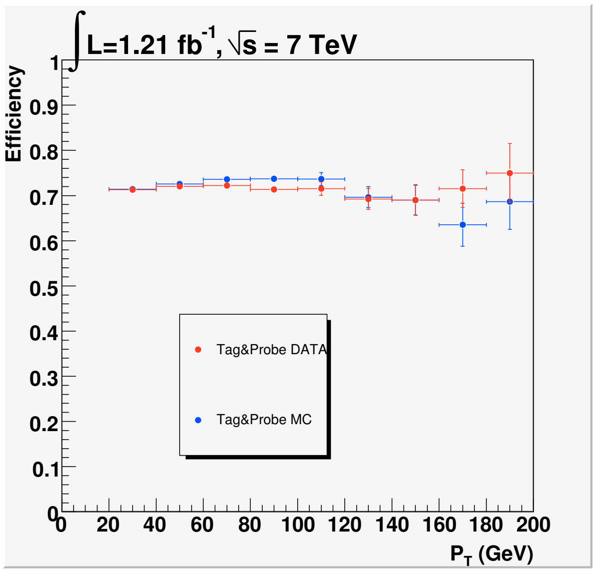

Figure 5.6: Muon reconstruction efficiency vs. P_T

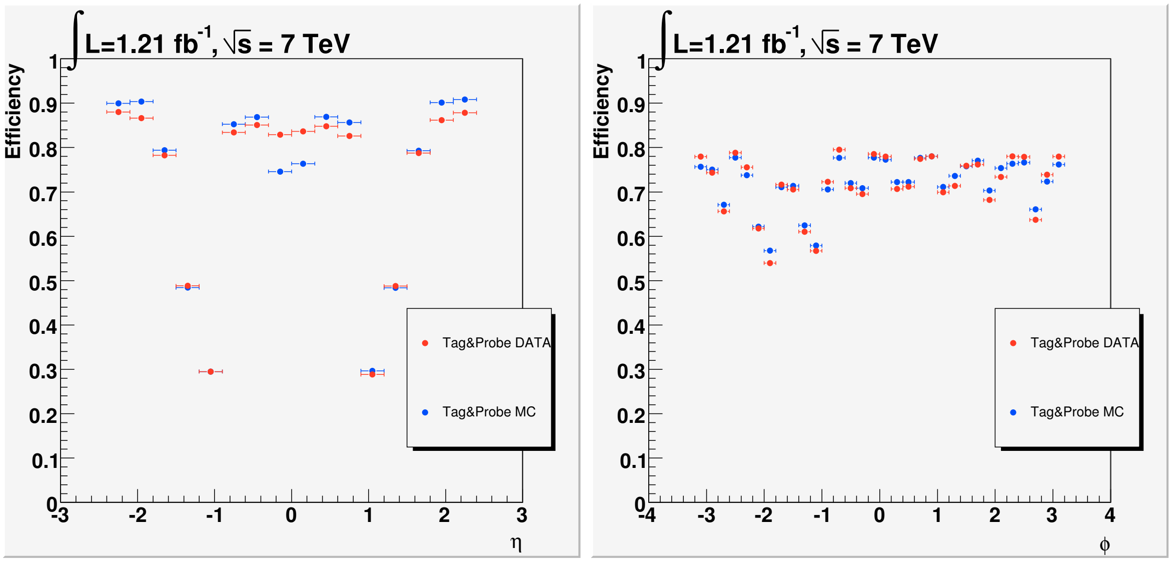

(a) (b)

Figure 5.7: Muon reconstruction efficiency vs. η (left) and ϕ (right)

	Reconstruction Efficiency Per Muon (%)
Data	71.72 ± 0.16
MC	72.02 ± 0.24
SF	99.59 ± 0.39
	Reconstruction Efficiency Per Event (%)
SF	99.2 ± 0.23

Table 5.7: Muon reconstruction efficiency and (data/MC) ScaleFactor

track isolation requirements and the limit on the tag muon P_T. The quadratic sum of these uncertainties resulted to a statistical error of 0.4%. Therefore:

$$SF = 0.992 \pm 0.004(\text{syst.}) \pm 0.0023(\text{stat.}) \tag{5.3}$$

5.8 Muon kinematics

In Figures 5.8, 5.10 and 5.11, we present the distributions of the P_T, η and ϕ variables, for the two most energetic muons ("leading" and "subleading") in the event, for the data and the Drell-Yan background.

A good agreement between data and Monte Carlo is observed[5]. The spikes in the P_T plot are due to some low statistics of the Monte Carlo inclusive Drell-Yan sample in the tail, which got multiplied by large factors. The errors of these particular bins can be seen in Figure 5.9.

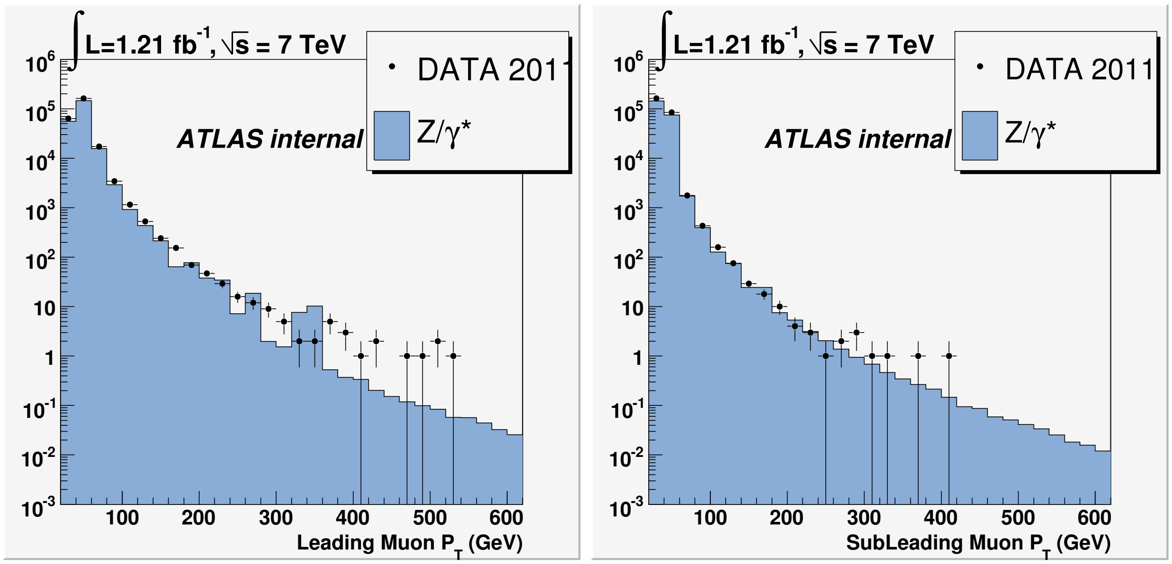

(a) (b)

Figure 5.8: P_T distribution for the Leading (left) and Subleading (right) muons

---

[5] AlpGen samples showed a better agreement than Pythia ones, but could not be used, due to low statistics

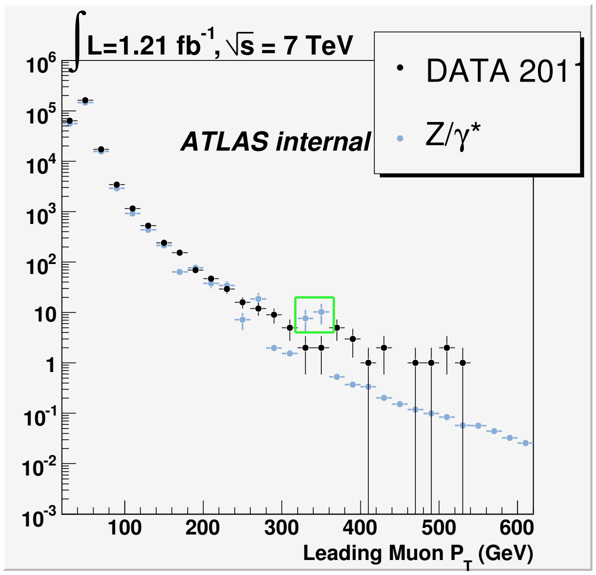

Figure 5.9: The leading μ P_T distribution with error bars

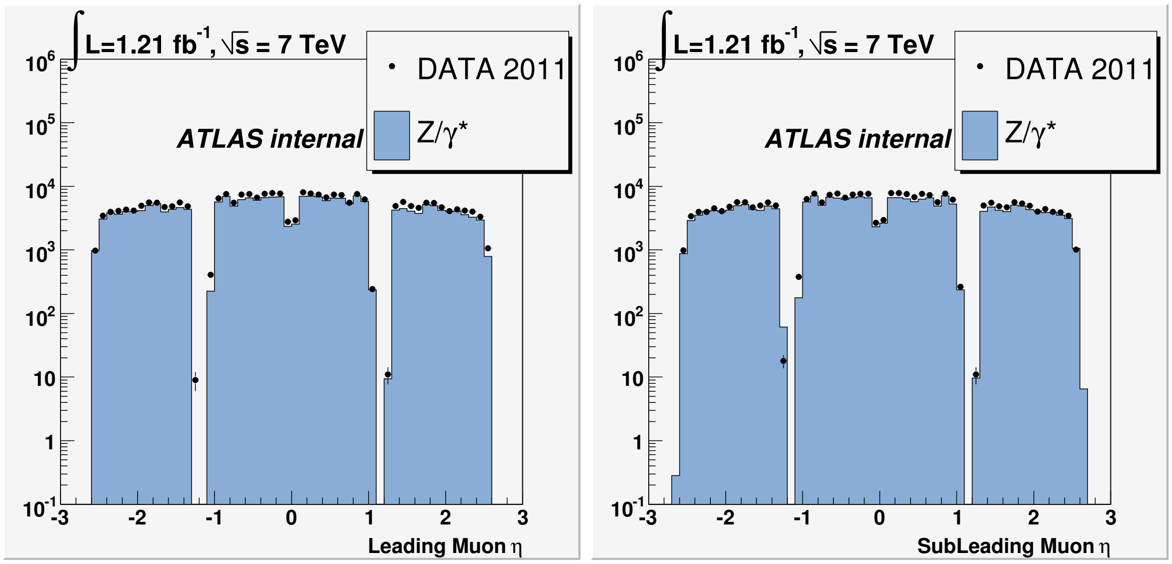

(a) (b)

Figure 5.10: η distribution for the Leading (left) and Subleading (right) muons

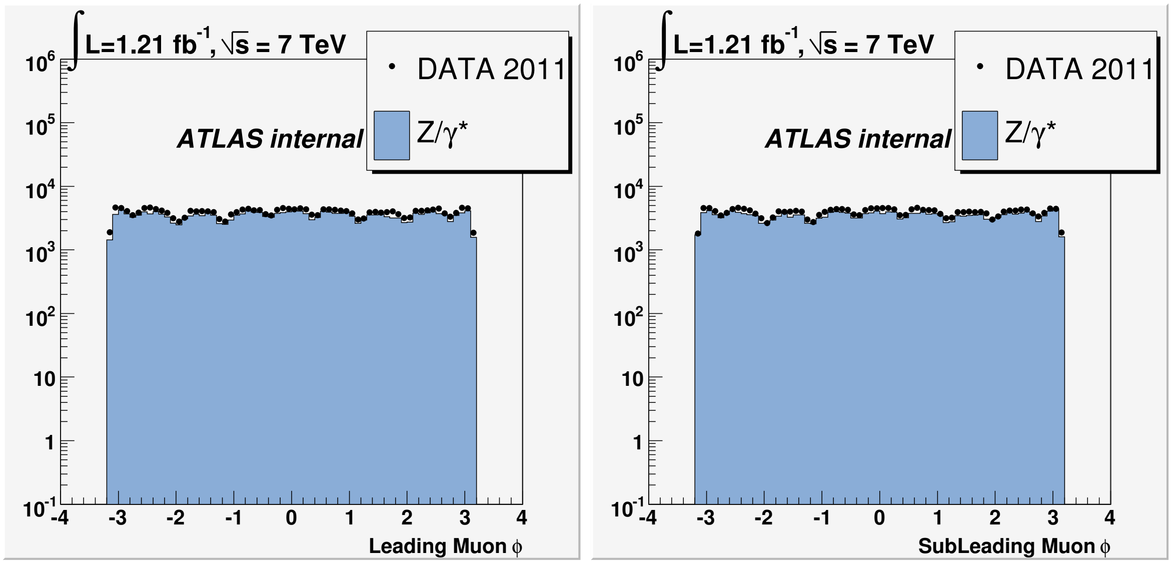

(a) (b)

Figure 5.11: ϕ distribution for the Leading (left) and Subleading (right) muons

In order to study the muon momentum resolution and its variance in the large P_T region, we are using four Monte Carlo Z' samples, namely the 500 GeV, 1 TeV, 1.5 TeV and 2 TeV ones. The corresponding reconstructed masses can be seen in Figure 5.12.

We divide the reconstructed P_T (of all the Z' samples combined) in a certain number of bins (presented in Table 5.8) and measure the resolution in each one, given by Equation 5.4.

$$\frac{\delta P_T}{P_T} = \frac{P_{T,\mathrm{true}} - P_{T,\mathrm{reco}}}{P_{T,\mathrm{true}}} \tag{5.4}$$

We also measure the resolution of the dimuon mass, for each one of the four samples separetely, according to Equation 5.5:

$$\frac{\delta M_{\mu\mu}}{M_{\mu\mu}} = \frac{M_{\mu\mu,\mathrm{true}} - M_{\mu\mu,\mathrm{reco}}}{M_{\mu\mu,\mathrm{true}}} \tag{5.5}$$

The next step is to perform Gaussian fits on all these distributions and study the variance of their standard deviations, with the increase of the mass and P_T. An example of those fits, for the Z' of 1TeV and the P_T bin 500-800 GeV can be seen in Figure 5.13.

In Figure 5.14, we present the variance of the resolution for the mass and the P_T.

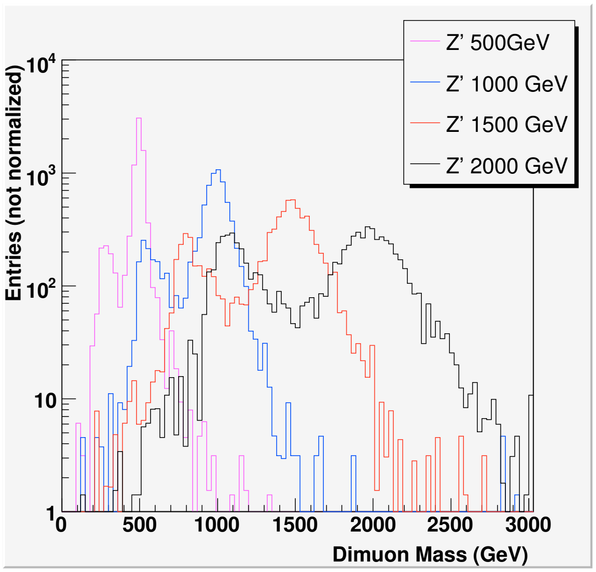

Figure 5.12: Mass distribution of the Monte Carlo Z' samples used for the resolution study

Bin	1	2	3	4	5	6
P_T (GeV)	25-45	45-65	65-85	85-110	110-150	150-200
Bin	7	8	9	10	11	12
P_T (GeV)	200-300	300-500	500-800	800-1200	1200- 1500	>1500

Table 5.8: The P_T bins used for the muon P_T resolution estimation

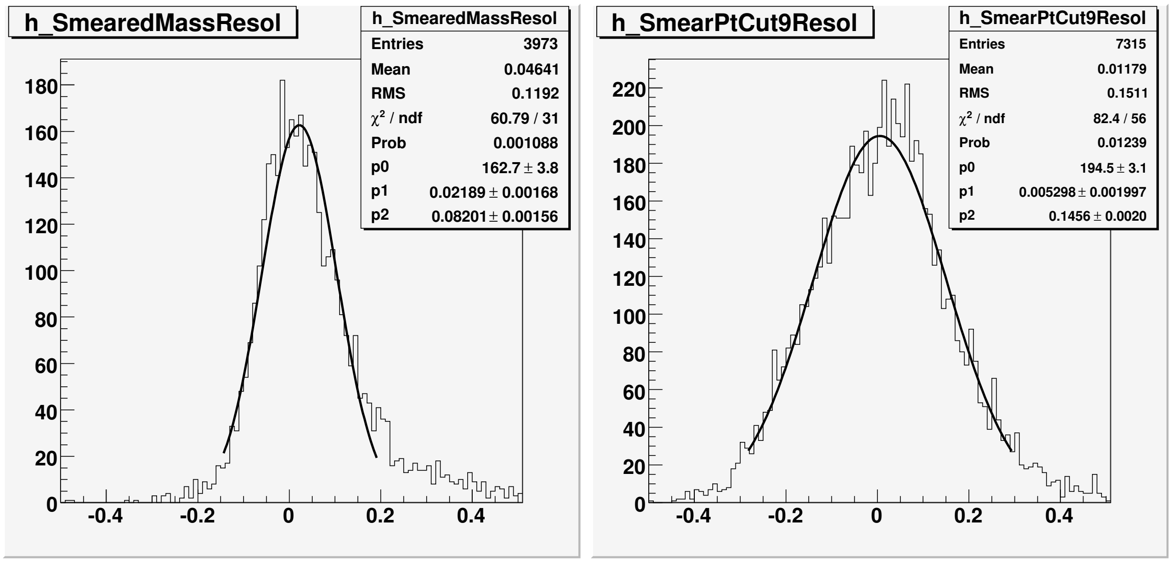

(a) (b)

Figure 5.13: Examples of the resolution Gaussian fits: 1TeV Mass (left), P_T 500-800 GeV (right)

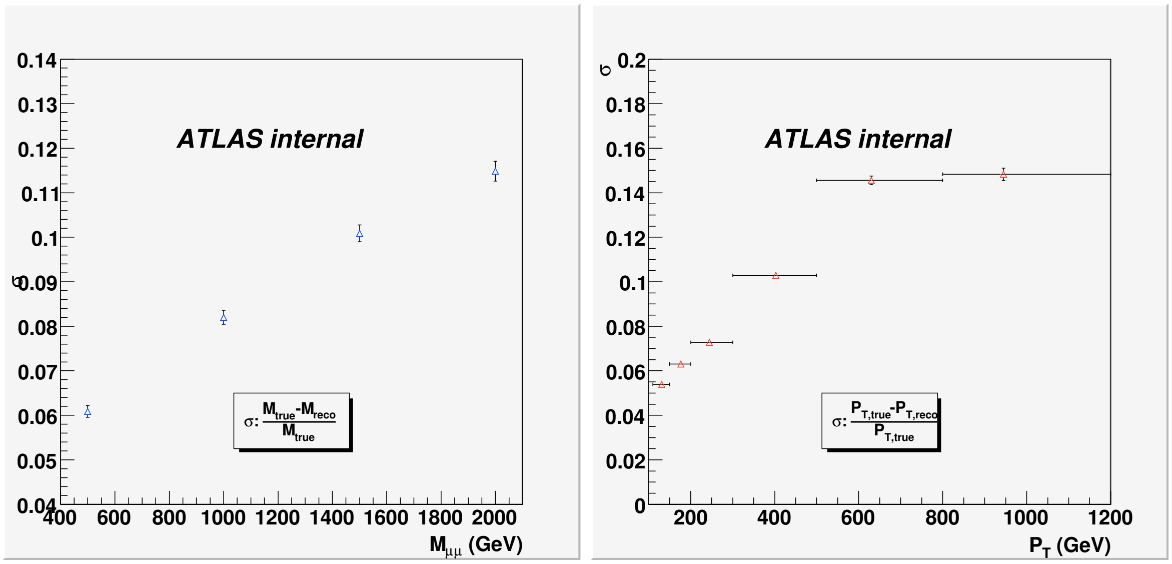

(a) (b)

Figure 5.14: Variance of the σ of the mass (left) and P_T (right) resolutions

The natural width of the Z' boson is of the order of 3% of its mass[6], therefore it is negligible in our study. Even in the lower mass of 500 GeV, where, as it can be seen from Figure 5.14(a), the mass resolution is equal to 6%, we see that $\sqrt{6^2 + 3^2} \sim 6\%$.

In order now to compare the mass and P_T resolutions, we first find the mean value and the R.M.S. of the P_T distribution for each one of the Z' samples, that can be seen in Figure 5.15. Then we plot the mass resolution σ parameter, calculated earlier, versus the mean values of the distributions of Figure 5.15.

To check the consistency, we add in the plot of the mass resolution the P_T resolution, after dividing it by factor of $\sqrt{2}$. Of course, this is only approximate and assumes that all the Z''s are produced symmetrically, namely with both muons of the same energy:

$$\begin{aligned}
M^2 &= 2 \cdot P_1 \cdot P_2(1 - \cos\theta) \Rightarrow \\
2{\cdot}M \cdot dM &= 2(P_1 dP_2 \oplus P_2 dP_1) \Rightarrow^{P_1=P_2=p} \\
M \cdot dM &= \sqrt{2}p \cdot dp \Rightarrow \\
\frac{dM}{M} &\sim \frac{\frac{dp}{p}}{\sqrt{2}}
\end{aligned} \tag{5.6}$$

The results are presented in Figure 5.16. The P_T distribution is fitted with a function of the form:

$$\frac{\delta P_T}{P_T} = [0] \oplus [1] \cdot P_T \tag{5.7}$$

The plots show that for the Z' limit which we finally calculated (see Section 5.12) and which is of the order of 1.7TeV, the mass resolution would be of the order of 11% (see Figure 5.17).

5.9 Z' signal acceptance

The total acceptance versus the Z' mass, for the 2011 analysis, can be seen in Figure 5.18. Again, it is of the order of 40%.

---

[6] http://arxiv.org/pdf/hep-ph/0610104v1.pdf

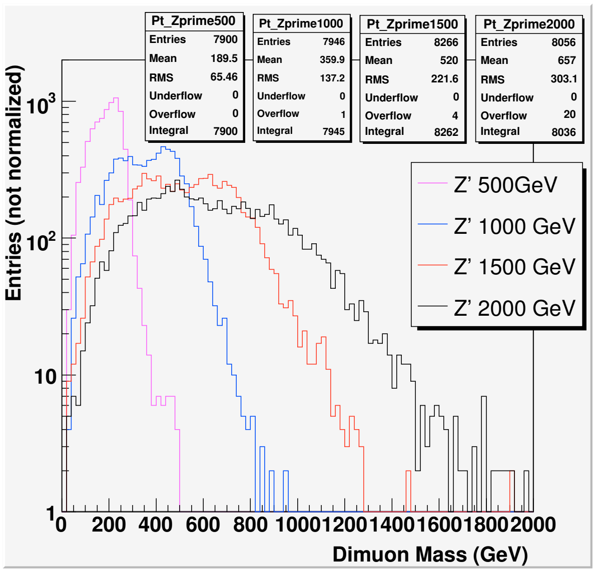

Figure 5.15: P_T distributions of the four Z' samples

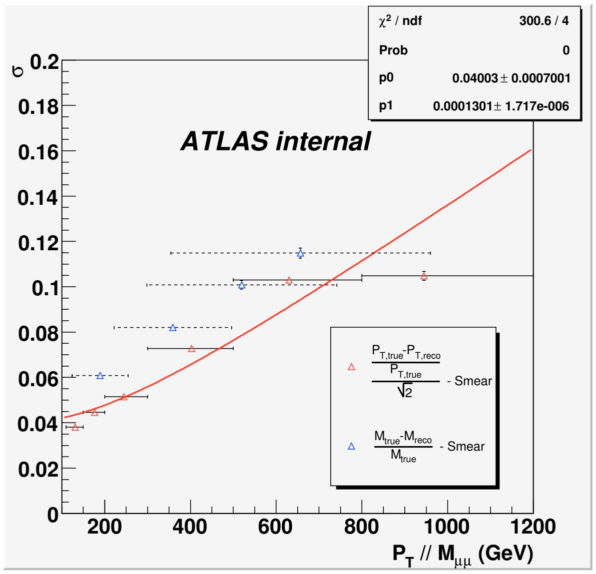

Figure 5.16: Comparison of P_T and Mass resolutions vs. P_T

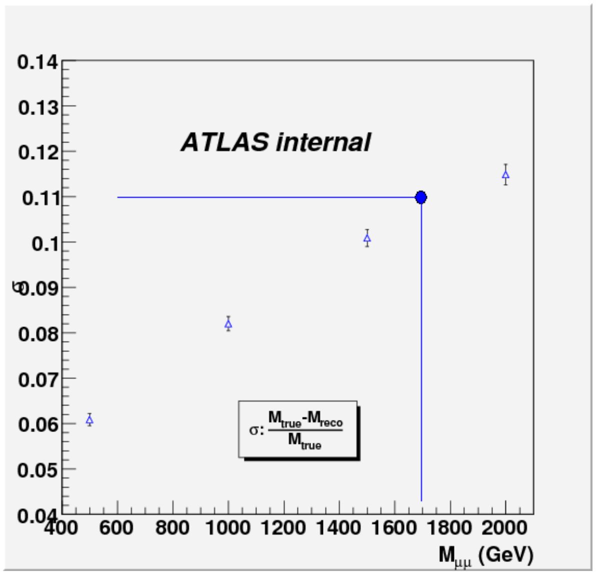

Figure 5.17: The mass resolution on the 1.7TeV Z' limit

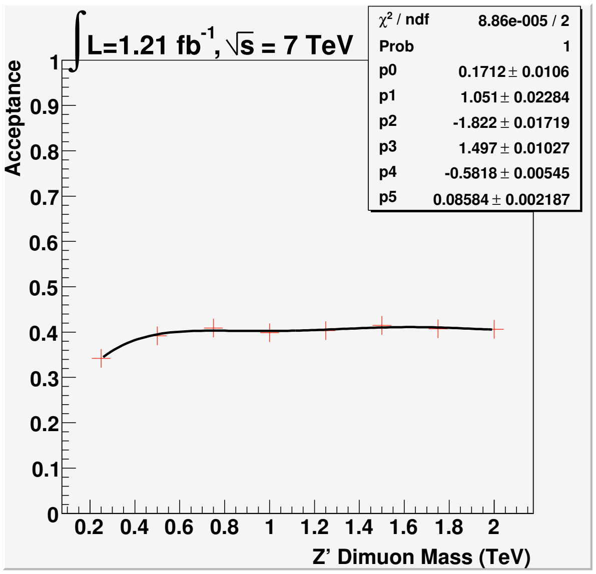

Figure 5.18: Z' overall acceptance versus mass

5.10 Normalization

After applying the data/MC reconstruction efficiency Scale Factor of 99.2% to the Monte Carlo samples (except from the QCD one, since this is estimated from the data itself), we have to account for the uncertainty in the luminosity. The procedure was the same as in the 2010 analysis: we count the sum of all the background mass histograms in the mass bin of 70-110 GeV and then we request a $(\text{data/MC})_{\text{lumi}}$ scale factor that makes this sum equal to the data entries in the same mass region.

The resulting scale factor is equal to:

$$(\text{data/MC})_{\text{lumi}} = 0.962 \pm 0.002 \tag{5.8}$$

Table 5.9 shows the number of observed events in bins of reconstructed dimuon invariant mass, along with the expectation from various background sources.

5.11 Results - Final Mass Distribution

In Figure 5.19, we present the final mass distributions for the 2011 data, the several background procedures and three different Monte Carlo Z' masses (1, 1.25 and 1.5 TeV). Like in 2010, we see a very good agreement between the Monte Carlo samples and the data points.

In Table 5.10, we present the four events with the largest masses in the 2011 Data and the characteristics of the corresponding muon pairs.

The ATLANTIS event displays are shown in Figures 5.20 up to 5.23.

5.12 Limits

Since the p-value for the 2011 ATLAS data was very large (local p-value $\sim$11% in the mass bin around 550 GeV and $\sim$99% globally in the search region 300 GeV - 2 TeV), we proceeded to extracting limits on the Z' existence.

As in the 2010 analysis, we have used the template method. Again, we produced the dimuon distribution for several Z' pole masses, using the flat sample mass and with the same parameters (resolution widths and weights) as in the 2010 analysis.

Mass (GeV)	70-110	110-130	130-150	150-170	170-200
Z/γ^*	235627 ± 232.2	3117 ± 83.4	1060.6 ± 32.4	523.9 ± 18.4	399.5 ± 15.3
$t\bar{t}$	185.9 ± 7.3	69.3 ± 4.0	45.0 ± 2.6	35.2 ± 1.3	38.6 ± 1.5
Dibosons	303.0 ± 7.3	24.5 ± 1.1	17.4 ± 0.9	13.7 ±0.9	12.9 ± 0.8
W+jets	1.3 ± 0.4	0.4 ± 0.2	0.0 ± 0.0	0.2 ±0.2	0.0 ± 0.0
QCD	1.1 ± 1.1	0.2 ± 0.2	0.1 ± 0.1	0.1 ± 0.1	0.1 ± 0.1
Total Background	236118 ± 5494.0	3211.5 ± 83.5	1123.1 ± 32.5	573.2 ± 18.5	450.9 ± 15.4
DATA	236118	3158	1149	580	446

Mass (GeV)	200-240	240-300	300-400	400-800	800-2000
Z/γ^*	221.9 ± 9.6	186.8 ± 7.3	90.3 ±4.0	40.3 ± 2.4	2.0 ± 0.2
$t\bar{t}$	29.4 ± 1.2	21.7 ± 1.0	11.3 ± 0.5	4.0 ± 0.2	0.1 ± 0.1
Dibosons	8.9 ± 0.7	7.5 ± 0.6	6.7 ± 0.6	1.3 ± 0.2	0.0 ± 0.0
W+jets	0.0 ± 0.0	0.1 ± 0.1	0.0 ± 0.0	0.0 ± 0.0	0.0 ± 0.0
QCD	0.0± 0.0	0.0 ± 0.0	0.0 ± 0.0	0.0 ± 0.0	0.0 ± 0.0
Total Background	260.3 ± 9.7	216.0 ± 7.3	108.2 ± 4.1	45.7 ± 2.5	2.1 ± 0.2
DATA	272	190	90	45	3

Table 5.9: Expected and observed number of events in the dimuon channel, normalized to the 2011 data luminosity. The uncertainties quoted include both statistical and systematic uncertainties. Entries of 0.0 indicate a value < 0.1

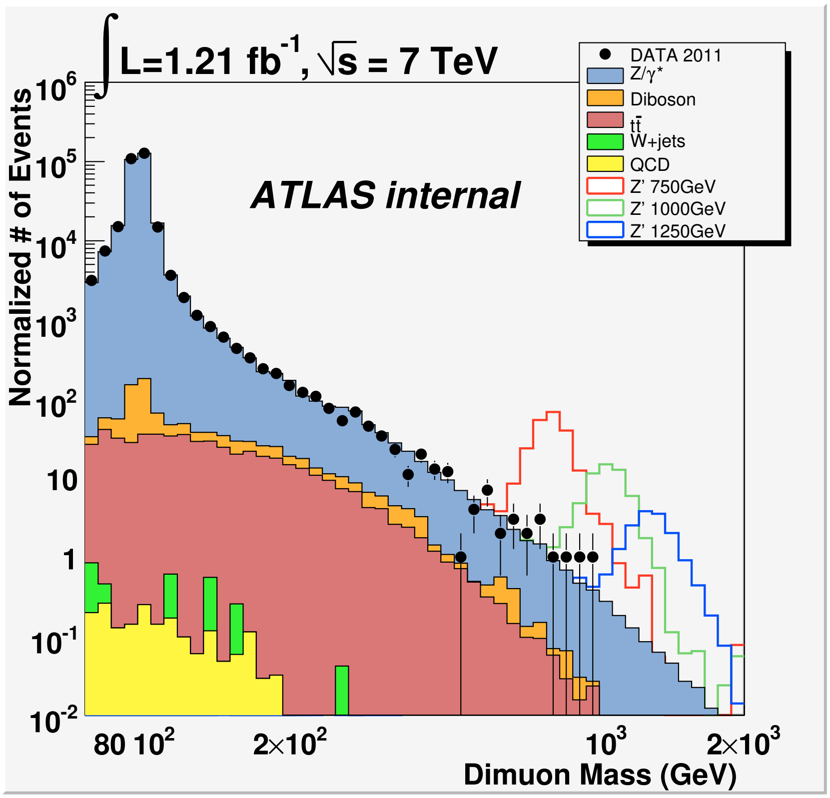

Figure 5.19: Mass distribution for the 2011 ATLAS pp data, background and Z' samples. The Monte Carlo events are normalized to those of the Data, in the Z pole mass region (70-110 GeV)

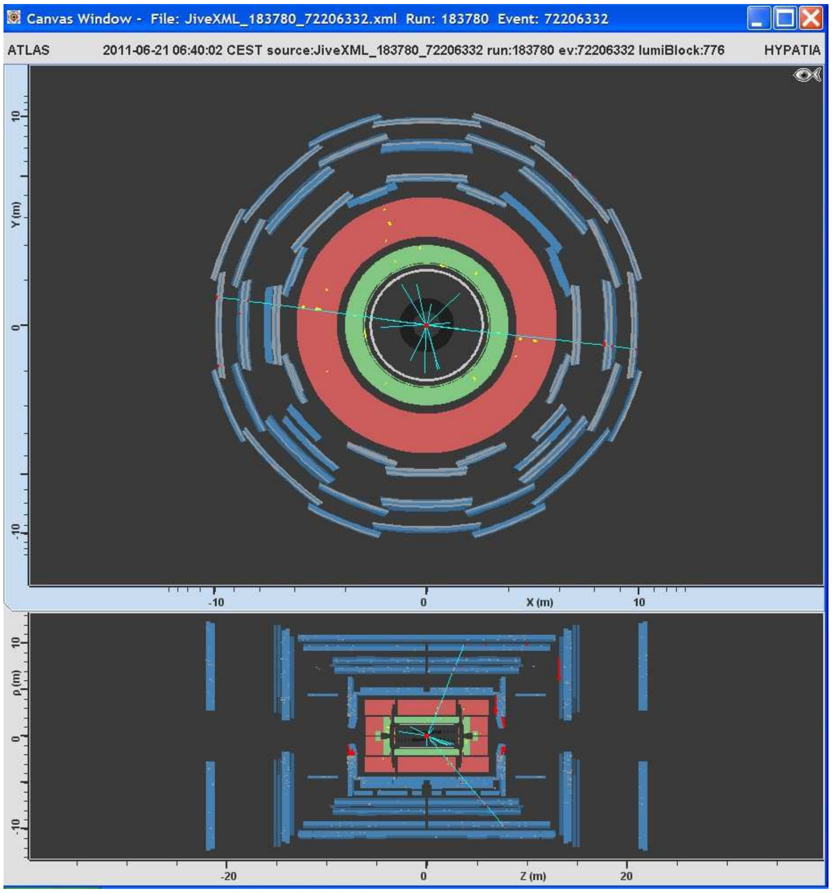
Canvas Window - File: JiveXML_183780_72206332.xml Run: 183780 Event: 72206332

ATLAS 2011-06-21 06:40:02 CEST source:JiveXML_183780_72206332 run:183780 ev:72206332 lumiBlock:776 HYPATIA

Figure 5.20: RunNumber 183780, EventNumber 72206332 : Invariant Mass 949 GeV

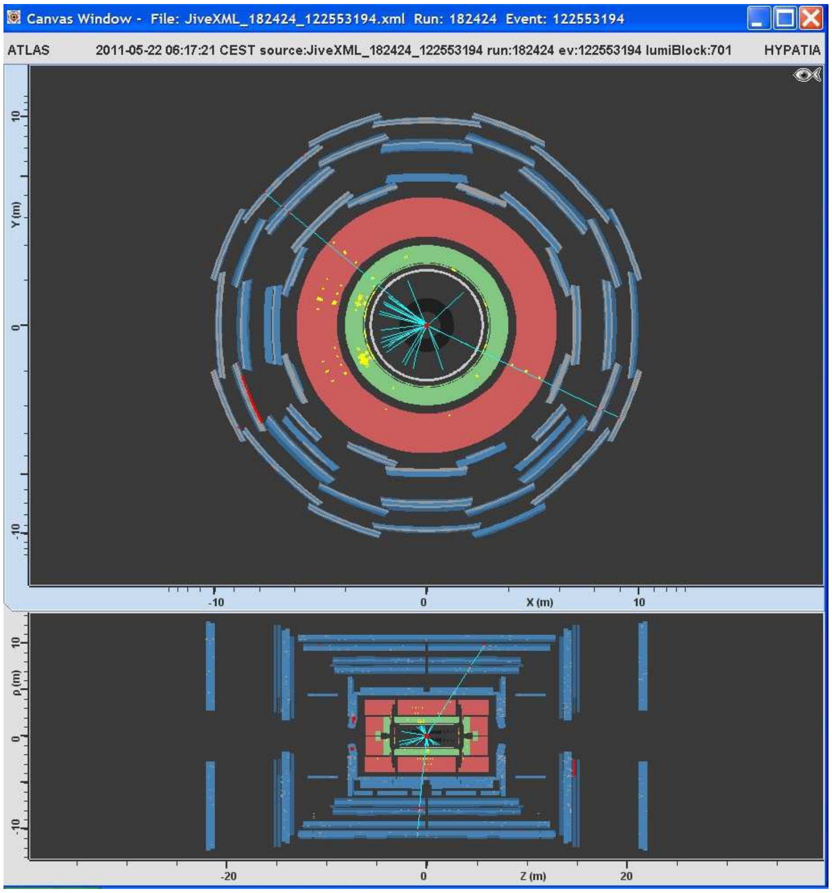

Figure 5.21: RunNumber 182424, EventNumber 122553194 : Invariant Mass 881 GeV

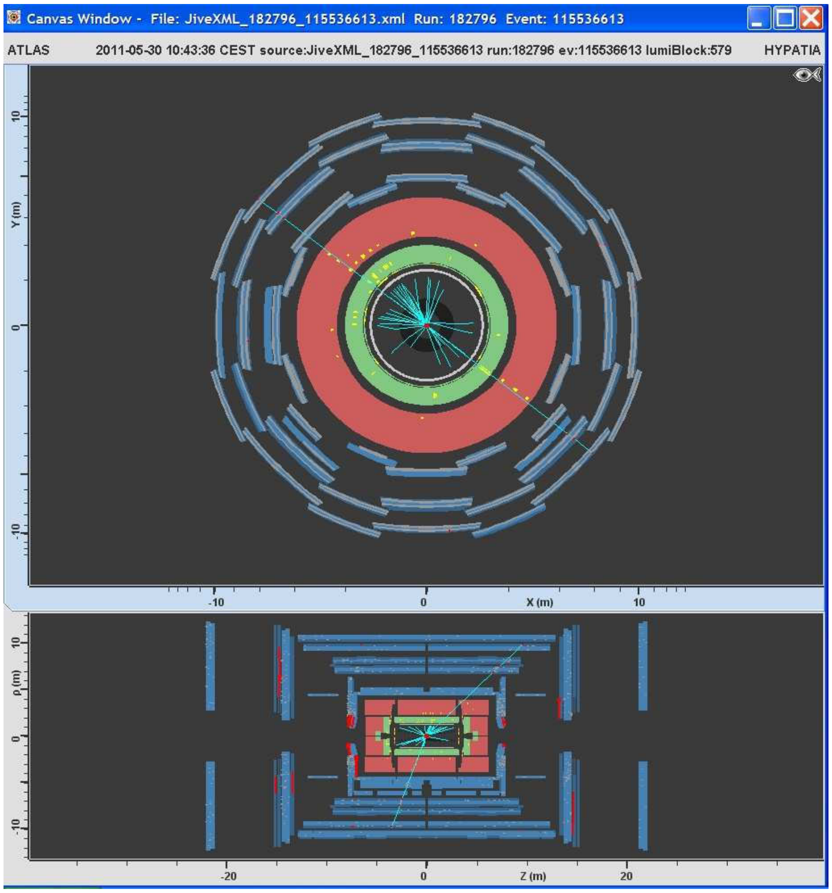

Figure 5.22: RunNumber 182796, EventNumber 115536613 8 : Invariant Mass 819 GeV

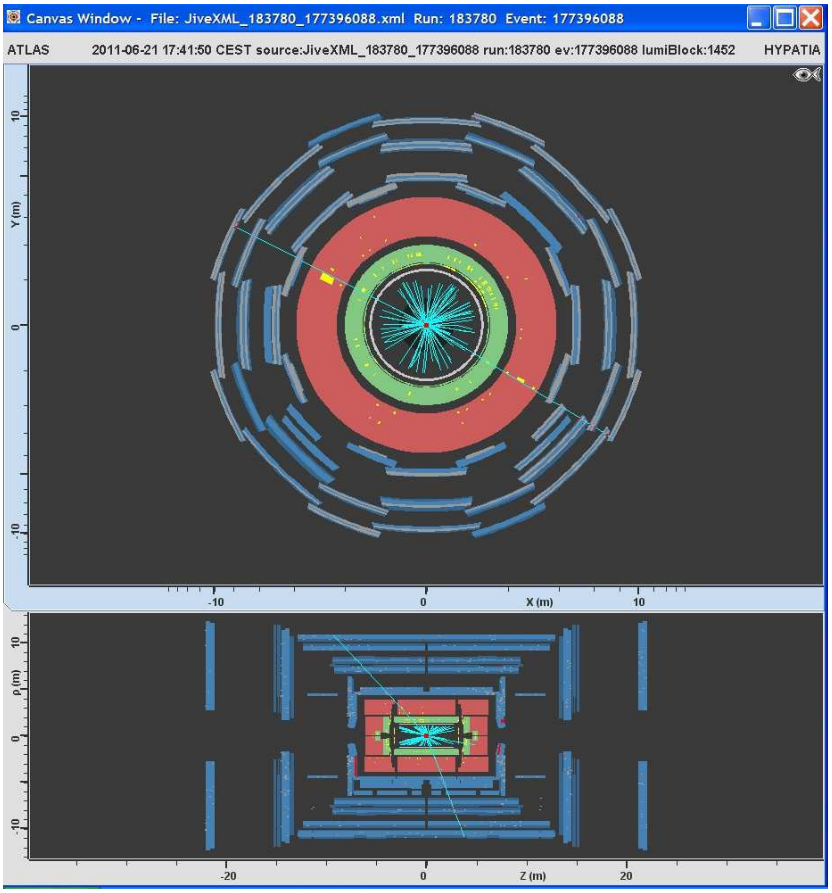

Canvas Window - File: JiveXML_183780_177396088.xml Run: 183780 Event: 177396088

ATLAS 2011-06-21 17:41:50 CEST source:JiveXML_183780_177396088 run:183780 ev:177396088 lumiBlock:1452 HYPATIA

Figure 5.23: RunNumber 183780, EventNumber 177396088 : Invariant Mass 777 GeV

Dimuon Mass (GeV)	$P_{T,1}$ (GeV)	$P_{T,2}$ (GeV)	η_1	η_2	ϕ_1	ϕ_2	MET
949	+533	-409	0.365	0.723	3.006	-0.116	138
881	+475	-374	-0.083	0.564	-0.453	2.46	16
819	+363	-328	-0.342	0.866	-0.662	2.489	34
777	-485	+308	-0.778	0.338	2.658	-0.551	180

Table 5.10: The four highest mass events of 2011 ATLAS data

In Table 5.11, we present the additional masses' characteristics that were used in the 2011 analysis and in Figure 5.24, the produced templates per unit area are presented (after passing the 2011 analysis selection criteria).

Regarding the uncertainties that are used in the limit setting procedure, these are identical to the ones of 2010.

In Figure 5.25, the final limits on the Z' existence using the 2011 ATLAS data can be seen. It is proved that a Z' boson can be excluded up to a mass of 1.678 TeV. The corresponding cross-section is $7.3\,\mathrm{fb}^{-1}$.

For the expected limits, the corresponding values were equal to 1.676 TeV and $7.4\,\mathrm{fb}^{-1}$.

Mass (GeV)	LO cross-section (pb)	k-factor	Pythia width (Gev)
1600	0.010	0.965	50.23
1700	0.0072	0.941	53.43
1800	0.0050	0.915	56.08
1900	0.0036	0.887	59.83
2000	0.0025	0.860	63.03

Table 5.11: LO xs, k-factors and widths for the additional Z' templates of 2011

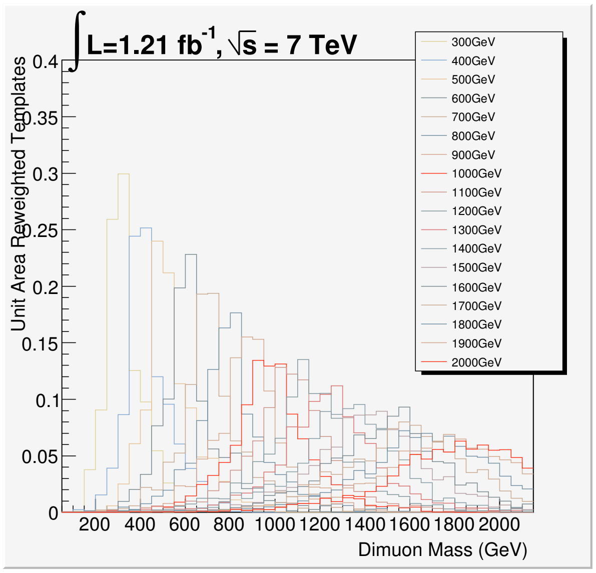

Figure 5.24: The Z' templates used in the 2011 analysis

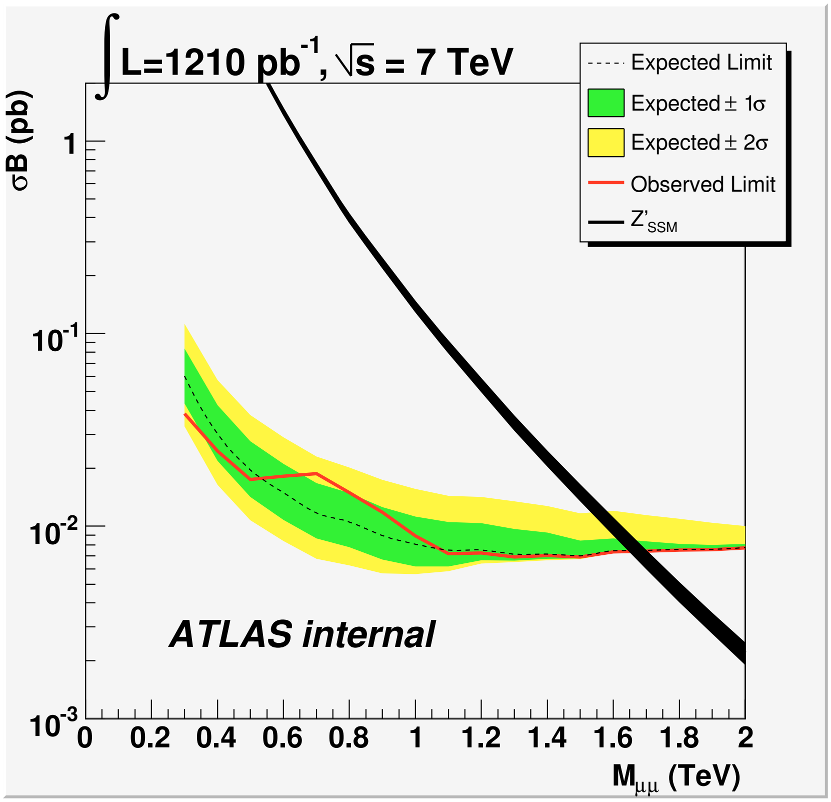

Figure 5.25: Expected and observed 95% C.L. limits on σB and expected σB for Z'

Chapter 6

Summary

In this thesis, a search for a new, heavy, neutral gauge boson, namely the Z' boson with Standard Model like couplings, is presented.

The study has been performed using the LHC p-p collision data, collected with the ATLAS experiment, at a center of mass energy of $\sqrt{s} = 7\,\text{TeV}$, covering two different time periods: March-November 2010 and March-June 2011. The total integrated luminosity for these periods was of the order of $42\,\text{pb}^{-1}$ and $1.2\,\text{fb}^{-1}$ correspondingly.

After a brief theoretical introduction of the models predicting such a new boson and a description of its properties and characteristics, we essentially proceeded to the analysis, by, first of all, presenting analytically the methods of reconstruction of the muon software and the system performance and giving all the details regarding the study methods that were used in this work (reconstruction algorithms, software tools, data quality control, etc.).

The Z' boson is expected to appear as a resonance in the high mass region of the Drell-Yan process ($pp \to \ell^+\ell^-$, where ℓ = e, μ and τ). The production mechanism chosen indicates that Z', in analogy with the Standard Model Z boson, is electrically neutral, colorless and self-adjoint.

In the present study, we focused on the muonic decay of the new boson ($Z' \to \mu^+\mu^-$), therefore the final state will be characterized by the presence of two, oppositely charged muons. Any Standard Model procedure with the same signature can be a possible background source for the Z' signal.

The dominant and irreducible background is the Drell-Yan process of the Standard Model into muons $Z/\gamma^* \rightarrow \mu\mu$. Obviously, we are mainly interested in the high mass region, where the rapid decrease of the cross-section leads to small statistics. For this reason, apart from an inclusive sample, several binned samples, generated in different large mass bins, were used, in order to enlarge the statistics.

Other procedures that can also constitute background processes to our signal and were examined are the $t\bar{t} \rightarrow \mu^+\mu^-$, W + jets (where a jet may be identified incorrectly as a muon), the di-boson production (WW, WZ and ZZ) and finally the QCD processes $b\bar{b} \rightarrow \mu^+\mu^-$ and $c\bar{c} \rightarrow \mu^+\mu^-$. The contribution of cosmic particles as another possible source of background is also discussed.

The first element that was examined in our analysis were the pile-up conditions. Since we can not know in advance the content of pile-up events in our data, so as to appropriately adjust our Monte Carlo, this has to be estimated a posteriori. The method adopted was to measure the number of primary vertices in the real data and apply a weight on every Monte Carlo event versus its number of vertices "n", that is extracted by the ratio of the total number of the Data events with n vertices over the total number of Monte Carlo events with n vertices:

- $MC_{p.u.W.}(n)$ = Data events with n vrts. / MC events with n vrts.

Not the whole amount of each data sample are appropriate for physics' studies. Before anything else, we had to choose, for each data sample, this part that was taken with all the sub-detectors up on High Voltage. This was done by applying the Good Run Lists (GRLs), a dedicated list that determines the "good" Luminosity Blocks for every data sample.

After that, we proceeded to apply the appropriate selection criteria of our analysis, on both data and Monte Carlo samples. These are:

1. Trigger: For the data, we have used different muon triggers, with a muon momentum that increased in time, due to the constantly increasing luminosity (P_T varied from 10 to 13 GeV). For the Monte Carlo, we kept one common trigger, of 10 GeV P_T

2. Primary Vertex: In order to ensure that the particular events that we tested are, indeed, the product of a real collision, we requested the presence of one Primary Vertex, displaced with respect to the interaction point 20 cm maximum, and with at least three different tracks associated to it
3. Two Combined Muons: We requested at least two muons with both Inner Detector and Muon Spectrometer information
4. P_T: We only kept muons with a transverse momentum above 25 GeV
5. η: In order for the muon to fall within the 2010 trigger acceptance, we restricted the muon pseudorapidity up to 2.4
6. Inner Detector hits: In order to ensure the quality of the track reconstruction, we requested a minimum number of hits of the muon in the several parts of the Tracker
7. Muon Spectrometer hits: Ensured quality of the reconstruction in the Spectrometer
8. Impact Parameters: We used upper limits on the impact parameters of the muons (z_0 and d_0), to reject muons coming from cosmic rays -which are expected to appear displaced from the Primary Vertex
9. Isolation: We imposed a limit on the activity (i.e., additional tracks) around the muons, to reject those within jets
10. Opposite Charge: We requested that the two most energetic muons of each event should possess opposite charges
11. Dimuon Mass: Finally, we examined those events that had a dimuon mass greater than $70\,\mathrm{GeV}/c^2$

The appropriate normalization of the background processes to the data luminosity is performed via their cross-section. In contrast to the less important backgrounds, where the higher-order cross-sections were used as a single number applied to the whole distribution, for the Drell-Yan background a more dedicated study was done. Emphasis was given to the estimation of a k-factor (that includes both QCD and Electroweak correction) which should vary with mass. The same study was performed for the Z' signal as well. Assuming that all colorless final states are characterized by the same QCD radiation in their initial state, we can apply the same QCD correction as in the Drell-Yan case. Nevertheless, because the EW ones are model dependent, we ignored them in this case.

Part of the study was devoted specifically to QCD background processes, $b\bar{b}$ and $c\bar{c}$. This background has little contribution to the analysis; however, due to the large uncertainty on its cross-section, it has to be estimated based on the data distribution. This is done by adjusting the distribution of the non-isolated muons (which is a characteristic of these processes) of the Monte Carlo to this of the data. The final QCD distribution with the isolation requirement included (i.e., after the whole selection) was extracted from the non-isolated one with the use of an appropriate scale factor.

Another dedicated study was performed on the background from cosmics. Since a cosmic muon can be reconstructed as two different ones, characterized also by high momentum, it can be an artificial source of background. The impact parameter requirement does remove the vast majority of these muons. The study has shown that the remaining amount is negligible.

After the whole selection was applied, the dimuon mass distributions for the data and the Monte Carlo samples were used to search for excesses that could be an indication of the Z' presence. The data showed no evidence of signal and, thus, limits were set on the σB of Z', in a mass range from 300 GeV to 1.5 TeV. The limits are evaluated using a likelihood analysis that is taking the shape of the mass into account. With the 2010 ATLAS pp data, the limit on the Z' was measured equal to $867\,\mathrm{GeV}/c^2$. This is equivalent to a σB exclusion of 0.278 pb.

A very much alike analysis was performed on the 2011 data, with only minor changes implemented. In this case, too, the data was in agreement with the Standard Model expectations and no important excess was presented. The 2011 data extended the mass limit on the Z' σB to the level of 1.678 TeV. The excluded cross-section this time was equal to 7.3 fb.

The search on the Z' existence continues from the ATLAS exotics group. The total amount of data taken in 2011 ($\sim 5\,\mathrm{fb}^{-1}$) is studied and, since no excess is yet discovered, the limits are expected to reach the level of 2 TeV. A new publication is anticipated soon.

Bibliography

[1] G. Altarelli, The Standard Model of Particle Physics, arXiv:hep-ph/0510281 v1 - 21 Oct 2005

[2] G.t Hooft, M.Veltman, Regularization and renormalization of gauge fields, Nucl.Phys. B 44 (1972)

[3] James Wells, Lectures on Higgs Boson Physics in the Standard Model and Beyond, arXiv:0909.4541

[4] O. E. Casas B., A. M. Raba P. and N. Poveda T., An approach to the formalism of the Standard Model of Particle Physics, arXiv:1004.3331v2 [physics.gen-ph] - 3 May 2010

[5] F. Halzen and A. D. Martin, Quarks and Leptons

[6] C. Burgess and G. Moore, The Standard Model, A Primer, 2007 (ISBN 275 0521860369)

[7] S.Raby, Grand Unified Theories, arXiv:hep-ph/0608183v1, 2006

[8] Hewett, J. L., and T. G. Rizzo, 1989, Phys. Rept. 183

[9] Langacker, P., and M.-x. Luo, 1992, Phys. Rev. D45, 278.

[10] F. Buccella, G. Mangano, O. Pisanti, and L. Rosa, Phys. Atom. Nucl. 61 (1998)

[11] R. Mohapatra, Unification and Supersymmetry: The Frontiers of Quark-Lepton Physics (Springer, Berlin)

[12] G. Polesello and M. Prata, Eur. Phys. J. C32S2 (2003)

[13] F. Aversa, S. Bellucci, M. Greco, and P. Chiappetta, Phys. Lett. B254 (1991)

[14] D0 Collaboration, V. M. Abazov et al., Phys. Rev. Lett. 100 (2008)

[15] T.Rizzo, J.Wells, Phys.Rev. D61, 016007, arXiv:hep-ph/9906234

[16] J.Lykken, Z' Bosons and Supersymmetry, arXiv:hep-ph/9610218v3, 1996

[17] P. Langacker, The Physics of Heavy Z' Gauge Bosons, arXiv:0801.1345v3 [hep-ph] 30 Nov 2009

[18] F. Del Aguila, The Physics of Z' bosons, arXiv:hep-ph/9404323v1 22 Apr 1994

[19] OPAL Collaboration, Tests of the standard model and constraints on new physics from measurements of fermion pair production at 189 GeV to 209 GeV at LEP, arXiv:hep-ex/0309053v1 17 Sep 2003

[20] T. Rizzo, Indirect Searches for Z'-like Resonances at the LHC, arXiv:0904.2534v5 [hep-ph] 3 Aug 2009

[21] V. M. Abazov et al. (D0 Collaboration), Phys. Lett. B695, 88 (2011).

[22] T. Aaltonen et al. (CDF Collaboration), Phys.Rev.Lett.106, 121801 (2011)

[23] The CMS Collaboration, Search for Resonances in the Dilepton Mass Distribution in pp Collisions at $\sqrt{s} = 7TeV$, arXiv:1103.0981v2 [hep-ex] 7 Mar 2011

[24] CMS Physics Technical Design Report, Volume I: Detector Performance and Software, CERN-LHCC-2006-001 ; CMS-TDR-008-1, 2006

[25] ALICE : Technical proposal for a Large Ion collider Experiment at the CERN LHC, CERN-LHCC-95-71 ; LHCC-P-3,1995

[26] The LHCb collaboration, LHCb Technical Proposal, CERN LHCC 98-4, LHCC/P4, 20-2-1998

[27] The TOTEM Collaboration et al 2008 JINST 3 S08007

[28] The LHCf Collaboration et al 2008 JINST 3 S08006

[29] ATLAS collaboration, ATLAS Detector and Physics Performance Technical Design Report Vol I, CERN-LHCC-99-14, 1999

[30] ATLAS collaboration, ATLAS Detector and Physics Performance Technical Design Report Vol II, CERN-LHCC-99-15, 1999

[31] ATLAS collaboration, Inner Detector Technical Design Report Vol I, CERN-LHCC-97-16, 1997

[32] ATLAS collaboration, Inner Detector Technical Design Report Vol II, CERN-LHCC-97-17, 1997

[33] Pixel Detector Technical Design Report ATLAS TDR 11, CERN/LHCC 98-13

[34] ATLAS collaboration, Liquid Argon Technical Design Report, CERN-LHCC-96-41, 1996

[35] ATLAS collaboration, Tile Calorimeter Technical Design Report, CERN-LHCC-96-12, 1996

[36] ATLAS Hadronic End-cap Calorimeter Group, JINST 2, P05005 (2007)

[37] A. Artamonov et al. The ATLAS Forward Calorimeter, JINST 3, 2008

[38] ATLAS collaboration, Magnet System Technical Design Report, CERN/LHCC/98-14, 1998

[39] ATLAS Collaboration, ATLAS central solenoid : Technical Design Report, CERN-LHCC-97-021

[40] ATLAS Level-1 Trigger Group, Level-1 Trigger Technical Design Report, ATLAS TDR12, 24 June 1998

[41] ATLAS HLT/DAQ/DCS Group, ATLAS High-Level Trigger, Data Acquisition and Controls, ATLAS TDR-016, 30 June 2003)

[42] ATLAS collaboration, Muon Spectrometer Technical Design Report, CERN-LHCC-97-22, 1997

[43] J.Barriere et al, The alignment system of the ATLAS barrel muon spectrometer, ATL-MUON-PUB-2008-007, 2008

[44] C. Amelung et al, The Optical Alignment System of the ATLAS Muon Spectrometer Endcaps, ATL-MUON-PUB-2008-003, 2008

[45] The ATLAS collaboration, Expected Performance of the ATLAS Experiment: Detector, Trigger and Physics, CERN-OPEN-2008-020, December 2008

[46] S. Hassani et al., A muon identification and combined reconstruction procedure for the ATLAS detector at the LHC using the (MUONBOY, STACO, MuTag) reconstruction packages, Nuclear Instruments and Methods in Physics Research A 572 (2007) 7779

[47] D. Adams et al.,Track Reconstruction in the ATLAS Muon Spectrometer with MOORE, ATL-COM-MUON-2003-012, 2 October 2003

[48] K. Nikolopoulos, D. Fassouliotis, C. Kourkoumelis, A. Poppleton, Event-by-Event Estimate of Muon Energy Loss in ATLAS, IEEE Trans. Nucl. Sci. 54, 2007

[49] CDF Collaboration, D.E. Acosta et al., Phys. Rev. Lett. 94 (2005) 091803

[50] D0 Collaboration, V.M. Abazov et al., Phys. Rev. D76 (2007) 012003.

[51] The ATLAS Collaboration, Search for high mass dilepton resonances in pp collisions at $\sqrt{s} = 7TeV$ with the ATLAS experiment, arXiv:1103.6218v1[hep-ph], 31 Mar 2011

[52] P. Calafiura, W. Lavrijsen, C. Leggett, M. Marino, D. Quarrie, The athena control framework in production, new developments and lessons learned, 2005

[53] T. Sjostrand, S. Mrenna, and P. Skands, PYTHIA 6.4 Physics and Manual, JHEP 05 (2006) 026

[54] A. Sherstnev and R. S. Thorne, Parton Distributions for LO Generators, Eur. Phys. J. C55 (2008) 553

[55] S. Frixione and B. Webber, Matching NLO QCD computations and parton shower simulations,JHEP 0206 (2002) 029.

[56] J. M. Butterworth, J. R. Forshaw, and M. H. Seymour, Multiparton interactions in photoproduction at HERA, Z. Phys. C72 (1996) 637646

[57] G. Corcella, I. Knowles, G. Marchesini, S. Moretti, K. Odagiri, P. Richardson, M. Seymour, and B. Webber, HERWIG 6.5 Release Note, arXiv:hep-ph/0210213

[58] P. M. Nadolsky et al., Implications of CTEQ global analysis for collider observables, Phys. Rev.622 D19 (2010)

[59] The ATLAS Collaboration, Muon momentum resolution from p-p collision data. ATLAS internal note: https://svnweb.cern.ch/trac/atlasgrp/browser/CombPerf/MuonPerf/Notes/2010-Autumn/MuonMomentumResolutionNote/perf.pdf

[60] T. Golling et al.,The ATLAS Data Quality Defect Database System,arXiv:1110.6119v1 [physics.ins-det] 27 Oct 2011

[61] R.Hamberg, W.L.van Neerven, and T.Matsuura, A Complete Calculation of the order $\alpha - s^2$ correction to the Drell-Yan K factor, Nucl.Phys.B3539(1991)

[62] A.D.Martina,W.J. Stirlingb, R.S. Thornec and G.Wattc, Parton distributions for the LHC, Eur.Phys.J.C63:189-285,2009, arXiv:0901.0002v3 [hep-ph]

[63] R. Blair et al., ATLAS Standard Model Cross Section recommendations for 7 TeV LHC running, https://svnweb.cern.ch/trac/atlasgrp/browser/Physics/StandardModel/xsectf/note/xsectf.pdf

[64] C. M. Carloni Calame, G. Montagna, O. Nicrosini, and A. 582 Vicini, Precision electroweak calculation of the production of a high transverse-momentum lepton pair at hadron colliders, JHEP 10 (2007) 109, arXiv:0710.1722[hep-ph]

[65] C. M. Carloni Calame, G. Montagna, O. Nicrosini, and A. Vicini, Precision electroweak calculation of the charged current Drell-Yan process, JHEP 0612 (2006) 016

[66] P. Golonka and Z. Was, PHOTOS Monte Carlo: a precision tool for QED corrections in Z and W decays, Eur. Phys. J. C 45 (2006)

[67] A. D. Martin, R. G. Roberts, W. J. Stirling, and R. S. Thorne, Parton distributions incorporating QED contributions, Eur. Phys. J. C39 (2005) 155161, arXiv:hep-ph/0411040

[68] M. L. Mangano, M. Moretti, F. Piccinini, R. Pittau, and A. D. Polosa, ALPGEN, a generator for 645 hard multiparton processes in hadronic collisions, JHEP 07 (2003) 001

[69] S. Frixione and B. Webber, Matching NLO QCD computations and parton shower simulations, JHEP 0206 (2002) 029.

[70] The ATLAS Collaboration,ATLAS Muon Momentum Resolution in the First Pass Reconstruction of the 2010 p-p Collision Data at$\sqrt{s} = 7TeV$, ATLAS-CONF-2011-046,March 22, 2011

[71] The ATLAS Collaboration,Luminosity Determination in pp Collisions at $\sqrt{s} = 7TeV$ Using the ATLAS Detector at the LHC, arXiv:1101.2185v1[hep-ph], 2011

[72] T. Junk, Confidence Level Computation for Combining Searches with Small Statistics, arXiv:hep-ex/9902006v1 5 Feb 1999

[73] C. M. Carloni Calame, G. Montagna, O. Nicrosini, and A. Vicini, Precision electroweak calculation of the charged current Drell-Yan process, JHEP 0612 (2006) 016

[74] TeV4LHC-Top and Electroweak Working Group Collaboration, C. E. Gerber et al., Tevatron-for-LHC Report: Top and Electroweak Physics, arXiv:0705.3251 [hep-ph]

[75] S. Dittmaier and M. Kramer, 1, Electroweak radiative corrections to W-boson production at hadron colliders, Phys. Rev. D65 (2002) 073007, arXiv:hep-ph/0109062.

[76] The ATLAS Collaboration, Search for dilepton resonances in pp collisions at $\sqrt{s}$ = 7 TeV with the ATLAS detector, arXiv:1108.1582v1, [hep-ex] 7 Aug 2011

[77] K. Sinervo, Signal Significance in Particle Physics, CDF/PUB/STATISTICS/PUBLIC/6031, 30 June 2002

[78] S.Bityukov, N. Krasnikov, A. Nikitenko, On the Combining Significances, arXiv:physics/0612178v3 [physics.data-an] 20 Dec 2006

[79] S.I. Bityukov, N.V. Krasnikov, Proc. of the Conference on: Advanced Statistical Techniques in Particle Physics, Eds M.R. Whalley and L. Lyons, IPPP/02/039,DCPT/02/78, Durham, UK, 2002; also, e-Print: hep-ph/0204426

[80] S.I. Bityukov, N.V. Krasnikov, Nucl.Instr.Meth. A452 (2000) 518

[81] H.Bu, J.Nielsen, Analytic Confidence Level Calculations using the Likelihood Ration and Fourier Transform, arXiv:physics/9906010 v1, 4 Jun 1999

[82] H.Hu, J.Nielsen, Analytic Confidence Calculations using the Likelihood Ratio and Fourier Transform, arXiv:physics/9906010 v1 4 Jun 1999

[83] A.Read, Optimal Statistical Analysis of Search Results based on the Likelihood Ration and its Applications to the Search for the MSM Higgs Boson at $\sqrt{s} = 161$ and 172 GeV, DELPHI note 97-158n PHYS 737 (1997)

[84] H.Sorensen, D.Jones, M. Heideman, C.Burrues, Real Valued Fast Fourier Transform Algoritmhs, IEEE Trans.Acoust, Speech, Signal Processing vol. ASSP-35, June 1987

Appendices

Appendix A

Significance Studies and Limits' setting

The interpretation of new particle search results always involves a confidence level calculation, which is a measure indicating how safe the extracted results are -i.e. they did not happen by chance.

In this type of studies, there are two basic hypotheses that have to be tested. The first one, which is called the "null hypothesis" or "background hypothesis" (symbolized with H0) is that the particle under investigation does not exist; only Standard Model background processes appear. The second hypothesis is the "test hypothesis" or "discovery hypothesis" (symbolized with H1): the particle under investigation does exist, so there will be a combination of signal plus Standard Model background procedures in our data.

Therefore, the observed data of an experiment (or even the simulation data) should be analyzed regarding its "signalness". Essentially, that is, it should be tested with which of the two cases the data are more compatible to.

A.1 Types of Errors

An obvious error that this kind of study can lead to, is to conclude that one of the above mentioned hypotheses is valid, while in reality the other one is. This error can be done in two ways:

- Type I error: We conclude that the particle under investigation exists, when it actually does not; we reject the null hypothesis when it is in fact correct.
- Type II error: The particle under investigation does indeed exist, but we fail to prove it; we accept the null hypothesis when it is actually wrong.

So, we have to find a way to estimate how safe the conclusion of such a study is, in terms of the discovery or absence of the particle. This is where the measure of the "statistical significance" enters. It indicates with how much confidence one can claim to have discovered the new particle. More specifically, the significance level gives the probability to reject the null hypothesis when it is actually true (probability of Type I error).

Significance levels show how likely a result is due to chance. It is customary to use the level of 0.95. This means that the result we have come to has a 95% chance of being true[1]. However, the value mainly used is the inverse one: the probability of the error, which, in this case, would be 0.05 or 5%. This means that the result has a 5% chance of being false.

The error probability $p < 0.05$ in statistics determines a successful outcome to an experiment.

Clearly, the purpose of any study concerning the existence of a theoretical predicted particle is precisely to minimize this error probability -at least, to the level of 5%.

A.2 Significance and p-value

Lets now return to the two alternatives hypotheses H0 and H1 and suppose we have a measurement whose value is a test statistic X. X is a random variable and can provide some discrimination between these two hypotheses.

For example, there is a "critical region", W, such that H1 is valid if $X \in W$ and H0 is valid otherwise [77]. Let now $f_0(X)$ and $f_1(X)$ be the probability distribution functions for X, associated with the two hypotheses. This function describes all values

---

[1] The use of the 95% level is due to the great pioneer of significance testing, R.A.Fisher.

that X can have, under each hypothesis, and the probability that a specific value of the X variable is within this set.

Obviously, the probability of making a Type I error (i.e., reject H0, when it is actually true) is equivalent with the (non-zero) probability that the assumption $X \in W$ has, when we calculate $f_0(X)$ function. This is equal to:

$$\int_{X \in W} f_0(X) dX = \alpha \tag{A.1}$$

This probability α measures the ability of a test to avoid Type I errors and is exactly the definition of the "significance": the probability of claiming discovery of the particle under investigation, when it actually does not exist.

The corresponding probability for a Type II error (false rejection of the existence of the particle) is given by a similar expression:

$$\int_{X \notin W} f_1(X) dX = \beta \tag{A.2}$$

It is straightforward that the task of a statistic test is to choose the test statistic X and the region W in such a way that α and β are as small as possible (see Figure A.1) [2]

Suppose now that an experiment makes a measurement of the test statistic X, say X_0. The observations of X can be categorized, depending if they are more or less consistent with H0.

Consider, for example, the great mass of the Z' boson: a resonance in high masses is "less consistent" with the H0 hypothesis; it is less likely to be observed if Z' does not exist. A measure of the inconsistency of the observed value X0 with the hypothesis H0 is then the probability:

$$\int_{X > X_0} f_0(X) dX \tag{A.3}$$

This is identical to the definition of the significance and is equivalent with Equation A.1. Of course, in order for this equivalence to be valid, the critical region W should be: $W = [X | X > X_0]$.

---

[2] Figure taken from Reference [77]

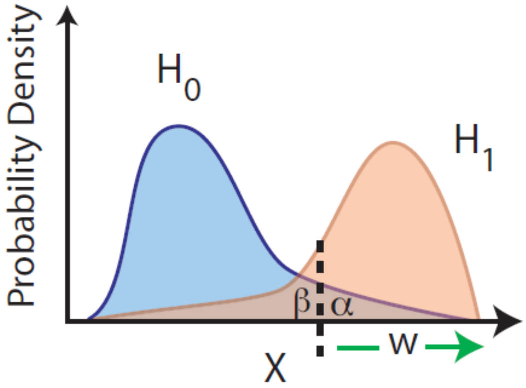

Figure A.1: A schematic of the hypothesis test

Equation A.3 gives the probability of X to be greater than X_0 (which is the rejection value for H0), despite the fact that H0 is valid. In the previous example of the Z' boson resonance, the above form gives the probability to observe a high-mass resonance if the boson does not exist (i.e., due to a fluctuation of the Standard Model background).

The above form is known as the "p-value" of the observation. For a given measurement and a specific hypothesis, the p-value depends on the measurement we make and the probability density for the hypothesis under investigation. It actually provides information on how consistent a measurement is with a particular hypothesis. A very small p-value is used to support the inference that the specific hypothesis should be rejected.

A.3 Significance estimation methods

There are several ways of estimating the significance for an experiment and several test statistics X that can be chosen to work with.

In analyses like the present one, where the objective is the existence of a new particle, we are mainly working with the excess of the observed or expected events of the new signal above the background ones in a certain mass region. First of all, we should distinguish the significance in two classes [78]:

(a) the "internal significance" $\mathcal{S}$ of an experiment is extracted based on two parameters: the expected number of the signal events N_s and the expected number of the background events N_b for a given experiment. It is a way of estimating the potential of a particular discovery in a certain experiment, before it is performed [79]

(b) the "observed significance" $\widehat{S}$ is based on the observed number of events $\widehat{N}_{obs}$ (i.e., the number of events that we record in the mass region in interest, after the experiment data is taken) and the expected number of events of the background N_b [80]

Obviously, the estimation of the observed significance is based on the knowledge of the internal one and cannot be performed otherwise. So, by using the expected number of signal and background events, according to our simulated data, we extract the expected internal significance (e.g. for a certain center-of-mass energy) in order to measure the observed significance, once the real data arrives.

What we usually do is to construct an expected experiment estimator distribution, against which the observed experiment's estimator (that is, the real data taken) will be later compared [81]; we construct a variable which quantifies the "signalness" of the simulated experiment. In other words, the estimator helps to characterize the results as to whether they are compatible with the H0 or the H1 hypothesis.

As mentioned above, the method followed consists of selecting an appropriate mass region (in our case, the expected Z' resonance region, depending on each particular simulated mass sample that we examine) and the number of events of expected signal and background are recorded there and used to give an measurement of the internal significance. In the following, we will describe several different methods for the significance estimation.

A.3.1 Number Counting

The most simple method we can use for the significance estimation is the "number counting" method[45].

Here we are only interested in the expected number of events for the signal and the background. With the use of Poisson statistics, we can estimate the probability that background fluctuations produce a signal-like result, according to some estimator, e.g. the likelihood ratio.

A.3.2 Shape analysis

The "shape analysis" approach [45] involves a detailed knowledge of the expected spectrum of the signal and the background, in terms of some observable (in our case, the invariant mass distribution).

The data is fitted or compared to the two hypotheses H0 and H1. The input signal and background shapes are given to the fitting algorithms either as histograms or as functions. For each of the models, a likelihood distribution is computed and the logarithm of the ratio of the two likelihoods (LLR) is estimated and used to compute the confidence levels.

We can use either $CL_b = CL_{H0}$ alone or $CL_S = CL_{H1}/CL_{H0}$ to estimate the significance, according to:

$$S = \sqrt{2} \times Erf^{-1}(1 - CL_b) \tag{A.4}$$

or

$$S = \sqrt{2} \times Erf^{-1}(1 - \frac{1}{CL_S}) \tag{A.5}$$

In the above equations, the term Erf^{-1} is the inverse of the error function:

$$Erf(x) = \frac{2}{\sqrt{\pi}} \int_0^x e^{-t^2} dt \tag{A.6}$$

In order to claim a 5σ significance, we should have: $1 - CL_b < 2.87 \times 10^{-7}$.

The shape analysis method can improve the sensitivity of the search, compared to the number counting method.

We can compute the LLR, either with the generation of pseudoexperiments or by using the Fast Fourier Transform (FFT) method. Those alternatives are described in the following paragraphs.

A.3.2.1 Monte Carlo Pseudoexperiments

The pseudoexperiments are based on the Monte Carlo distributions and are divided into the "background-only" experiments (BO), containing only background contributions, and the "signal-plus-background" experiments (SpB) having both the signal and the background contribution.

The signal significance can be estimated from the log-likelihood ratios lnQ_{BO} and lnQ_{SpB}, defined as:

$$lnQ = (N_S + N_B) ln\frac{N_S + N_B}{N_B} - N_S \tag{A.7}$$

The signal significance is obtained from the probability of a Type-II error, defined by the fraction of BO pseudoexperiments which have a log-likelihood ratio lnQ_{BO} larger than the median of the lnQ_{SpB} distribution. The probability of a Type-I error, i.e. the number of SpB pseudoexperiments which fall below the median of the lnQ_{BO} distribution, is used to determine the 95% CL limits.

A.3.2.2 Fast Fourier Transform

The pseudoexperiment method, described in the previous paragraph, is obviously time consuming. Another method was proposed, in order to bypass this problem, which help us estimate the significance by making use of Fast Fourier Transforms.

The Fourier transform moves a data sample from the time domain to the frequency domain. This allows a random sample to be broken into its major frequencies.

Consider a continuous function $f(x)$. The (continuous) Fourier transform is defined as[3]:

$$f(v) = \mathcal{F}_t [f(t)](v) = \int_{-\infty}^{+\infty} f(t) e^{-2\pi i v t} dt \tag{A.8}$$

For a discrete function $f(t_k)$, Equation A.8 can be generalized, to give the discrete

---

[3] http://mathworld.wolfram.com/

Fourier trasnform:

$$F_n = \sum_{k=0}^{N-1} f_k e^{-\frac{2\pi i n k}{N}} \tag{A.9}$$

The inverse transform is then:

$$f_k = \frac{1}{N} \sum_{n=0}^{N-1} F_n e^{\frac{2\pi i n k}{N}} \tag{A.10}$$

A.3.2.3 Description of the FFT method

A analytical description of the method is presented in Reference [82]. We give a brief outline in this paragraph.

The "Fast Fourier Transform" method, for the estimation of the significance, makes use of the likelihood ratio estimator. This is the ratio of the probabilities of observing an event (in our case, a high mass resonance), under the two search hypotheses (H0 and H1). For a single experiment, we have:

$$E = C \cdot \frac{\mathcal{L}_{s+b}}{\mathcal{L}_b} \tag{A.11}$$

In the above form, $\mathcal{L}_{s+b}$ is the probability density function for H1 hypothesis (signal+background) and $\mathcal{L}_b$ the corresponding one for H0 (background only).

The constant factor C appears in each event's estimator, so it cannot affect the "signalness" of an event. Therefore we choose $C = e^s$

In studies like the present one, we can choose the discriminant variable to be the mass m of a high mass resonance (i.e., the mass of the new particle under investigation). The signal and the background will have different probability density functions of the resonance mass, namely $f_s(m)$ and $f_b(m)$. Therefore, the estimator E, taking into account the event weighting coming from the discriminant variables, will be:

$$E = e^s \frac{P_{s+b}}{P_b} = e_s \frac{e^{-(s+b)}\left[s f_s(m) + b f_b(m)\right]}{e^{-b}\left[f_b(m)\right]} \tag{A.12}$$

More details about the advantages of the likelihood ratio estimator usage in the search of new particles can be found in [83].

The likelihood ratio estimator is a multiplicative estimator. This means that the estimator for an ensemble of events is formed by multiplying the individual event estimators.

For an experiment with 0 events, the calculation of the estimator is simple:

$$E = e^{-0}\frac{e^{-(0+0)}}{e^{-0}} = 1 \tag{A.13}$$

If we define F=lnE, for the 0 events experiment it is F=0 and for the probability density function of F, we have:

$$\rho_0\left(F\right) = \delta\left(F\right) \tag{A.14}$$

We consider now the case of an experiment with exactly one event. For example, a resonance at mass m_1. It is straightforward that:

$$E_1 = e_s\frac{e^{-(s+b)}\left[sf_s\left(m_1\right) + bf_b\left(m_1\right)\right]}{e^{-b}\left[f_b\left(m_1\right)\right]} = \frac{sf_s\left(m_1\right) + bf_b\left(m_1\right)}{f_b\left(m_1\right)} \tag{A.15}$$

And of course:

$$F_1 = lnE_1 = ln\left(\frac{sf_s\left(m_1\right) + bf_b\left(m_1\right)}{f_b\left(m_1\right)}\right) \tag{A.16}$$

Here, the probability density function will be defined as $\rho_1\left(F\right)$.

For the two events case, for example two reconstructed masses m_1 and m_2, equation A.16 becomes:

$$E_2 = \frac{sf_s\left(m_1\right) + bf_b\left(m_1\right)}{bf_b\left(m_1\right)}\frac{sf_s\left(m_2\right) + bf_b\left(m_2\right)}{bf_b\left(m_2\right)} \tag{A.17}$$

Therefore, the new estimator is the product of the two individual ones. For the F_2 variable, the two logarithms should be added:

$$F_2 = ln\frac{sf_s\left(m_1\right) + bf_b\left(m_1\right)}{f_b\left(m_1\right)} + ln\frac{sf_s\left(m_2\right) + bf_b\left(m_2\right)}{f_b\left(m_2\right)} \tag{A.18}$$

The corresponding probability density function is then given by:

$$\rho_2\left(F\right) = \int\int \rho_1\left(F_1\right)\rho_1\left(F_2\right)\delta\left(F - F_1 - F_2\right)dF_1dF_2 = \rho_1\left(F\right)\otimes\rho_1\left(F\right) \tag{A.19}$$

therefore, its equal to the convolution of $\rho_1(F)$ with itself.

The next step is to extend the above results to the general case of n events. The generalization is rather easy:

$$E_n = \prod_{i=1}^{n} \frac{sf_s(m_i) + bf_b(m_i)}{bf_b(m_i)} \tag{A.20}$$

and

$$F_n = \sum_{i=1}^{n} ln \frac{sf_s(m_i) + bf_b(m_i)}{bf_b(m_i)} \tag{A.21}$$

and, finally:

$$\rho_n(F) = \int ... \int \prod_{i=1}^{n} [\rho_i(F_i)\, dF_i]\, \delta\left(F - \sum_{i=1}^{n} F_i\right) = \underbrace{\rho_1(F) \otimes ... \otimes \rho_1(F)}_{\text{n times}} \tag{A.22}$$

Consider the functions $A(F)$, $B(F)$ and $C(F)$, for which:

$$A(F) = B(F) \otimes C(F) \tag{A.23}$$

The corresponding Fourier transforms of these functions satisfy the following relation:

$$\overline{A(G)} = \overline{B(G)}\, \overline{C(G)} \tag{A.24}$$

By comparing this equation with A.19, we get:

$$\overline{\rho_n(G)} = \left[\overline{\rho_1(G)}\right]^n \tag{A.25}$$

The convolution has therefore been expressed as a simple power.

For any practical computation, the analytic Fourier Transform can be approximated by a numerical Fourier Transform [FFT] [84].

The probability density function, for an experiment with s signal events and b background events, would be:

$$\rho_{s+b}(F) = \sum_{n=0}^{\infty} e^{-(s+b)} \frac{(s+b)^n}{n!} \rho_n(F) \tag{A.26}$$

In the above equation, n is the number of the observed events in the experiment under study. The Fourier Transform of the above probability density is given by:

$$\overline{\rho_{s+b}\left(G\right)} = \sum_{n=0}^{\infty} e^{-(s+b)} \frac{(s+b)^n}{n!} \overline{\rho_n\left(G\right)} = \sum_{n=0}^{\infty} e^{-(s+b)} \frac{(s+b)^n}{n!} \left[\overline{\rho_1\left(G\right)}\right]^n \tag{A.27}$$

The above equation can be written as:

$$\overline{\rho_{s+b}\left(G\right)} = e^{(s+b)\left[\overline{\rho_1(G)}-1\right]} \tag{A.28}$$

The function $\rho_{s+b}(F)$ can be extracted by the inverse transform.

Equation A.28 tells us that the probability density function for any (s+b) combination of the number of signal and background events can be calculated, if the probability density function of the estimator is known for a single event.

A.3.3 Combining results from several searches

Another advantage of the FFT method is the fact that it can be used to combine the results of several search channels (for example, get a common significance from $Z' \to e^+e^-$ and $Z' \to \mu^+\mu^-$ searches).

Since the likelihood ratio estimator is a multiplicative measure and assuming we have N different search channels, we can write for the (combined) probability density function:

$$\overline{\rho_{s+b}\left(G\right)} = \prod_{j=1}^{N} \overline{\rho^j_{s+b}(G)} = e^{\sum_{j=1}^{N}(s_j+b_j)\left[\overline{\rho^j_1(G)}-1\right]} \tag{A.29}$$

A.4 Limits

In studies such as the present one, when the object is the discovery of a theoretically predicted particle, another very important task is to also manage to reject it, if it indeed is absent. Therefore, in addition to the significance estimation, a similar study should be performed, to analyze the conditions required in order to positively state that the particle under investigation does not exist.

A.4.1 Limit setting method

The method we have used is described in [72].

In a search like the present one, we expect that both the number of signal and background events in the search region would be quite small and, thus, few candidate events are observed in the data. In such cases, Poisson statistics are required.

The method is based on the computation of Confidence Levels. More precisely, we have to compute the CL_{s+b}, which is the confidence level for the H1 hypothesis, and the CL_b for the H0 one, which can be evaluated by integrating the corresponding LLR distributions (via pseudoexperimets).

If LLR_{obs} is the observed test statistic (derived from the real data), then we have:

$$1 - CL_b = p(LLR \leq LLR_{obs}|H0) \tag{A.30}$$

and

$$CL_{s+b} = p(LLR \geq LLR_{obs}|H1) \tag{A.31}$$

Equation A.26 gives us the probability that the Standard Model background can give an fluctuation which simulates a “signal-like” outcome, like the one presented in the data (i.e., H0 is still valid). Correspondingly, CL_{s+b} is the probability that the (signal+background) case can lead to a (donwward) fluctuation. A small value of CL_{s+b} tells us that the outcome is inconsistent with the H1 hypothesis (i.e. limit setting).

So, we define the CL_s parameter, which is the ratio of the two confidence levels:

$$CL_s = \frac{CL_{s+b}}{CL_b} \tag{A.32}$$

The exlusion limit for the theoretical particle is determined, if we increase the particle's cross-section until we have:

$$CL_s = 1 - \alpha = 0.05 \tag{A.33}$$

Therefore $\alpha = 0.95$ ensures a 95% confidence level on the exclusion.

A.4.2 A priori sensitivity

We use Standard Model only pseudoexperiments (for the appropriate luminosity and conditions of the actual experiment). Then, for each pseudoexperiment, we perform a counting experiment, in order to extract the upper limit on the σB parameter at the 95% confidence level.

Appendix B

Muon Resolution Study

The purpose of this appendix is to investigate the so-called “Muon Spectrometer Hits” (MS Hits) set of cuts applied on muons in the dimuon analyses . The study on the cuts efficiency was based on the transverse momentum (P_T) resolution, between the P_T measurement of the Inner Detector and the one of the Muon Spectrometer of ATLAS.

We study the momentum resolution as a function of the muon transverse momentum and pseudorapidity, and compare the results with expectations from Monte Carlo simulation[1]. We compared the resolution in two cases: first, for muons with at least 3 hits in at least 3 layers of the Muon Spectrometer and second for those with at least 3 hits in only 2 layers.

The fractional resolution on the momentum measurement, $\sigma(p)/p$, is the result of different effects related to the amount of material that the muon traverses, the spatial resolution of the single track points and the degree of internal alignment of the two subsystems that are used in the measurement (Muon Spectrometer and Inner Detector).

The ATLAS Muon Spectrometer is designed to provide a uniform momentum resolution as a function of the pseudorapidity, which can be parameterized in the following way as a function of the P_T [59]:

$$\frac{\sigma(P)}{P} = \frac{P_2^{MS}}{P_T} \oplus P_0^{MS} \oplus P_1^{MS} \times P_T \tag{B.1}$$

where P_2^{MS} is the energy loss in the calorimetry material and P_0^{MS} and P_1^{MS} are the

---

[1] here, the Monte Carlo samples are before smearing

multiple scattering and intrinsic resolution terms respectively.

For the Inner Detector we expect a similar behaviour. The difference here is that the curvature measurement depends on the track length of the muon in the active material, which is reduced close to the end of the end of the TRT fiducial volume. In other words, we expect a uniform response in the central part of the detector and a rapidly worsening resolution beyond this region.

So, for the Inner Detector we have a parametrization of the resolution, described by two terms. First, for $|\eta| < 1.9$:

$$\frac{\sigma(P)}{P} = P_0^{ID} \oplus P_1^{ID} \times P_T \tag{B.2}$$

and, second, for $|\eta| > 1.9$:

$$\frac{\sigma(P)}{P} = P_0^{ID} \oplus P_1^{ID} \times P_T \times \frac{1}{tan^2(\theta)} \tag{B.3}$$

We divide the P_T distribution of the single muons in a total number of seven bins, presented in Table B.1.

P_T bin (GeV)	20-30	30-40	40-50	50-70	70-100	100-150	>150

Table B.1: The P_T bins where the muon resolution is calculated.

We also identify three regions in pseudorapidity for which we expect to have different resolutions both in the Inner Detector and the Muon Spectrometer:

- Barrel ($|\eta| < 1.05$)
- Intermediate Region ($1.05 < |\eta| < 2.0$)
- EndCups ($|\eta| > 2.0$)

The selection cuts we use for the (single) muons, for the barrel and the intermediate/endcup region are seen in Tables B.2 and B.3 correspondingly.

Muon Selection Cuts: Barrel Region ($\vert\eta\vert < 1.05$)
1) MDTBIS78Hits=MDTBEEHits=0 / RPCPhiHits>0 / 3 MDT hits in at least *3* layers
2) MDTBIS78Hits=MDTBEEHits=0 / RPCPhiHits>0 / 3 MDT hits in at least *2* layers

Table B.2: Selection Cuts for single muons, for Barrel region.

Muon Selection Cuts: Intermediate($1.05 < \vert\eta\vert < 2.0$) and EndCup ($\vert\eta\vert > 2.0$) regions
1) TGCPhiHits> 0 / (nCSCEtaHits>0 OR 3 MDT hits) in at least *3* layers
2) TGCPhiHits> 0 / (nCSCEtaHits>0 OR 3 MDT hits) in at least *2* layers

Table B.3: Selection Cuts of single muons, for Intermediate and EndCup regions.

For the above η regions and for each P_T bin of Table B.1, we estimate the ratio given by Equation B.4:

$$\rho = \frac{\frac{1}{P_{T_{MS}}} - \frac{1}{P_{T_{ID}}}}{\frac{1}{P_{T_{MS}}}} \tag{B.4}$$

We produced the ratio ρ, for the several P_T bins, in each one of the three control regions, first for the muons that have at least 3 layers of hits and then for those that have exactly 2 layers. We then perform a Gaussian fit on the several ρ distributions and extract the corresponding σ value.

Then, for each case (barrel, intermediate and endcaps for 3 and 2 layers hits requirements for data and background, i.e. twelve cases in total), we try to fit the distribution of the σ values with a fit, of the form:

$$f(P_T) = \sqrt{[0] * [0] + [1] * P_T * [1] * P_T} \tag{B.5}$$

which gives the $P_0 = [0]$ and $P_1 = [1]$ terms.

In order to avoid the incorporation of the cases with large energy loss in the calorimeter (i.e., the right region of the distribution, where the $P_{T_{ID}}$ value is sufficiently larger than $P_{T_{MS}}$), we perform, if possible, the fit within the limits $(-3\sigma, +2\sigma)$ from the mean of the distribution.

In several cases, mainly because of low statistis -so, in the distributions of the larger bins- the fit failed, therefore these particular cases cannot be included in our measurements.

For the fits that succeed, we keep the σ value, along with its error. For each of the two hit categories, and in all three control regions, we plot the distribution of the σ value versus the P_T bin. In Figures B.1, B.2 and B.3, we present the corresponding σ distributions for muons with (a) at least 3 hits and (b) exaclty 2 hits, for all three control regions.

In order now to estimate the correction factors between Monte Carlo and data, we extract the quadratic differences of the $P0$ and $P1$ terms for the data and the Z inclusive background sample, for each one of the η regions. The results are summed in Table B.4.

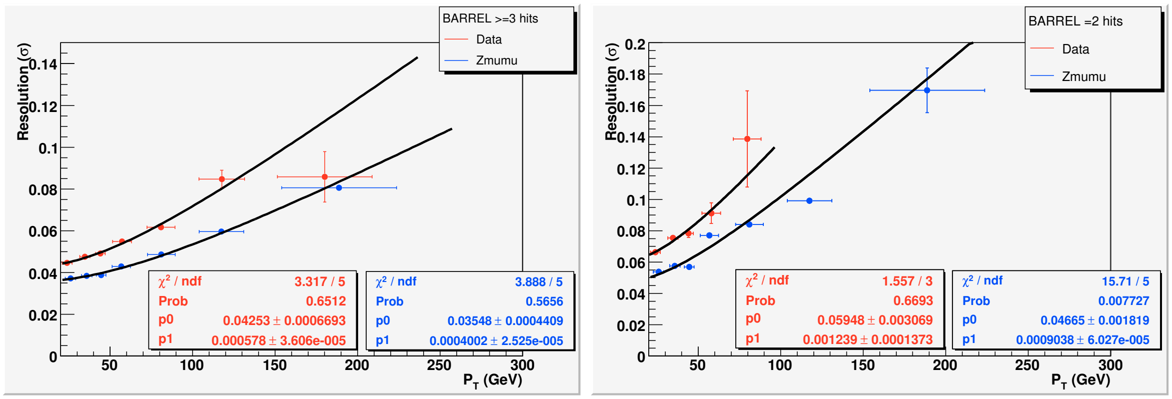

(a)

(b)

Figure B.1: *σ distribution per P_T bin: Barrel Muons with (a) at least 3 MS hits (b) exactly 2 MS hits (red: data, blue: $Z \rightarrow \mu\mu$ Monte Carlo)*

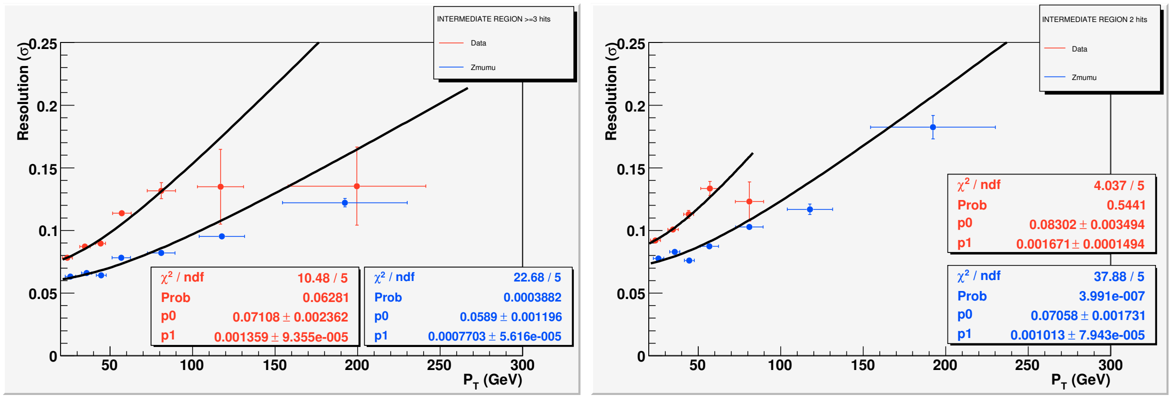

(a)

(b)

Figure B.2: *σ distribution per P_T bin: Intermediate region Muons with (a) at least 3 MS hits (b) exactly 2 MS hits (red: data, blue: $Z \rightarrow \mu\mu$ Monte Carlo)*

BARREL		3 layers			2 layers
P_0^{MC}	P_0^{Data}	Cor.Factor	P_0^{MC}	P_0^{Data}	Cor.Factor
0.03548	0.04253	0.0230±0.0008	0.04665	0.05948	0.036±0.003
P_1^{MC}	P_1^{Data}	Cor.Factor	P_1^{MC}	P_1^{Data}	Cor.Factor
0.00040	0.00058	0.42±0.04/TeV	0.0009	0.00124	0.85±0.15/TeV
INTERMEDIATE		3 layers			2 layers
P_0^{MC}	P_0^{Data}	Cor.Factor	P_0^{MC}	P_0^{Data}	Cor.Factor
0.0589	0.07108	0.0398±0.0026	0.07058	0.08302	0.0437±0.0039
P_1^{MC}	P_1^{Data}	Cor.Factor	P_1^{MC}	P_1^{Data}	Cor.Factor
0.00077	0.001359	1.1 ±0.1/TeV	0.00101	0.00167	1.3±0.16/TeV
END CAPS		3 layers			2 layers
P_0^{MC}	P_0^{Data}	Cor.Factor	P_0^{MC}	P_0^{Data}	Cor.Factor
0.06917	0.06854	0.0093±0.0066	0.08164	0.086	0.027±0.009
P_1^{MC}	P_1^{Data}	Cor.Factor	P_1^{MC}	P_1^{Data}	Cor.Factor
0.001096	0.001997	1.08 ±0.06/TeV	0.001424	0.002407	1.90 ±0.0001/TeV

Table B.4: Resolution Correction Factors for MC and data, versus η, for 3 and 2 layers requirements

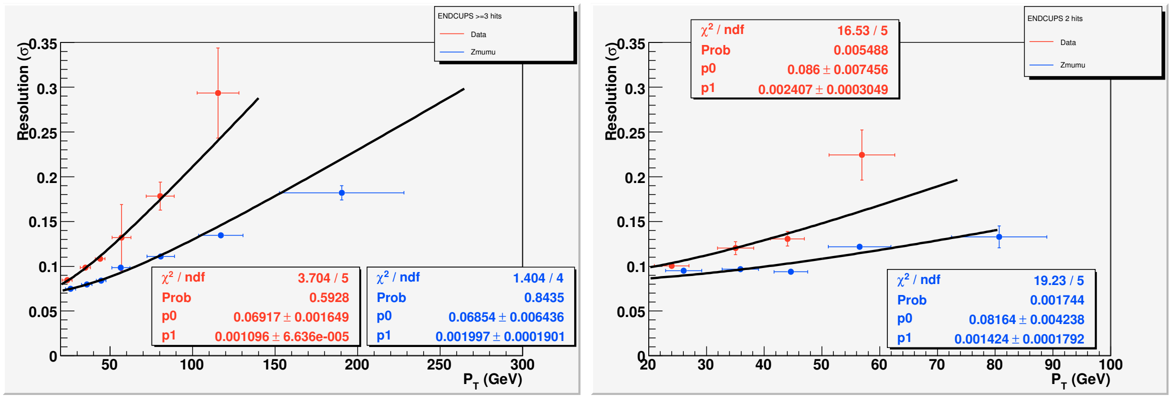

(a) (b)

Figure B.3: *σ distribution per P_T bin: End Cup Muons with (a) at least 3 MS hits (b) exactly 2 MS hits (red: data, blue: $Z \to \mu\mu$ Monte Carlo)*

From the above, we conclude that using the muons with hits in only 2 layers of the Spectrometer would worsen the resolution in all three cases (Barrel, Intermediate, End Cups).

Appendix C

Study on the Reconstruction Efficiency

The scope of this appendix is the comparison of the muon reconstruction efficiency, for the different reconstruction categories for the muons.

The key point is the presence of two muons coming from the Z boson decay ($Z \to \mu^+\mu^-$). The samples used for this study include the whole 2010 ATLAS data, a Pythia generated $Z \to \mu^+\mu^-$ sample and a $b\bar{b} \to \mu^+\mu^-$ one, that plays the role of the background to the Z decay. Other backgrounds (such as $c\bar{c} \to \mu^+\mu^-$) are not expected to have significant contribution in the overall efficiency.

As it was mentioned in Chapter 3, the main tool used to estimate the efficiency from data is the "Tag-And-Probe" method. We begin by searching for a muon ("tag" muon) which fulfills certain quality criteria and we try to associate it with an Inner Detector track ("probe" track), in the sense that they should form the Z boson invariant mass ($81.2\,\mathrm{GeV} < M_{tag-probe} < 101.2\,\mathrm{GeV}$) and, at the same time, have opposite electric charges. Then, the probe track should be matched with another muon of the event, in an appropriately selected $\eta - \phi$ cone.

The results extracted by the data should then be compared with those of the Monte Carlo simulation.

For this work, we evaluate the efficiency in three different ways, by keeping the characteristics of the Tag muon stable, but alternating the criteria for the muons that have to be matched to the probe track.

C.1 Reconstruction Details

The muon track, in general, is reconstructed using three layers of precision drift tube (MDT) chambers in the pseudorapidity range $\eta < 2$ and two layers of MDT chambers in combination with one layer of cathode strip chambers (CSC) at the entrance of the Muon Spectrometer for $2 \leq |\eta| < 2.7$[1].

In general, the Combined muons are the ones with the best characteristics, in terms of purity and reconstruction information. Still, they suffer from some drops in their reconstruction efficiency, in several regions of the Muon Spectrometer. The first of these regions lie at $\eta \sim 0$, where, due to the presence of several services for the other sub-detectors (namely, the Inner Detector and the Calorimeters) the Spectrometer is not fully equipped. The other one is at $\eta \sim 1.2$. There, due to staged end-cap chambers, the muon traverses only one chamber and, as a result, the efficiency decreases for the combined muons.

Another less efficient region is the one with $\phi \sim 1$ and $\phi \sim 2$, where the efficiency drops due to the additional material introduced by the feet, which support the barrel part of the detector.

C.1.1 Selection of Tag Muon

In the selection of the Tag muon, we follow in general the official Selection Criteria of the ATLAS exotics group, described in section 4.5, that will ensure the good quality of the candidates. Still, we loosen and alternate them a little ("minimum selection"), so as to enlarge the statistics.

First of all, we use a lower P_T cut of 20 GeV, in order not to loose a large amount of muon candidates, since we are now working with a much lighter boson, compared to the Z' case ($M_Z = 91.2\,\text{GeV}$). We also relax the Impact Parameter cut, by requesting only $z_0 < 10\,\text{mm}$, and we finally remove the Muon Spectrometer hits request, in order to have a compatible set of cuts for both the combined and the tagged muons, which

---

[1] 2.5 for Combined muons

Selection Cut	Description
Transverse Momentum	$P_T > 20\,\mathrm{GeV}$
No Muon Spectrometer Hits	
Distance from P.V.	$z_0 < 10\,\mathrm{mm}$
Impact Parameter Cuts	$z_0 < 1\,\mathrm{mm}$, $d_0 < 0.2\,\mathrm{mm}$

Table C.1: Differentiations of the Muon Selection Cuts for the Tag-And-Probe study, with respect to the main analysis. The MS hits requirement (described in section 4.5) will be applied in one muon category (see section C.1.3)

will be used later on in the method (the tagged muons can be seen only in the first layers of the Muon Spectrometer, thus a request for hits in all three layers would reject the majority of the candidates).

The differentiated cuts for this study are shown in Table C.1. All other cuts are the same, as in Table 4.8.

C.1.2 Selection and matching of Probe Track

The next step is to find the "Probe" track. Tracks that are good probe candidates should also satisfy certain selection criteria. Those can be seen in Table C.2.

Any tag that fulfills the criteria of Table C.2 is considered a "Probe". The Probe track is then compared with all the muons of the event (except, of course, the one with

Selection Cut	Description
Reconstruction Algorithm used	MUID
Pseudorapidity	$\|\eta\| < 2.5$ (Inner Detector coverage)
Transverse Momentum	$P_T > 20GeV$
Inner Detector Hits	>= 1 B-layer hit Pixel Hits >= 1 SCT Hits >= 6 Pixel Holes + SCT Holes <= 1 TRT: $\|\eta\| < 1.9$: (Hits+Outliers > 5),$\frac{\text{Outliers}}{\text{Hits+Outliers}} < 0.9$ $\|\eta\| >= 1.9$: If (Hits+Outliers > 5), then $\frac{\text{Outliers}}{\text{Hits+Outliers}} < 0.9$
Distance from P.V.	$z_0 < 10mm$
Isolation	$\frac{\sum_{dR<0.4} P_{T,\text{tracks}}}{P_{T,\text{probetrack}}} < 20\%$
Charge	$\text{Probe}_{\text{charge}} \cdot \text{Tag}_{\text{charge}} < 0)$
Tag-Probe mass close to Z	$81.2\,\text{GeV} < M_{\text{Tag}-\text{Probe}} < 101.2\,\text{GeV}$

Table C.2: Selection Cuts for the Probe Track which it forms the Z mass) and the efficiency is increased if at least one muon is found that can be associated to the track. The association is successful if the dR cone between the Probe and the muon is less than 0.1:

$$dR_{\text{probe},\mu} = \sqrt{(\eta_{\text{probe}} - \eta_{\mu})^2 + (\phi_{\text{probe}} - \phi_{\mu})^2} < 0.1 \tag{C.1}$$

C.1.3 Choice of muon category

The requirements of all three categories follow in general the selection of Table C.1 (“minimum selection”), with some slight differentiations, that have to do mainly with the reconstruction procedure. In the first category we include both Combined and Tagged Muons and in the second one we remove the Tagged ones and estimate the drop in the efficiency. Finally, we re-introduce the Muon Spectrometer hits, in order to test what cost in statistics this cut causes (“extended selection”).

Therefore, we have:

- Category 1: Combined + Tagged Muons, with minimum selection
- Category 2: Combined Muons only, with minimum selection
- Category 3: Combined Muons only, with extended selection (MS hits)

In Figures C.1 and C.2 the P_T and η, ϕ efficiencies respectively, for the $Z \rightarrow \mu\mu$ sample, can be seen.

In Table C.3, we present the efficiencies, for the same sample, for all three muon caterories. As it can be seen, the efficiency in the case where the muons are Combined only is very much compatible to the case where tagged muons are included, without a significant loss in the statistics, while the third category, with the Muon Spectrometer hits included, suffers, as expected, from both a low efficiency and statistics.

C.1.4 Incorporation of the $b\bar{b} \rightarrow \mu\mu$ background

The QCD $b\bar{b} \rightarrow \mu\mu$ procedure is a background to the $Z \rightarrow \mu\mu$ one, therefore it should be taken into account in the estimation of the muon reconstruction efficiency.

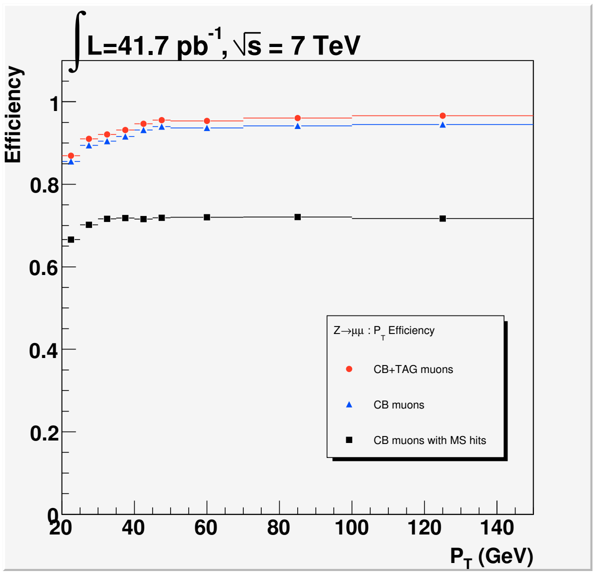

Figure C.1: P_T efficiency for $Z \longrightarrow \mu\mu$, for the three different muon categories

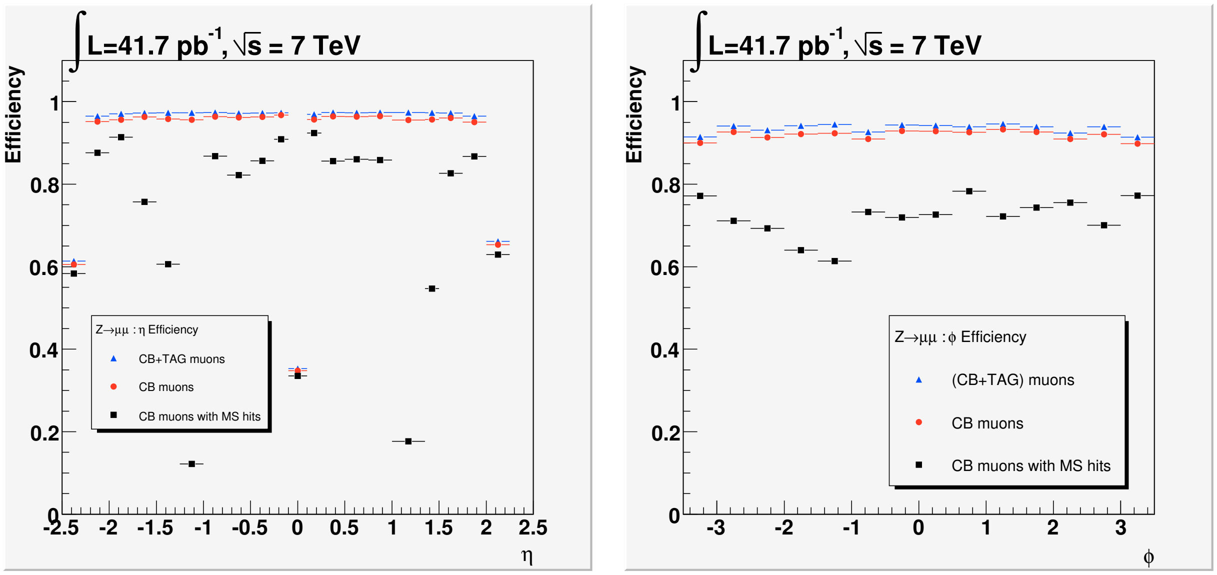

Figure C.2: η (left) and ϕ (right) efficiencies for $Z \longrightarrow \mu\mu$, for the three different muon categories

Muon Category	Matched Probes	All probes	Efficiency (%)
CB+TAG (min.selection)	3.31655 e+006	3.53865 e+006	93.72 ± 0.07
CB only (min. selection)	3.2606 e+006	3.53865 e+006	92.14 ± 0.07
CB only (ext. selection)	2.52707 e+006	3.53865 e+006	71.41 ± 0.06

Table C.3: Total Efficiency for the three different muon categories for $Z \rightarrow \mu\mu$

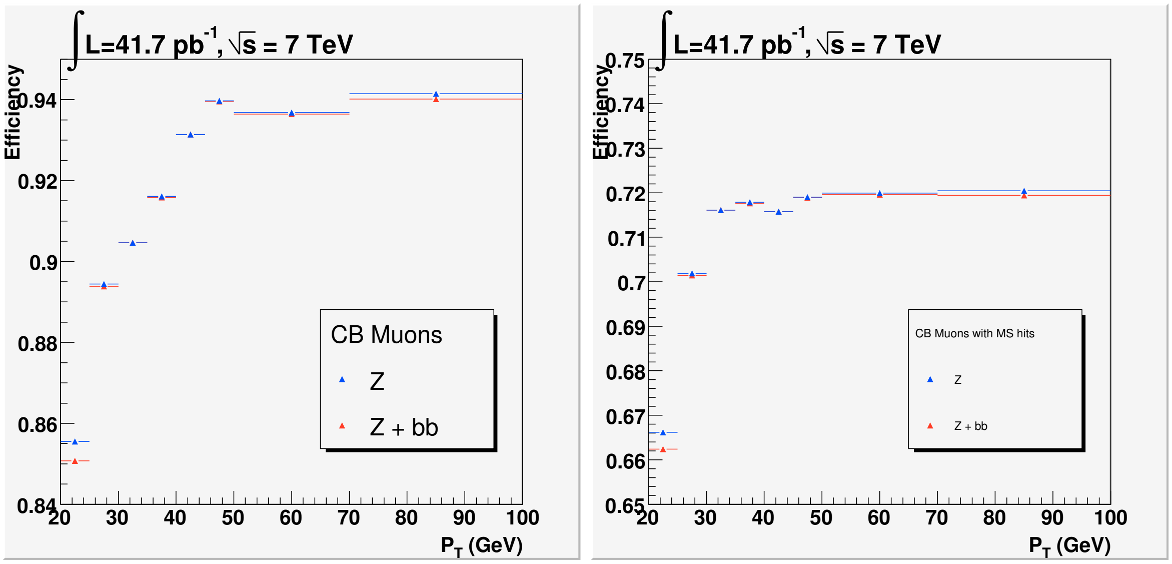

(a) (b)

Figure C.3: P_T efficiency for Z alone (blue) and Z+$b\bar{b}$ (red) decays to muons a) CB muons with minimum selection b) CB muons with MS hits

Since the muon tracks coming from the $b\bar{b}$ decay are less energetic than the Z ones (thus, it is quite rare to reproduce the Z mass and even more difficult to have two adequately energetic ones in the same event), we expect that the incorporation of this particular background will only cause a small drop in the efficiency. This is demonstrated in the combined plot of the two samples, for CB muons with minimum selection in Figure C.3(a) and for CB muons with MS hits requirement in Figure C.3(b).

Indeed, out of the almost 4 million events of the $b\bar{b} \rightarrow \mu\mu$ sample, in only 18 events we can find a probe track (i.e. a track that reproduces an invariant mass in the vicinity of 91.2 GeV). Out of these 18 events, not even one possesses a pair of tag-and-probe, namely a (second) good muon that can be associated to the probe track.

These 18 events can be normalized to the data luminosity, multiplied by the $b\bar{b}$ cross-section (73.9 pb) times the luminosity of $41.7\,\mathrm{pb}^{-1}$ and divided by the total number of the generated evens of the sample. This multiplication results to 12.36 $b\bar{b}$ events .

C.1.5 Efficiency of the data

The Tag-And-Probe method is now applied to the data.

The data should pass all the quality cuts mentioned in the previous sections (GoodRunList and Data Trigger), plus the most specific ones of this section with respect to the muons. The procedure is then similar to the estimation of the $Z \rightarrow \mu\mu$ efficiency.

Table C.4 presents the statistics and the overall efficiency of the data (again, for the three different categories) while the comparison of the Data efficiencies for the three categories of muons can be seen in Figures C.4 (P_T) and C.5 (η and ϕ).

C.2 Results for the extended muon selection

The incorporation of the Muon Spectrometer requirements provokes a drop in the efficiency of both Data and Monte Carlo of the order of 20%, if compared to the other two categories of muons.

In Figures C.6 and C.7 the P_T and η, ϕ efficiencies are presented, for both data and Monte Carlo backgrounds, for the muons passing the extended Selection Criteria (i.e., Combined only muons with the Muon Spectrometer hits requirement included).

Muon Category	Matched Probes	All probes	Efficiency (%)
CB+TAG (min.selection)	19739	21112	93.50 ± 0.06
CB only (min.selection)	19315	21112	91.49 ± 0.07
CB only (ext.selection)	14715	21112	69.70 ± 0.11

Table C.4: Total Efficiency for the several muon categories for the Data

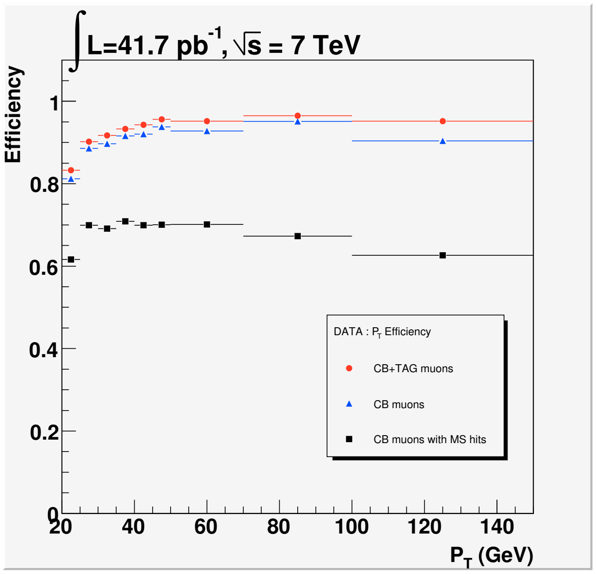

Figure C.4: P_T efficiency for Data,for the three different muon categories

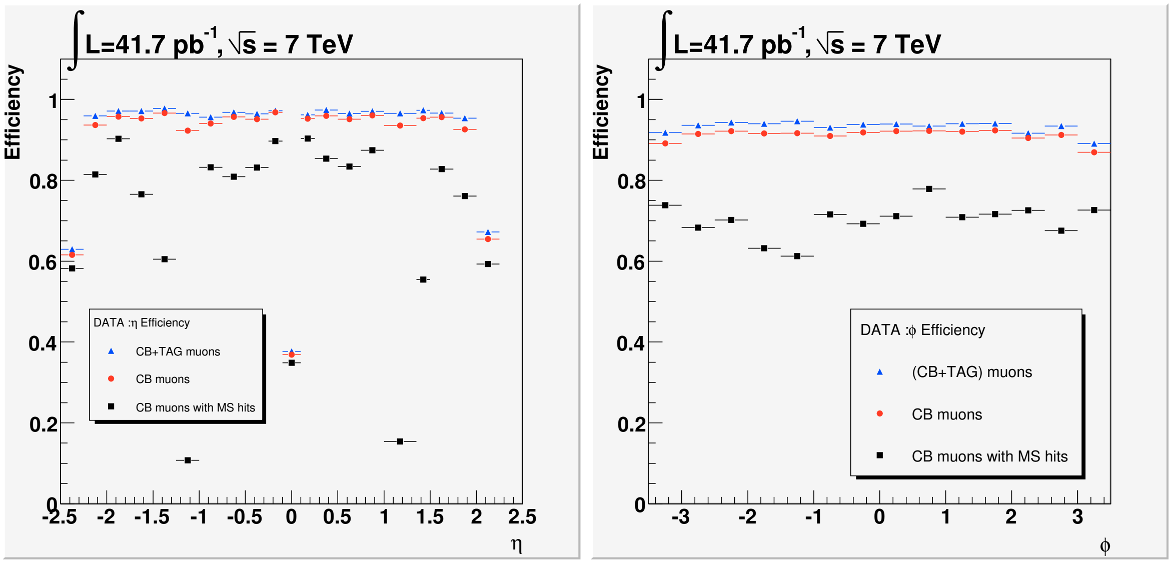

(a) (b)

Figure C.5: η (left) and ϕ (right) efficiency of Data, for the three different muon categories

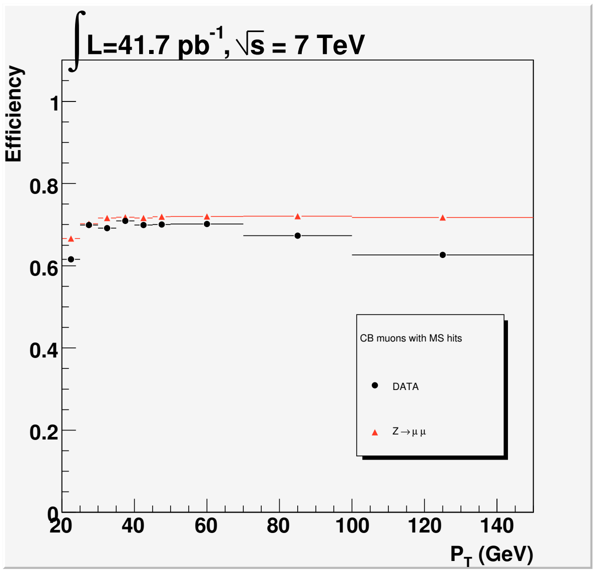

Figure C.6: Comparison of P_T efficiency for Data (black) and Monte Carlo

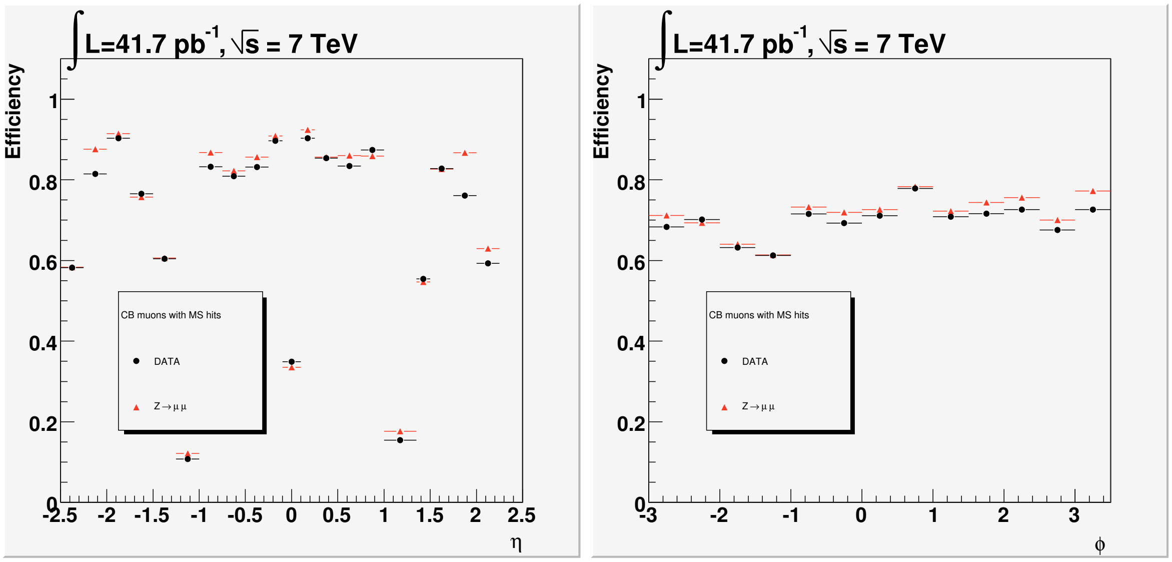

(a) (b)

Figure C.7: Comparison of η (left) and ϕ (right) efficiency for Data and Monte Carlo

From the above study, we concluded that the third category of muons (combined muons with Muon Spectrometer hits requirements) is the less efficient of the three. However, for reasons of quality of the track reconstruction (which is extremely important in the search of the new boson), we are obliged to used this particular muon selection in our analysis.

List of Figures

List of Tables